iScience

CellPress

Article

Histone Deacetylase 3 Governs Perinatal Cerebral Development via Neural Stem and Progenitor Cells

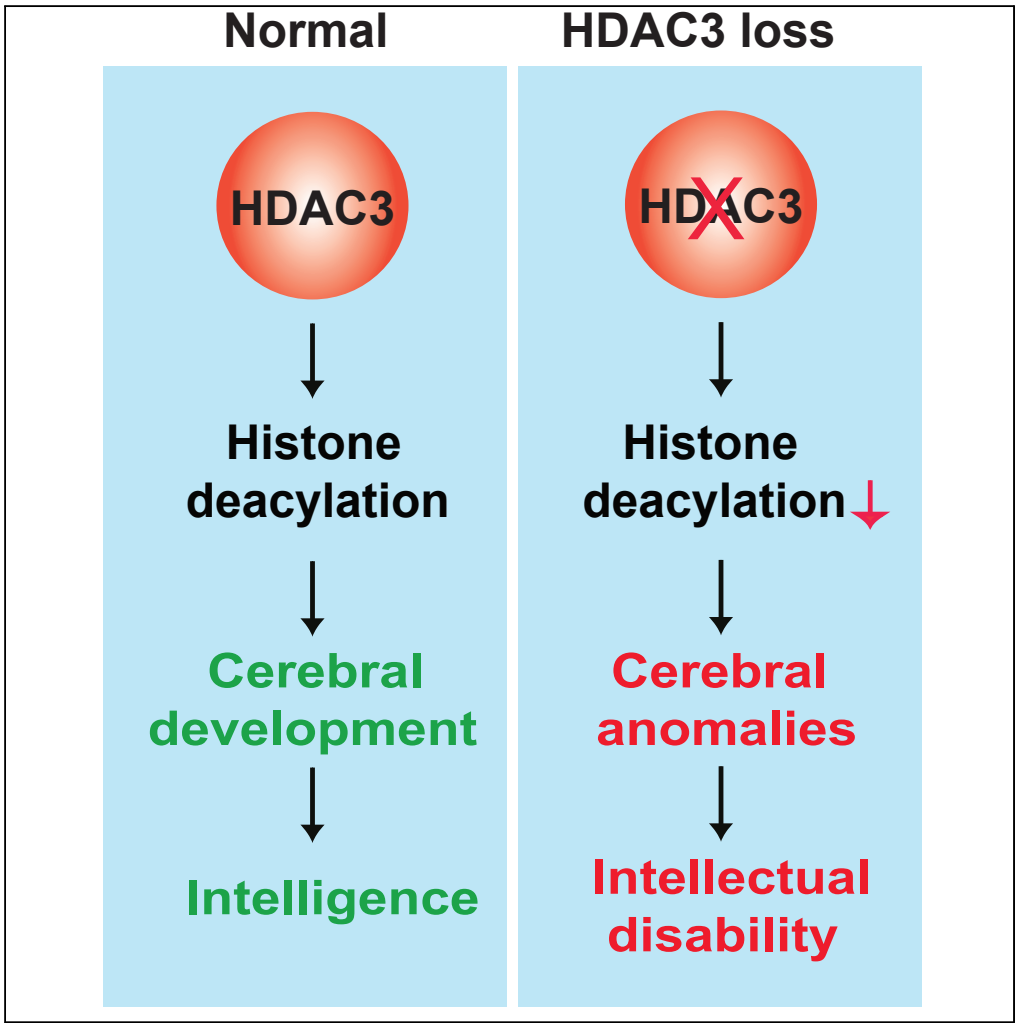

Lin Li, Jianliang Jin, Xiang-Jiao Yang

xiang-jiao.yang@mcgill.ca

HIGHLIGHTS

HDAC3 inactivation causes developmental defects in the neocortex and hippocampus

HDAC3 loss leads to depletion of embryonic neural stem and progenitor cells

HDAC3 inhibition abolishes neurosphere formation *in vitro*

HDAC3 interacts with NFIB and other transcription factors in cerebral development

Li et al., iScience *20*, 148–167
October 25, 2019
https://doi.org/10.1016/j.isci.2019.09.015

iScience

CellPress

Article

Histone Deacetylase 3 Governs Perinatal Cerebral Development via Neural Stem and Progenitor Cells

Lin Li,[1,2] Jianliang Jin,[1,3] and Xiang-Jiao Yang[1,2,4,5,6,*]

SUMMARY

We report that cerebrum-specific inactivation of the histone deacetylase 3 (HDAC3) gene causes striking developmental defects in the neocortex, hippocampus, and corpus callosum; post-weaning lethality; and abnormal behaviors, including hyperactivity and anxiety. The defects are due to rapid loss of embryonic neural stem and progenitor cells (NSPCs). Premature neurogenesis and abnormal neuronal migration in the mutant brain alter NSPC homeostasis. Mutant cerebral cortices also display augmented DNA damage responses, apoptosis, and histone hyperacetylation. Moreover, mutant NSPCs are impaired in forming neurospheres *in vitro*, and treatment with the HDAC3-specific inhibitor RGFP966 abolishes neurosphere formation. Transcriptomic analyses of neonatal cerebral cortices and cultured neurospheres support that HDAC3 regulates transcriptional programs through interaction with different transcription factors, including NFIB. These findings establish HDAC3 as a major deacetylase critical for perinatal development of the mouse cerebrum and NSPCs, thereby suggesting a direct link of this enzymatic epigenetic regulator to human cerebral and intellectual development.

INTRODUCTION

Histone acetylation is critical for establishing, maintaining, and regulating all eukaryotic epigenomes (Suganuma and Workman, 2008; Yang and Seto, 2008a). This modification is reversible and controlled by the opposing actions of acetyltransferases and deacetylases. There are 18 mammalian histone deacetylases (HDACs) (Haberland et al., 2009; Yang and Seto, 2008b). Different from the other 15 deacetylases, HDAC1, HDAC2, and HDAC3 are catalytic subunits of different stoichiometric multiprotein complexes, which are highly stable, even enough for purification via conventional chromatography (Yang and Seto, 2008b). These complexes serve as functional cores for additional interaction with other partners to exert gene-specific histone deacetylation and subsequent functional impact (Yang and Seto, 2008b). Although HDAC1 and HDAC2 are part of at least three different complexes containing >15 other proteins (Yang and Seto, 2008b), HDAC3 is the catalytic subunit of several paralogous tetrameric complexes, composed of the nuclear receptor corepressor NCoR (or its paralog SMRT), the WD40 protein TBL1 (a.k.a. TBL1X; or its paralogs TBL1XR1 and TBL1Y), and the signaling regulator GPS2 (no homology to GPS1 and no paralogs) (Karagianni and Wong, 2007; Oberoi et al., 2011). Thus, HDAC3 is unique among the HDAC superfamily. Within the complexes, NCoR and SMRT serve as scaffolds for complex assembly with their deacetylase-activating domains for HDAC3 interaction and other domains for association with TBL1 and GPS2 (Codina et al., 2005; Oberoi et al., 2011; Watson et al., 2012). Complex formation is crucial for the maximal activity of HDAC3 (Guenther et al., 2001; Guenther et al., 2000).

The mouse gene has been subject to various genetic studies. Germline deletion of *Hdac3* leads to embryonic lethality at E9.5 (Knutson et al., 2008; Montgomery et al., 2008), indicating an essential role in embryo development. Conditional deletion of *Hdac3* in the liver, heart, muscle, fat, or intestine causes abnormal development or metabolism (Alenghat et al., 2013; Emmett et al., 2017; Farooq et al., 2008; Feng et al., 2011; Knutson et al., 2008; Lu et al., 2018; Montgomery et al., 2008; Summers et al., 2013; Sun et al., 2012), indicating that *Hdac3* is crucial for development and homeostasis of these tissues. Its role in the mouse brain also started to emerge (McQuown et al., 2011; Norwood et al., 2014; Nott et al., 2016; Zhang et al., 2016). These studies raise an interesting question about the roles in human development. Related to this, a child with a heterozygous *HDAC3* mutation is associated with neonatal epileptic encephalopathy (Helbig et al., 2016). Another child with an *HDAC3* mutation displays learning difficulties and brain abnormalities (Zhou et al., 2019a). Three individuals with mutations in the genes for NCoR and SMRT show learning difficulties, intellectual disability, or developmental delay (Zhou et al., 2019a). Multiple patients

[1]The Rosalind & Morris Goodman Cancer Research Center, Montreal, QC H3A 1A3, Canada

[2]Department of Medicine and McGill University, Montreal, QC H3A 1A3, Canada

[3]Research Center for Bone and Stem Cells, Department of Human Anatomy, Key Laboratory of Aging & Disease, Nanjing Medical University, Nanjing, Jiangsu 211166, China

[4]Department of Biochemistry, McGill University, Montreal, QC H3A 1A3, Canada

[5]Department of Medicine, McGill University Health Center, Montreal, QC H3A 1A3, Canada

[6]Lead Contact

*Correspondence: xiang-jiao.yang@mcgill.ca

https://doi.org/10.1016/j.isci.2019.09.015

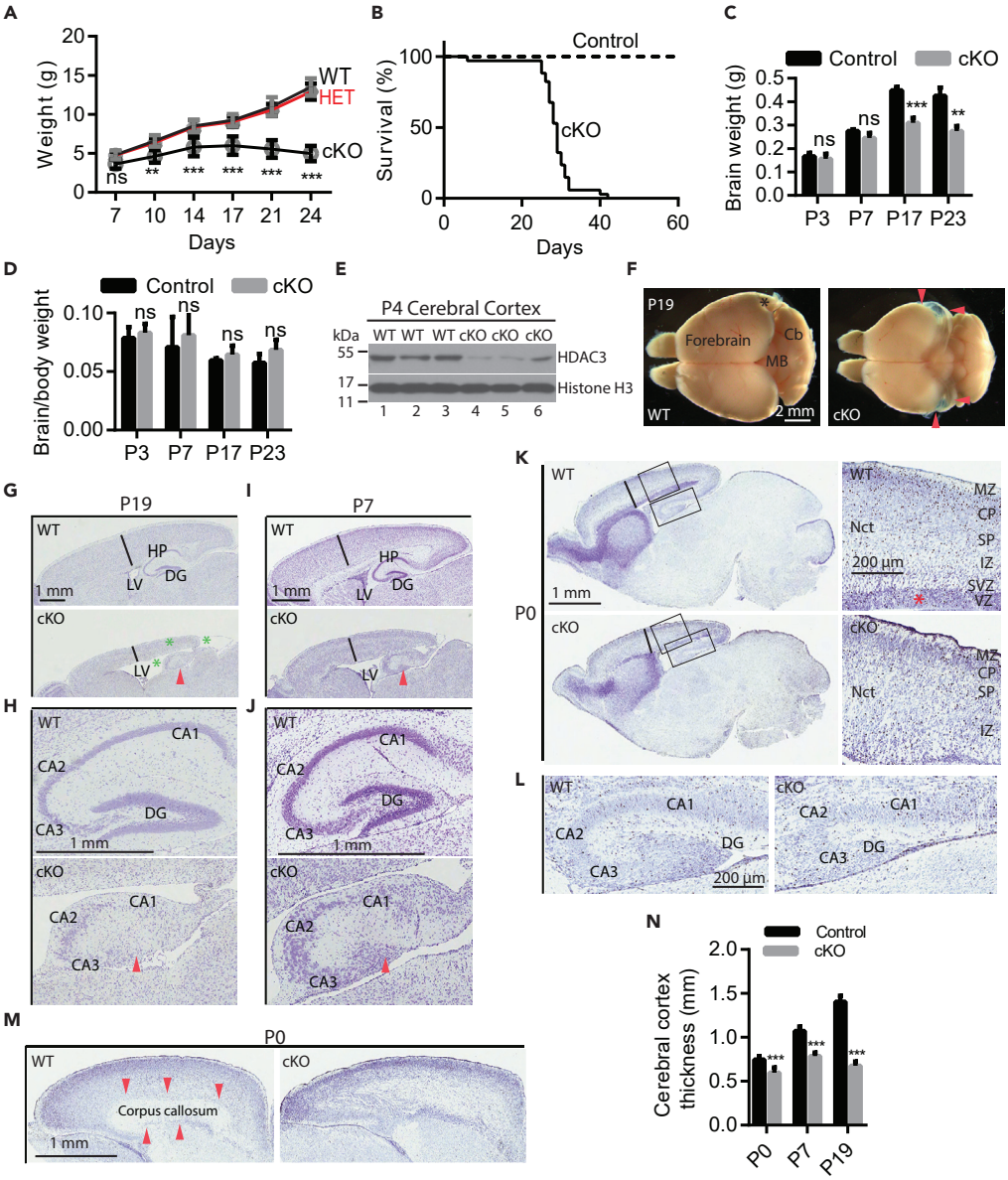

Figure 1. Cerebrum-Specific *Hdac3* Loss Causes Defects in the Neocortex, Hippocampus, and Corpus Callosum

(A) Growth curves for wild-type (WT), heterozygous (HET), and homozygous cerebrum-specific knockout (cKO) mice (n = 12, 8, and 7 for the WT, HET, and cKO groups, respectively). cKO was compared with WT for statistical analysis.

(B) Survival curves for control and homozygous mutant mice (n = 40 and 38 for the control and cKO groups, respectively).

(C and D) Brain weight and brain/body weight ratio at P3, P7, P17, and P23 (n ≥ 3 for all groups).

(E) Western blotting showed efficient deletion of *Hdac3* in the cerebral cortex of mutant pups at P4 (n = 3). No other bands were detected.

(F) Representative brain photos of wild-type and cKO mice at P19. Red arrowheads mark cysts in the cKO brain. In the wild-type, an asterisk denotes damage caused during dissection.

(G) Representative images for Nissl staining of WT and cKO brain sections from pups at P19. A red arrowhead denotes the underdeveloped mutant hippocampus, and green asterisks mark the region corresponding to the cysts shown in (F).

(H) Enlarged images of hippocampal regions of the brain sections shown in (G).

(I and J) Same as (G and H) but at P7.

(K) Nissl staining of brain sections indicated that the ventricular/subventricular zone almost disappears in the P0 mutant cerebrum. The boxed areas in the left panels are enlarged at the right or in (L). A red asterisk denotes the ventricular/subventricular zone in the wild-type.

(L) Enlarged images of hippocampal regions of boxed in (K).

Figure 1. *Continued*

(M) Representative images showing agenesis of the mutant corpus callosum at P0. Red arrowheads denote the boundary of the corpus callosum in the WT cerebral cortex. For panels (F–M), representative images from serial sections are shown; at least three embryos or pups were analyzed for each group.

(N) Quantification of the cerebral neocortical thickness at the middle parts as marked with solid lines in (G), (I), and (K). n = 3 for all groups.

Abbreviations: CA1, Cornu Ammonis 1; CA2, Cornu Ammonis 2; CA3, Cornu Ammonis 3; Cb, cerebellum; CP, cortical plate; DG, dentate gyrus; HP, hippocampus; IZ, intermediate zone; LV, lateral ventricle; MB, middle brain; MZ, marginal zone; Nct, neocortex; SP, subplate; SVZ, subventricular zone; VZ, ventricular zone. ns, not statistically significant; **, $p < 0.01$; ***, $p < 0.001$. Scale bars, 2 mm in (F); 1 mm in (G–J), (M), and the left panels of (K); and 200 μm in (L) and right panels of (K). See also Table S1 and Figures S1 and S2.

with *TBL1XR1* mutations have intellectual disability (Heinen et al., 2016; Laskowski et al., 2016; Saitsu et al., 2014). These clinical features suggest that HDAC3 complexes may be critical for early cerebral development. We thus carried out cerebrum-specific deletion of mouse *Hdac3*. The mutant embryos and pups show cerebral defects, impaired NSPC development, altered histone modifications, and deregulated transcription.

RESULTS

Hdac3 Is Highly Expressed in the Developing Cerebrum

To examine the role of HDAC3 in cerebral development, we initially determined the expression pattern of *Hdac3* in the developing cerebral cortex. Indirect immunofluorescence microscopy using a specific anti-HDAC3 antibody indicated that *Hdac3* is abundantly expressed in the developing ventricular zone (VZ), subventricular zone (SVZ), cortical plate (or preplate), and hippocampus at P0 (Figure S1A), E16.5 (Figure S1D), and E12.5 (Figure S1G). In addition, RNA sequencing (RNA-seq) showed that the FPKM value for *Hdac3* mRNA is higher than 30 in the neonatal cerebral cortex and the neurospheres cultured from E16.5 embryonic cerebral cortex (Figure S1J), indicating high-level expression of this deacetylase in the developing cerebral cortex and embryonic NSPCs. The expression data suggest that HDAC3 may have an important role in regulating perinatal cerebral development.

Cerebrum-Specific *Hdac3* Deletion Leads to Early Lethality and Abnormal Behaviors

To evaluate directly the function of HDAC3 in early cerebral development, we generated cerebrum-specific knockout mice by using the *Emx1-Cre* line, which expresses the Cre recombinase specifically in the cerebrum and its precursors as early as E10.5 (Chou et al., 2009; Gorski et al., 2002). Mating of this line with $Hdac3^{f/f}$ mice produced the $Hdac3^{f/f}$; *Emx1-Cre* knockout (or cKO) mice. Knockout pups were born at a normal Mendelian ratio (Table S1) and appeared grossly normal, with some displaying up-turned paws for a few days in the first week of life. Starting from week 2, all mutant pups failed to thrive and became significantly smaller than the wild-type (Figure 1A). In week 3, some mutant pups were runted and subsequently died, with a majority unable to survive in the week after (Figures 1A and 1B). The exact cause of lethality is unclear, but we have found similar lethality in another line with cerebral defects (You et al., 2015b).

Around P21, the mutant pups started to show obvious abnormalities in walking and were overactive. Moreover, 2- or 3-week-old mutant pups were also easily irritated when touched. We thus carried out open field tests to assess the anxious and hyperactive status of mutant mice (Li et al., 2019). Paired control and cKO mice at P22 were tested in an arena for 10 min and recorded by a video tracking system. The results showed that, compared with the wild-type counterparts, the mutant pups spent significantly more time at the border (Figures S2A and S2C) and traveled much more (Figures S2B and S2C). Thus, the homozygous mutant pups displayed hyperactivity and anxiety.

The brain weight of the mutant pups was comparable with that of the wild-type counterparts at P7 but showed significant reduction at P17 and P23 (Figure 1C). However, the brain/body weight ratio was comparable between the wild-type and mutant pups, even at P17 and P23 (Figure 1D). Thus, the mutant brain remained proportional to the body weight (Figures 1C and 1D), indicative of no microcephaly in mutant pups.

We assessed whether *Hdac3* was efficiently and specifically deleted in the mutant cerebrum. For this, we carried out western blotting analysis of cerebral extracts from wild-type and mutant pups. As shown in Figure 1E, HDAC3 was specifically detected in the wild-type cerebral cortices at P4 (lanes 1–3). Importantly, the

protein level was greatly reduced in the mutants (lanes 4–6). Quantification confirmed this assessment (Figure S1L). To investigate whether the deletion is also efficient at early developmental time points, we performed immunofluorescence microscopy to analyze expression of HDAC3 on brain or embryonic sections at P0, E16.5, and E12.5. As shown in Figures S1A–S1C, *Hdac3* was efficiently deleted at a majority of cells in the neocortex or hippocampus but not the striatum at P0. A small number of cells remained positive in the cKO mutant neocortex (Figures S1A and S1B). Some of them may be interneurons that migrate in a parallel manner from the ganglionic eminence (Marin and Rubenstein, 2001). Another possibility is microglia, which are of hematopoietic origin. The Cre recombinase in the *Emx1-Cre* line is not expressed in interneurons or microglia (Chou et al., 2009; Gorski et al., 2002). The deletion was also efficient at E16.5 (Figures S1D and S1F). As for E12.5, HDAC3 was lost in the mutant cortical plate but not the ganglionic eminence (GE) (Figures S1G and S1I). Thus, the *Emx1-Cre* line induces efficient and specific *Hdac3* deletion in the cerebrum and its embryonic precursors, at least starting at E12.5.

HDAC3 Is Crucial for Development of the Neocortex, Hippocampus, and Corpus Callosum

During brain dissection, we unexpectedly noticed prominent cysts at the caudal part of the mutant brain from 3-week-old pups (Figure 1F). Nissl staining of serial brain sections revealed thin neocortices and large lateral ventricles in the mutant forebrain (Figure 1G). Moreover, the mutant hippocampus was poorly developed, with the dentate gyrus barely visible (Figure 1H). Such neocortical and hippocampal defects were also present in the mutant pups at earlier time points, such as P7 (Figures 1I and 1J) and P0 (Figures 1K–1L). Moreover, Nissl staining of serial brain sections from P0 showed that the mutant corpus callosum was underdeveloped, with no clear boundaries between the corpus callosum and its adjacent tissues (Figure 1M). Quantification confirmed that the mutant cerebral cortex was significantly thinner starting at P0 (Figure 1N). Thus, *Hdac3* deletion leads to cerebral defects starting at least around birth.

To substantiate these histological observations, we carried out immunostaining to examine the defects at the molecular and cellular levels. For this, we used various antibodies against makers (such as Cux1, Ctip2, and Tbr1) specific to different neocortical layers. Cux1 is specifically expressed in upper layer neurons, whereas Ctip2 (a.k.a. Bcl11b) and Tbr1 are cortical markers of deeper layer neurons (Molyneaux et al., 2007). As shown in Figure 2, neocortical lamination was altered in the mutant neonatal cerebrum. There was no clear boundary for the mutant Ctip2$^+$ layer (Figures 2A and 2B, upper panels). Quantification confirmed abnormal distribution of such cells in the mutant neocortex (Figure 2C). This was also true for Tbr1$^+$ neurons in the mutant neocortex (Figures 2D and 2E, upper panels and 2F). The Cux1$^+$ and Cux2$^+$ layers were obvious in the wild-type neocortices but missing in the mutant neocortices (Figures 2A, 2B, 2D, and 2E, lower panels). Such alterations were also evident at P7 (Figure S3) and E16.5 (Figure S4). Thus, cerebrum-specific *Hdac3* deletion results in developmental defects in the neocortex at least starting at E16.5.

The above-mentioned immunostaining experiments also confirmed hippocampal abnormalities in the embryonic, neonatal, and postnatal mutant brains (Figures 2, S3, and S4). To substantiate this, we utilized two other markers, NeuroD and GFAP. The former is a neuron-specific transcription factor, and the latter is a marker of radial glia cells (precursors of neural stem and progenitor cells [NSPCs]) and activated astrocytes. Immunostaining with antibodies against both markers supported the abnormal morphology of the mutant hippocampus at P0, with fewer NeuroD$^+$ cells but more GFAP$^+$ cells than the wild-type (Figures S5A, S5C, S5D, and S5F). As shown in Figures S5B, S5C, S5E, and S5F, the abnormality was even more dramatic in the mutant hippocampus at P7. Thus, these results indicate that cerebrum-specific *Hdac3* deletion leads to profound developmental defects in the hippocampus.

HDAC3 Is Required for Development of Neural Stem and Progenitor Cells

From DAPI and Nissl staining, we noticed that the ventricular/subventricular zone is thin in the mutant brain at E16.5 (Figure S1K) and almost missing at P0 (Figure 1K). The embryonic ventricular/subventricular zone is the area where radial glia cells reside (Noctor et al., 2001). To investigate how neural stem cells (NSCs) are affected, we carried out immunofluorescence staining of embryonic and brain sections using an antibody against Sox2, an NSC-specific marker (Ellis et al., 2004). At P0, the Sox2$^+$ layer was dramatically reduced in the mutant (Figures 3A and 3B), indicating that *Hdac3* loss exhausts the NSC compartment. Moreover, ectopic Sox2$^+$ cells were found outside of the mutant ventricular/subventricular zone (Figures 3A and 3C). At E16.5, the Sox2$^+$ layer was also dramatically reduced in the mutant (Figures 3D and 3E), and more ectopic Sox2$^+$ cells were observed outside of the mutant ventricular/subventricular zone

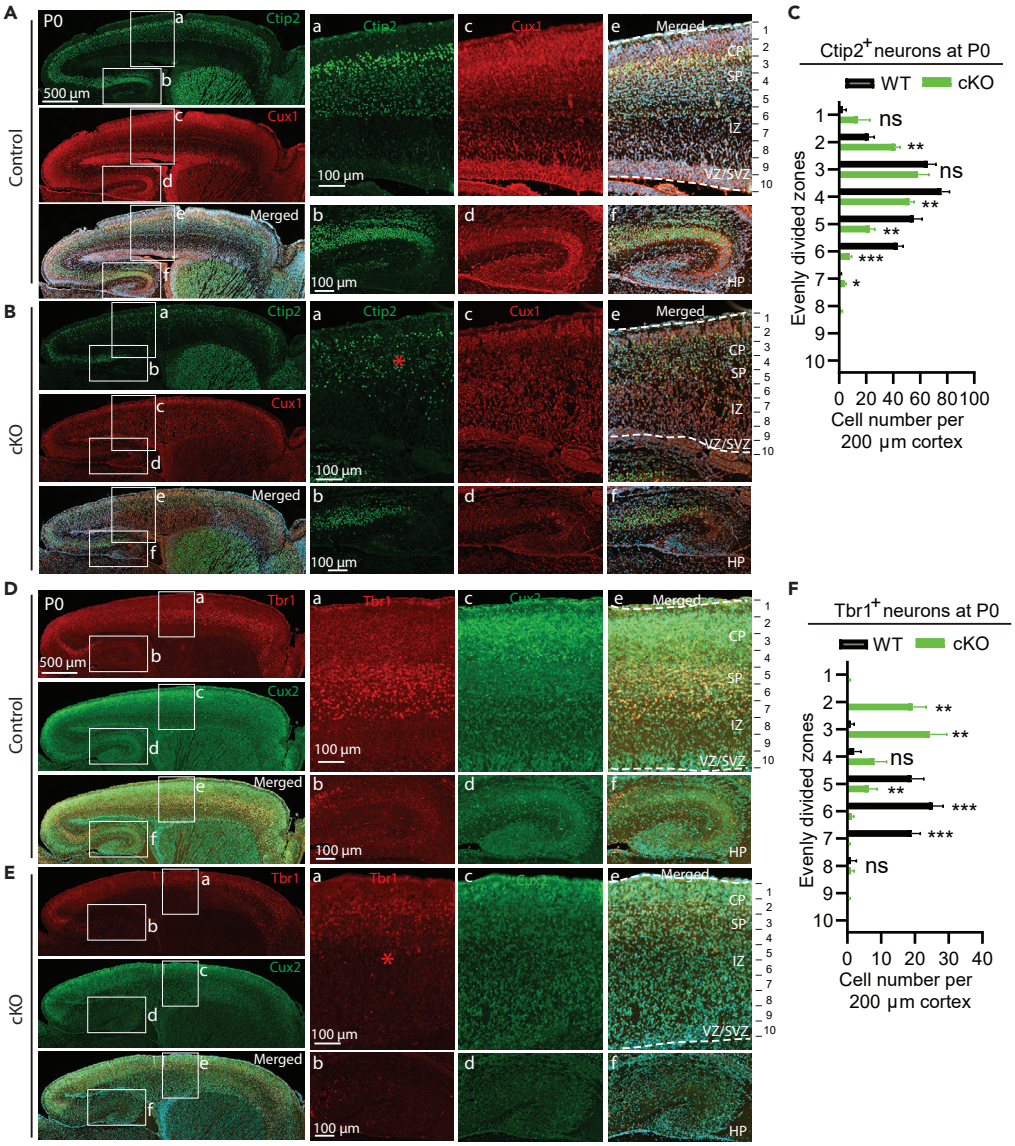

Figure 2. Abnormal Neocortical Lamination and Hippocampal Development in the Mutant Brain

(A and B) Co-immunostaining of wild-type and mutant neonatal brain sections with anti-Cux1 and -Ctip2 antibodies. The former labels the SVZ and layers II-IV of adult neocortex (Nieto et al., 2004), whereas the latter marks layers V–VI (Lai et al., 2008). A red asterisk denotes a disorganized Ctip2$^+$ layer in the mutant.

(C) The mutant neocortical layers are not clearly separated, so the wild-type or mutant neocortex were divided equally into 10 zones for determination of the Ctip2$^+$ cell distribution (n = 3 for each group).

(D and E) Co-immunostaining of wild-type and mutant P0 brain sections with anti-Tbr1 and -Cux2 antibodies. The former labels layer VI of the adult neocortex (Hevner et al., 2001), whereas the latter marks layers II–IV (Nieto et al., 2004). A red asterisk denotes ectopic distribution of Tbr1$^+$ cells.

(F) The wild-type or mutant neocortex was divided equally into 10 zones for determination of the Tbr1$^+$ cell distribution (n = 3 for each group).

Abbreviations are listed in the legend to Figure 1. Scale bars, 500 μm for the left panels and 100 μm for the rest of the panels of (A and B) and (D and E). ns, not statistically significant; *, $p < 0.05$; **, $p < 0.01$; ***, $p < 0.001$. See also Figures S3–S5.

(Figures 3D and 3F). Thus, at both P0 and E16.5, HDAC3 is critical for proper development of the Sox2$^+$ cell layer. By contrast, thickness of the Sox2$^+$ cell layer was not significantly affected in the mutant at E12.5 (Figures 3G and 3H), although HDAC3 was efficiently deleted (Figures S1G–S1I), indicating that HDAC3 is dispensable for formation of the Sox2$^+$ cell layer at this embryonic stage.

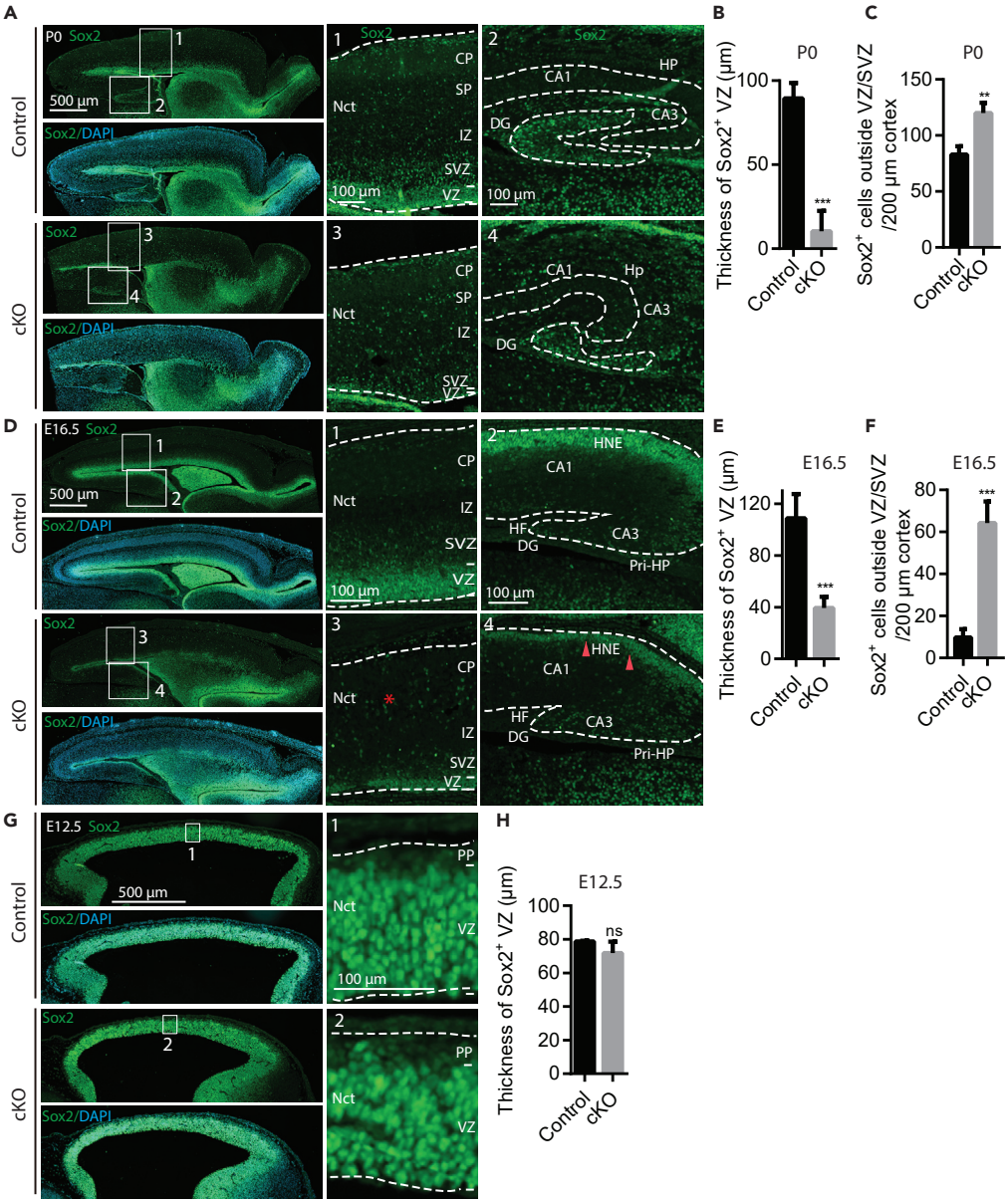

Figure 3. Cerebrum-Specific *Hdac3* Deletion Compresses the NSC Compartment

(A) Immunostaining analysis with anti-Sox2 antibody showed almost complete disappearance of $Sox2^+$ cells in the mutant VZ at P0.

(B) $Sox2^+$ cells are dense in the VZ, so its thickness instead of the cell number was measured for the $Sox2^+$ cell layer (n = 4).

(C) $Sox2^+$ cells outside the VZ/SVZ were counted (n = 4).

(D) Immunostaining analysis revealed reduction of $Sox2^+$ cells in the VZ of mutant cerebral cortex at E16.5. An asterisk in the middle bottom panel marks $Sox2^+$ cells outside the VZ/SVZ. Two red arrowheads in the right bottom panel denote a thinner layer of the hippocampal neuroepithelium in the mutant.

(E and F) Similarly as in (B and C), the thickness of the $Sox2^+$ cell layer in the VZ and the number of $Sox2^+$ cells outside the VZ/SVZ were measured (n = 4).

(G) Immunostaining to compare wild-type and mutant $Sox2^+$ cells at E12.5.

(H) Thickness of the $Sox2^+$ layer at the VZ is comparable between the control and cKO cerebral cortices at E12.5 (n = 3).

Abbreviations: HF, hippocampal fissure; HNE, hippocampal neuroepithelium; Pri-HP, primordial hippocampus. Other abbreviations are listed in the legend to Figure 1. Scale bars, 500 μm for the left panels and 100 μm for the rest of the panels of (A), (D), and (G). ns, not statistically significant; **, $p < 0.01$; ***, $p < 0.001$.

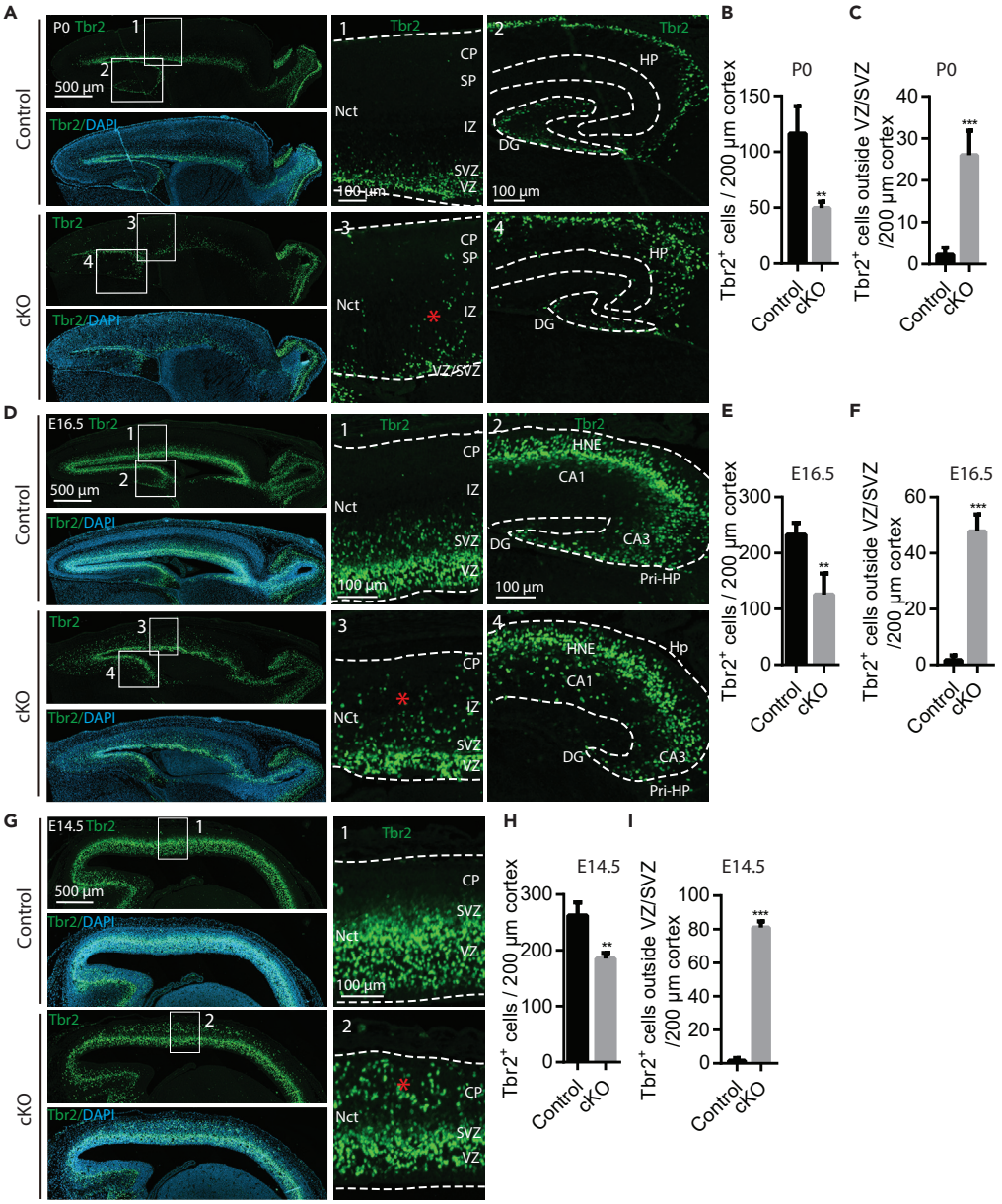

Figure 4. Cerebral *Hdac3* Deletion Depletes Tbr2$^+$ Neuronal Progenitors

(A–C) (A) Immunostaining analysis with anti-Tbr2 antibody to detect Tbr2$^+$ progenitors in brain sections from wild-type and mutant neonates. (B and C) Quantification of Tbr2$^+$ progenitors from sections as shown in (A) (n = 4).

(D) Same as in (A) except E16.5 embryo sections were analyzed (n = 4). Dashed lines denote borders of the hippocampus and neocortex.

(E and F) Quantification of Tbr2$^+$ progenitors from sections as shown in (C). n = 3.

(G) Same as (A) except that E14.5 embryonic sections were analyzed.

(H and I) Quantification of Tbr2$^+$ progenitors from sections as shown in (G). n = 3. The number of Tbr2$^+$ progenitor cells in the mutant is significantly reduced at E14.5 and E16.5 but comparable with the wild-type at E12.5 (Figures S6B and S6C). Red asterisks in (A), (D), and (G) mark ectopic distribution of Tbr2$^+$ progenitors. Scale bars, 500 μm for the left panels and 100 μm for the rest of the panels of (A), (D), and (G). **, $p < 0.01$; ***, $p < 0.001$.

See also Figures S6A–S6C.

We next analyzed different embryonic and brain sections using an antibody specific to the transcription factor Tbr2, a marker of neuronal progenitors critical for neocortex and hippocampus development (Arnold et al., 2008; Hodge et al., 2012). As shown in Figures 4A and 4B, the Tbr2$^+$ progenitor number was reduced

in the mutant ventricular/subventricular zone at P0. Reminiscent of what was observed with $Sox2^+$ cells (Figure 3), more $Tbr2^+$ cells were found outside the mutant ventricular/subventricular zone (Figures 4A and 4C). Similar to the mutant ventricular/subventricular zone, the $Tbr2^+$ progenitor cell number was greatly reduced in the mutant hippocampus (Figure 4A). Consistent with this, few $Tbr2^+$ progenitor cells were detected in the mutant hippocampus at P7 (Figure S6A). Moreover, at both E16.5 (Figures 4D and 4E) and E14.5 (Figures 4G and 4H), the $Tbr2^+$ progenitor cell number was significantly decreased in the mutant neocortices. As with the neonatal mutant brain, more ectopic $Tbr2^+$ cells were also observed outside the ventricular/subventricular zone at both E16.5 (Figure 4F) and E14.5 (Figure 4I), indicating impaired migration of the progenitors in the mutant brain. In contrast to what was observed at P0, E16.5, and E14.5, the $Tbr2^+$ progenitor cell number remained comparable between the wild-type and mutant neocortical primordium at E12.5 (Figures S6B and S6C), indicating that HDAC3 is not essential for the formation of the $Tbr2^+$ progenitor cell layer at this embryonic stage. Thus, *Hdac3* deletion reduces the number of NSPCs required for neocortical development starting at E14.5.

The hippocampal fissure is formed at E17.5, and its boundary within the CA1-CA3 regions also starts to emerge at this time point (Urban and Guillemot, 2014). As described earlier (Figure 3A, right panels), the upper blade of the dentate gyrus was almost missing and there were fewer $Sox2^+$ cells in the dentate gyrus at P0. At E16.5, noticeably fewer $Sox2^+$ cells were present in the hippocampal neuroepithelium area (Figure 3D, right panels). The hippocampus (or its primordium) in the mutant cerebral cortices at P0 and E16.5 were smaller when compared with the wild-type (Figures 3A and 3D). At P0, there were fewer $Tbr2^+$ cells in the mutant hippocampus than the wild-type (Figure 4A). One week later, this population of $Tbr2^+$ cells disappeared in the mutant hippocampus (Figure S6A). Thus, cerebrum-specific *Hdac3* loss reduces the number of NSPCs required for hippocampus development.

Hdac3 Deletion Induces Premature Neurogenesis and Disrupts Neuronal Migration

Embryonic NSPCs either proliferate to replenish the population or differentiate to generate new neurons for proper brain development (Cattaneo and McKay, 1990). To investigate whether neurogenesis from NSPCs is affected, we performed immunostaining of embryo sections using Tuj1 antibody, which recognizes a neuron-specific β-tubulin (You et al., 2015a; You et al., 2015b). As shown in Figures S7A and S7B, thickness of the $Tuj1^+$ cell layer was similar between the wild-type and mutant brains at E13.5. This became slightly different at E14.5. Although the cerebral cortex remained similar between wild-type and mutant brains, the $Tuj1^+$ cell layer was thicker in the mutant (Figures S7C and S7D), indicating that in the absence of *Hdac3*, neurogenesis is enhanced at this developmental stage. At E15.5, the $Tuj1^+$ cell layer was comparable between the wild-type and mutant brains but the cerebral cortex was thinner in the mutant (Figures S7E and S7F), so the ratio of the $Tuj1^+$ cell layer to the neocortex was still higher in the mutant. These results indicate that the neurogenic zone expands at both E14.5 and E15.5. Related to this, at both developmental stages, the ventricular/subventricular zone was compressed in the mutant (Figures S7C and S7E, labeled with green asterisks). Moreover, ectopic distribution of $Tuj1^+$ neurons was also observed in the mutant VZ/SVZ (Figures S7C and S7E), indicative of aberrant birth of $Tuj1^+$ neurons from NSPCs. These results indicate that *Hdac3* deletion leads to premature neurogenesis.

Embryonic NSPCs are subject to a delicate balance between self-renewal (proliferation) and differentiation (neurogenesis). To investigate whether NSPC proliferation is affected, we examined the S phase by carrying out BrdU labeling *in vivo* (You et al., 2015a; You et al., 2015b). For the assays, BrdU was injected into pregnant mice at E12.5 or E13.5 for embryo retrieval 1 h later. Indirect immunofluorescence microscopy was then performed with embryonic sections using anti-BrdU and -Ki67 antibodies. As shown in Figures S6D–S6G, no difference was observed between the mutant and wild-type at either developmental time point. Considering that $Sox2^+$ NSCs or $Tbr2^+$ progenitors are comparable between the wild-type and mutant neocortices at E12.5 (Figures 3G, 3H, S6B, and S6C), these results indicate that NSPC proliferation is not affected.

For neurogenesis, NSPCs exit the cell cycle for neuronal differentiation. To gain mechanistic insights into the observations about premature neurogenesis, we analyzed cell cycle exit (You et al., 2015a; You et al., 2015b). For this, BrdU was injected into pregnant mice at E12.5 and E14.5 for embryo retrieval 24 h later at E13.5 and E15.5, respectively. Indirect immunofluorescence microscopy was then performed with anti-BrdU and -Ki67 antibodies. As shown in Figures S8A–S8C, compared with the wild-type, there were significantly more $BrdU^+Ki67^-$ cells (green) in the mutant ventricular zone at E13.5 and E15.5, indicating that more NSPCs exit the cell cycle at 24 h after BrdU injection. This supports enhanced neurogenesis in the mutant.

From immunostaining, we observed ectopic distribution of $Sox2^+$ NSCs (Figure 3), $Tbr2^+$ progenitors (Figure 4), $Tuj1^+$ neurons (Figure S7), and cortical layer-specific neurons (Figures 2, S3, and S4). These observations suggest that neuronal migration might be affected. To evaluate this directly, we injected BrdU into pregnant mice at E12.5 or E14.5 for embryo retrieval 2 or 4 days later at E16.5. As shown in Figures S8D–S8E, neuronal migration was compromised in the mutant neocortex. Specifically, for BrdU tracing from E12.5 to E16.5, a majority of $BrdU^+$ cells were observed in the cortical plate in the wild-type neocortex (Figure S8D, upper panel), whereas such cells were rather evenly distributed throughout the mutant neocortex (Figure S8D, lower panel). For BrdU tracing from E14.5 to E16.5, a majority of $BrdU^+$ cells were localized to the wild-type ventricular/subventricular zone (Figure S8E, upper panel), whereas such cells were more evenly distributed throughout the mutant neocortex, with a lot of $BrdU^+$ cells in the cortical plate (Figure S8E, lower panel). These results indicate impairment of neuronal migration in the mutant cerebral cortex.

Compared with the wild-type, there were more $Ki67^+$ cells in the mutant immediate zone and cortical plate at E15.5 (Figure S8B) and E16.5 (Figures S8D–S8E). Quantification confirmed this assessment (Figure S8F). These results indicate that proliferating cells are ectopically located outside the ventricular/subventricular zones in the mutant at E15.5 and E16.5. Related to this, $Sox2^+$ NSCs and $Tbr2^+$ progenitors were ectopically located in the mutant (Figures 3 and 4). Thus, alteration of NSPC distribution is a prominent feature in the mutant.

Hdac3 Deletion Augments DNA Damage Response and Triggers Apoptosis

Global deletion of *Hdac3* in embryonic fibroblasts induces DNA damage and triggers apoptosis (Bhaskara et al., 2008), so we investigated whether cerebrum-specific loss of *Hdac3* causes similar defects. For this, immunostaining of embryonic and brain sections with an anti-γH2A.X antibody was used to detect DNA damage responses and TUNEL assays were employed to assess apoptosis. As shown in Figures 5A and 5B, the number of $\gamma H2A.X^+$ cells increased dramatically in the neonatal mutant neocortex. Such increase was found even at E12.5 (Figure 5C), when the NSPC number was normal (Figures 3G, 3H, S6B, and S6C). TUNEL assays revealed that apoptosis increased in the mutant at both E14.5 (Figure 5D and 5E) and P0 (Figures 5F and 5G), with a massive amount of apoptotic cells in the mutant VZ/SVZ at E14.5 (Figures 5D and 5E). Immunostaining with an antibody recognizing activated caspase 3 also detected an increase of apoptosis in the mutant at both E14.5 and P0 (Figures 5H and 5I). Together, these results indicate that DNA damage and apoptosis contribute to NSPC depletion in the mutant.

Mutant NSPCs Are Impaired in Forming Neurospheres *In Vitro*

To investigate whether the residual mutant NSPCs are still functional, we conducted neurosphere formation assays, which have been widely used to determine NSPC potential *in vitro* (Singec et al., 2006). For these assays, we collected cerebral cortices from wild-type and mutant embryos at E16.5 to prepare single cell suspension for subsequent neurosphere formation in an NSC culture medium *in vitro*. Like the wild-type, single cells from the E16.5 mutant cerebral cortex formed round neurospheres in the first 4 days (Figure 6A), but the mutant neurospheres became irregular at day 6 and afterward (Figure 6B). Even at day 4, more dead cells were visible in the medium from the mutant neurospheres. Quantification revealed that at this time point, there were significantly fewer mutant neurospheres than the wild-type (Figure 6C). Measurement of neurosphere sizes indicated that, at days 4 and 9, the mutant neurospheres were significantly smaller than the wild-type (Figure 6D). Although there was no difference between the wild-type and heterozygous groups in terms of the total cell number, the homozygous mutant neurospheres contained fewer cells than the wild-type (Figure 6E).

We also collected wild-type and mutant cerebral cortices at E18.5 to grow neurospheres. Strikingly, those from the E18.5 mutant embryos were irregular even at day 4 of culturing (Figure 6F). To examine the NSC nature of neurospheres, we immunostained them with the anti-Sox2 antibody. As shown in Figure 6G, there was a high ratio of $Sox2^+$ cells in both wild-type and mutant neurospheres, confirming of their NSC nature. These results indicate that at E16.5 and E18.5, neurosphere formation from the mutant is impaired.

To investigate the impact of *Hdac3* inactivation on NSC self-renewal, we analyzed formation of secondary neurospheres. For this, primary neurospheres were cultured as described earlier and used for preparation of single-cell suspension through pipetting; 10,000 cells were used for neurosphere formation in the NSC

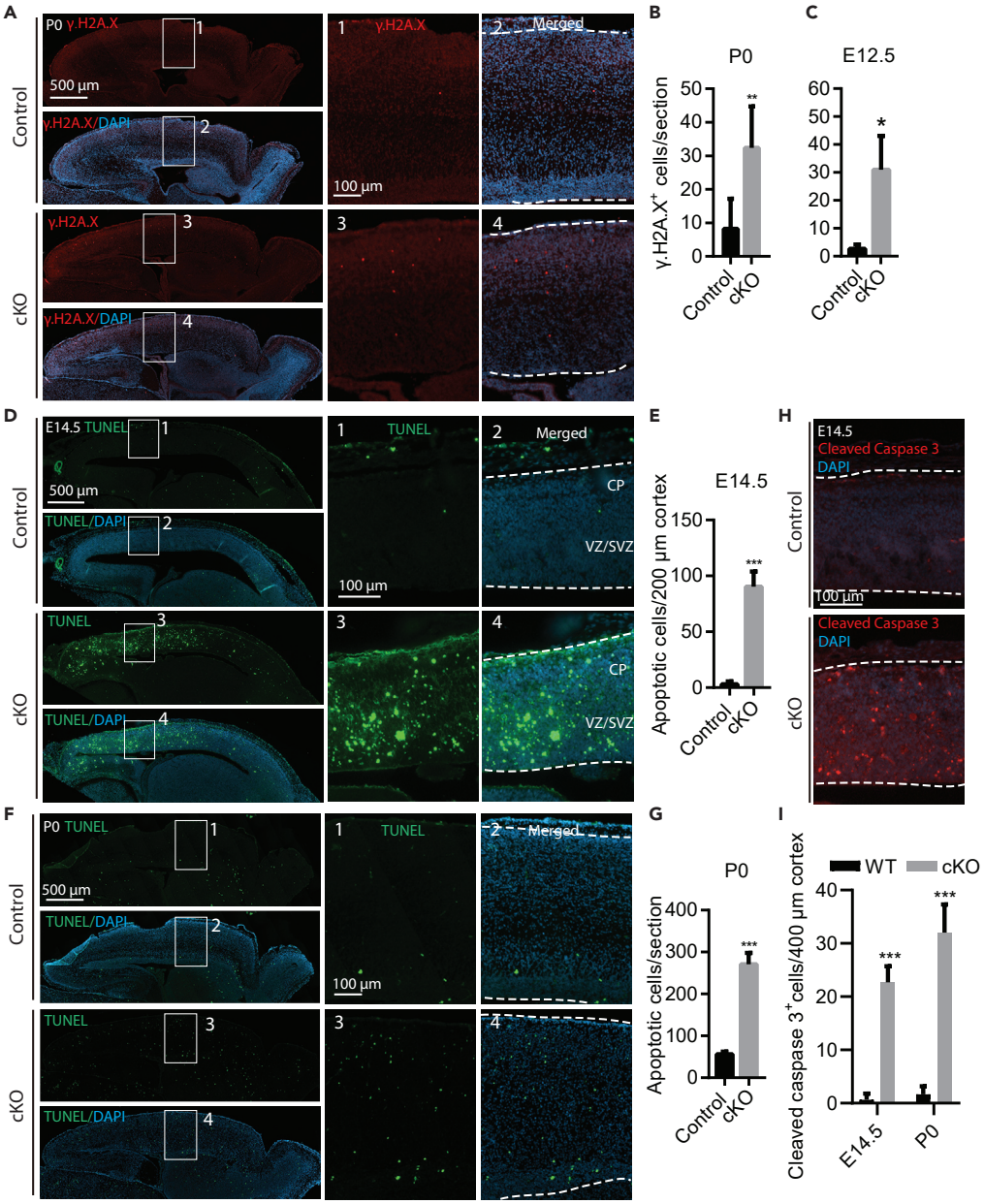

Figure 5. Cerebral *Hdac3* Loss Leads to DNA Damage and Apoptosis

(A) Immunostaining of wild-type and mutant neonatal brain sections with anti-γH2A.X antibody.

(B) Quantification of sections as shown in (A) indicated more γH2A.X$^+$ cells in the mutant cerebral cortex than in the wild-type (n = 3).

(C) Quantification of sections as in (B) except that E12.5 embryonic sections were analyzed (n = 3).

(D) TUNEL staining in control and cKO embryonic brain sections at E14.5.

(E) Quantification of TUNEL-positive cells in embryonic brain sections as shown in (D) (n = 3).

(F) TUNEL staining of control and cKO neonatal brain sections (n = 3).

(G) Quantification of TUNEL-positive cells in neonatal brain sections as shown in (F). n = 3.

(H) Immunostaining of control and cKO embryonic sections with an anti-activated caspase 3 antibody. Cerebral cortical areas are shown.

(I) Quantification of cells positive for activated caspase 3 in cerebral cortices at E14.5 and P0 (n = 3 for each group).

Scale bars, 500 μm for the left panels and 100 μm for the rest of the panels of (A), (D), and (F); and 100 μm for (H). *, $p < 0.05$; **, $p < 0.01$; ***, $p < 0.001$.

See also Figures S6D–S6G, S7, and S8.

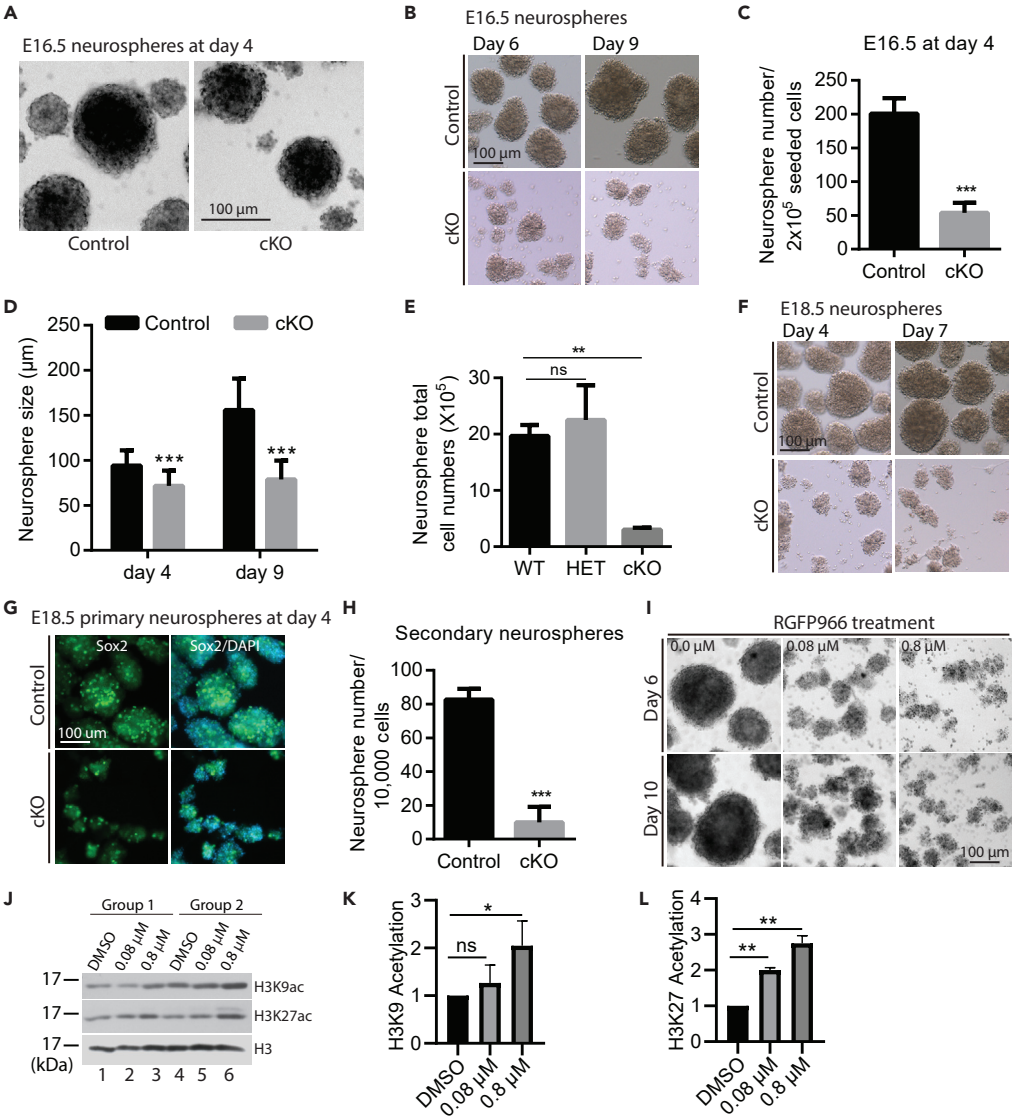

Figure 6. HDAC3 Is Essential for Neurosphere Formation *In Vitro*

(A) Normal round morphology of mutant neurospheres at day 4. In the first 4 days of culturing, the morphology of *Hdac3*-deficient neurospheres was similar to that of the wild-type counterparts.

(B) Photos of wild-type and mutant neurospheres at days 6 and 9 of culturing.

(C) Quantification of neurospheres formed from 2 × 10^5 single cells prepared from the E16.5 wild-type or mutant cerebral cortex (n = 3).

(D) Diameter of neurospheres grown for 4 days from the cerebral cortices of E16.5 control and mutant embryos (>50 neurospheres were measured for each group).

(E) Total cell number in neurospheres from wild-type, heterozygous (HET), and homozygous mutant (cKO) cerebral cortices. n = 5, 2, and 3 for the wild-type, heterozygous, and cKO groups, respectively.

(F) Morphology of E18.5 primary neurospheres at days 4 and 7 of culturing. Wild-type neurospheres were large and round, whereas the mutant ones were small and irregular.

(G) Microscopic photos of E18.5 neurospheres immunostained with anti-Sox2 antibody and counterstained with DAPI.

(H) Quantification of neurospheres formed from 10,000 single cells prepared from E18.5 wild-type or mutant primary neurospheres (n = 3).

(I) Treatment of E18.5 wild-type neurospheres using the HDAC3-specific inhibitor RGFP966 at 0, 0.08, and 0.8 μM for the indicated days. The IC50 value is 0.08 μM (Malvaez et al., 2013). The vehicle DMSO was maintained at the same amount for all conditions.

Figure 6. *Continued*

(J) Immunoblotting analysis of protein extracts from wild-type neurospheres treated with RGFP966 at 0, 0.08, and 0.8 μM. The inhibitor was added to the medium at ~12 h after neurosphere culturing started. After 24 h, cells were collected for immunoblotting with anti-acetylated histone H3 antibodies to detect changes of H3K9 and H3K27 acetylation.

Quantification of anti-H3K9 (K) and H3K27 (L) acetylation from two independent groups as shown in (J). For each sample, the acetylation levels were normalized to the total histone H3 level as the internal control. ns, not statistically significant; *, $p < 0.05$; **, $p < 0.01$; ***, $p < 0.001$. Scale bars, 100 micrometers for panels (A), (B), (F), (G) and (I).

medium. As shown in Figure 6H, single cells prepared from the mutant neurospheres yielded a much smaller number of neurospheres, indicating impairment of self-renewal in the mutant NSCs.

HDAC3 is a transcriptional coregulator with intrinsic deacetylase activity (Emiliani et al., 1998; Yang et al., 1997), so we took a pharmacological approach to substantiate the above-mentioned conclusions drawn from genetically modified NSPCs. For this, we utilized an HDAC3-specific inhibitor, RGFP966 (Malvaez et al., 2013). Single cell suspension was prepared from E16.5 wild-type cerebral cortex for neurosphere formation in the presence or absence of this inhibitor. As shown in Figure 6I, treatment with this inhibitor even at the IC50 value of 0.08 μM was sufficient for interfering with neurosphere formation, indicating that HDAC3 inhibition abolishes neurosphere formation. These results support that HDAC3 is essential for NSPC homeostasis.

Hdac3 Deletion Alters Epigenetic Marks Differently in the Cerebrum and Neurospheres

To shed light on how *Hdac3* deletion affects cerebral development and NSPC homeostasis, we asked how cerebrum-specific *Hdac3* deletion may alter the epigenome. We thus determined levels of histone marks using western blotting analyses with various histone modification-specific antibodies. Protein extracts of cerebral cortices were prepared from wild-type and mutant pups at P4, because at this stage the mutant pups were still grossly normal (Figures 1A–1C). For histone H3, the levels of the marks H3K9ac, H3K18ac, and H3K27ac, but not H3K4ac, H3K14ac, and H3K23ac, increased in the mutant cerebral cortex (Figure 7A, left and middle panels). Interestingly, the H3K14pr level also increased. Consistent with the increased levels of H3K9ac and H3K27ac, trimethylation at both sites, but not H3K4, decreased (Figure 7A, middle panels). Notably, the decrease at the H3K27me3 level was much more dramatic than at H3K9me3 (Figure 7A, middle panels). Consistent with this, immunostaining of brain sections revealed that the H3K27me3 level decreased in the mutant cerebral cortex, whereas the change was not so obvious for H3K9me3 (Figure S9). As with histone H3, histone H4 was also hyperacetylated (Figure 7A, right top panel). In support of this, the H4K16ac level increased in the mutant cerebral cortex (Figure 7A, right bottom panel). Moreover, the H4K16pr level increased as well. These results indicate that cerebrum-specific *Hdac3* deletion causes histone Hyperacetylation and hyperpropionylation and deregulates other histone modifications in the cerebrum.

We also performed western blotting with protein extracts from wild-type and mutant neurospheres. As shown in Figure 7B (bottom left two panels), *Hdac3* was efficiently deleted in neurospheres. This is consistent with the results for the cerebral cortex (Figure 1E) and its embryonic precursors (Figures S1A–S1I). As expected, H3K4 acetylation slightly increased, whereas H3K9 or H3K27 acetylation increased in the mutant neurospheres (Figure 7B, top left panels). This increase was also evident in neurospheres by treatment with the HDAC3 inhibitor (Figures 6J–6L). Unexpectedly, instead of hyperacetylation observed with the mutant cerebral cortex (Figure 7A), H3K14, H3K18, and H3K23 acetylation decreased in the mutant neurospheres (Figure 7B, middle left panels), perhaps due to indirect effects. As for methylation, the H3K4me3 level decreased, the H3K9me3 level increased, and the K3K27me3 level remained unaltered in the mutant neurospheres (Figure 7B, bottom left panels). About histone H4, its total acetylation level decreased in the mutant neurospheres, whereas the H4K16ac level was not altered (Figure 7B, right panels). Thus, unlike what was observed with the cerebral cortex (Figure 7A), *Hdac3* deletion causes histone hypoacetylation at some sites in neurospheres (Figure 7B). Differential impact in the cerebrum and neurospheres suggests cell type-specific effects.

HDAC3 Regulates Different Transcription Programs in the Cerebrum and Neurospheres

To identify molecular mechanisms by which *Hdac3* deletion affects cerebral development and NSPC homeostasis, we performed transcriptomic analyses. For this, we extracted total RNA from cerebral cortices from wild-type and mutant newborns (P0). Poly(A) RNA profiling revealed altered transcription

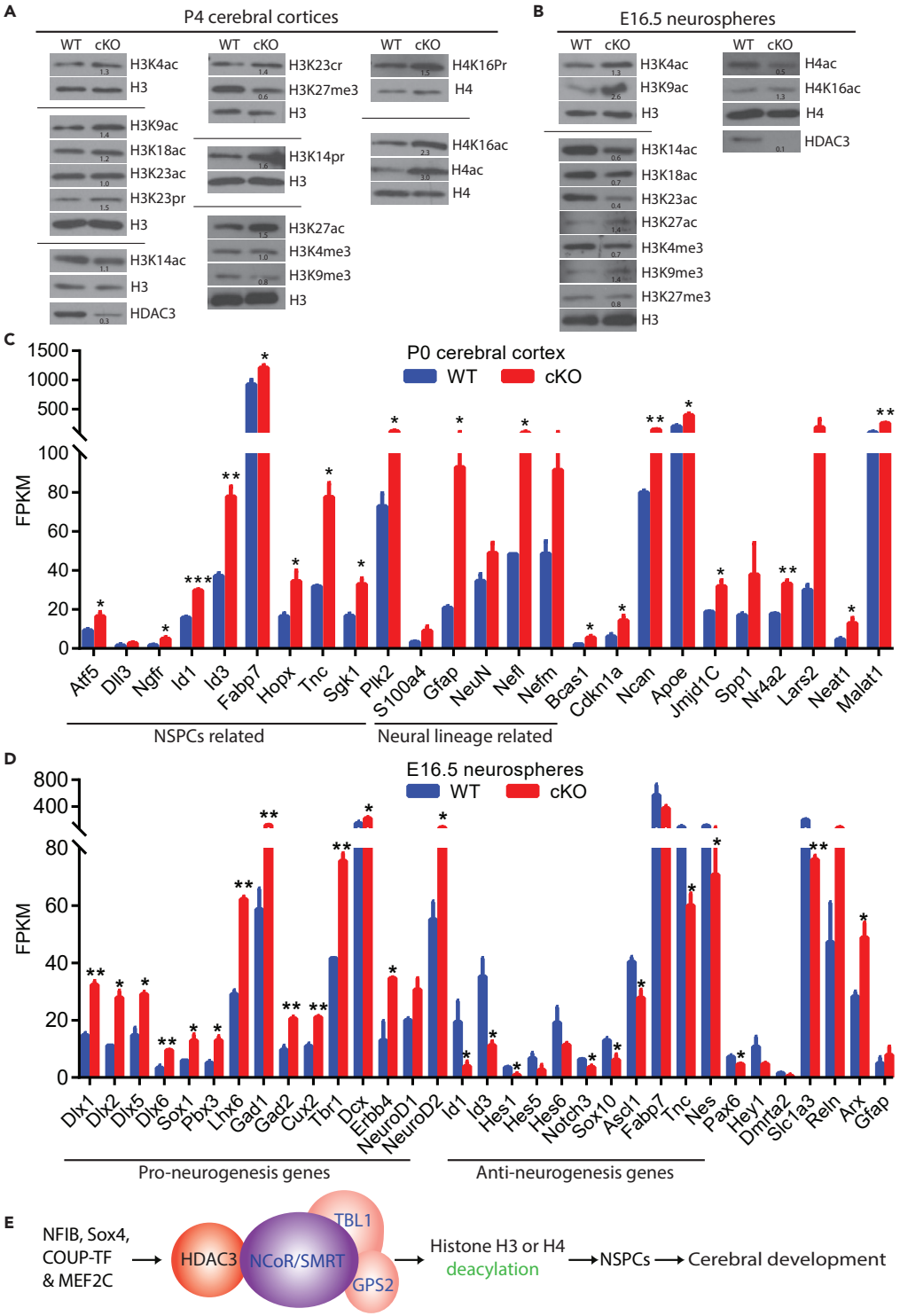

Figure 7. *Hdac3* Deletion Alters Epigenetic Marks in the Cerebral Cortex and Neurospheres

(A) Western blotting analysis of protein extracts from cerebral cortices of the control and mutant pups at P4. In agreement with Figures 1E and S1L, HDAC3 was efficiently deleted (compare the bottom two blots at the left). Modification-specific antibodies were used to detect changes of histone acetylation (ac), trimethylation (me3), propionylation (pr), and crotonylation (Cr). Notably, the deletion led to histone hyperacetylation, hyperpropionylation (e.g., H3K14pr and H4K16pr), and hypomethylation at multiple sites. Relative abundance of each modification was normalized to the

Figure 7. *Continued*

corresponding histone H3 or H4 level; the ratio of the normalized modification level in the mutant was then calculated against the wild-type and shown at the right of each blot. The blots were repeated at least once, with similar results.

(B) Same as (A) except that protein extracts were from neurospheres cultured from control and mutant cerebral cortices of E16.5 embryos.

(C) *Hdac3* deletion alters transcription of multiple genes related to NSPC and cell lineage development in neonatal cerebral cortex. Illustrated are FPKM values of genes related to NPSC and neural lineage development, as well as other genes important for brain development. The values were from RNA-seq of wild-type and mutant neonatal cerebral cortices (n = 2 for each group).

(D) *Hdac3* loss deregulates transcription of multiple genes related to neurogenesis in neurospheres. Illustrated are FPKM values of pro- and anti-neurogenesis genes, as well as some other genes related to NSC function (based on RNA-seq of wild-type and mutant neurospheres cultured from E16.5 cerebral cortices for 4 days *in vitro* [n = 2 for each group]). Fragments Per Kilobase of transcript per Million mapped reads (FPKM) values in (C and D) are from Tophat analysis (complete tables available from GSE133195).

(E) A model on how specific DNA-binding transcription factors may recruit HDAC3 and its associated subunits for genomic locus-specific deacylation (including deacetylation and depropionylation) during NSPC and cerebral development. Other transcription factor partner candidates include c-Jun and HIF1, both of which are not only highly expressed in the neonatal cerebral cortex and E16.5 neurospheres (GSE133195) but also able to interact with the HDAC3 complexes via GPS2 in non-neural tissues (Drareni et al., 2018; Fan et al., 2016).

See also Tables S2 and S3 and Figures S9–S12.

of multiple genes related to NSPC or lineage cell development (Figure 7C). With the Log_2FC (fold change) value of 0.8 as the cutoff, we identified 58 upregulated genes and 58 downregulated genes (see analysis results at GEO: GSE133195). The top upregulated gene is *Gfap*, with *Ngfr* at the fifth and two non-coding RNA genes, *Neat1* and *Malat1*, at the sixth and seventh positions, respectively. To evaluate the quality of RNA-seq datasets, we selected 19 significantly upregulated genes and 1 downregulated gene for validation by RT-qPCR. As shown in Figures S11A–S11D, the validation success rate was 75%, attesting to the quality of the datasets. In particular, RT-qPCR detected a dramatic increase in *Gfap* expression (Figure S11A), consistent with immunostaining results showing increased astrogliogenesis in the mutant brain sections at P0 (Figures S5D–S5F). This is in agreement with what was reported (Norwood et al., 2014). However, the pan-HDAC inhibitor trichostatin A reduces *GFAP* expression in primary human astrocytes and astrocytoma cells (Kanski et al., 2014), so other HDACs may be required for the expression. Among the other validated candidates are *Ngfr, Tnc, Bcas1, Nefl, Hopx, Sgk1, Nr4a2, Id1, Atf5, and Sox1* (Figures S11A and S11B), most of which have known roles in the brain. The non-coding RNA genes *Neat1* and *Malat1* were also validated (Figures S11A–S11D), suggesting their possible roles in cerebral development.

To draw further insights from RNA-seq datasets, we carried gene ontology (GO) analysis. The Log_2FC value of 0.8 was used as the cutoff to select top upregulated or downregulated genes for analyses via Enrichr (Kuleshov et al., 2016) and Metascape (Zhou et al., 2019b). Consistent results were obtained by both bioinformatic tools. The results indicated that neuropeptide signaling pathway (GO: 0007218), positive regulation of neuron differentiation (GO:0045666), negative regulation of neuron differentiation (GO:0045665), generation of neurons (GO:0048699), and regulation of neuron differentiation (GO:0045664) were among the top 15 GO categories affected in the mutant neonatal cerebral cortex, with p values ranging from 0.0015 to 5.8×10^{-5}. Related to neuropeptide signaling pathway, *Ngfr* was one of the top upregulated gene, as supported by RT-qPCR results (Figures S11A).

To dissect out the molecular mechanisms further, we extracted RNA from E16.5 primary neurospheres cultured at day 4, when the morphology was similar between wild-type and mutant neurospheres (Figure 6A). RNA-seq and gene differential analysis identified 68 upregulated (fold change>2) and 75 downregulated (fold change<0.5) genes (Tables S2 and S3), including increased transcription of pro-neurogenesis genes such as the *Dlx* family genes and decreased transcription of anti-neurogenesis genes such as the *Id* and *Hes* family genes (Figure 7D). These changes were supported by RT-qPCR (Figures S11E–S11F). To evaluate the quality of RNA-seq datasets, we selected 11 upregulated genes and 5 downregulated genes for validation by RT-qPCR. As shown in Figures S11E and S11F, the success rate was 94%, attesting to the quality of the datasets. Transcript levels of many other neurogenesis-promoting genes (such as *Sox1*, *Pbx*, *Lhx6*, *Gad1*, *Gad2*, *Cux2*, *Tbr1*, *Dcx*, *Erbb4*, *NeuroD1*, and *NeuroD2*) increased, whereas the levels of some anti-neurogenesis genes (such as *Notch3*, *Sox10*, *Ascl1*, *Tnc, and Nes*) decreased (Figure 7D). These results indicate that *Hdac3* deletion upregulates the expression of multiple pro-neurogenesis genes and inhibits the expression of some anti-neurogenesis genes. Extracellular matrix organization (GO:0030198),

regulation of cell migration (GO:0030334), extracellular matrix disassembly (GO:0022617), central nervous system development (GO:0007417), and brain development (GO:0007420) were among the top 17 affected GO categories, with p values ranging from to 2.7×10^{-5} to 1.3×10^{-16}.

Consistent with immunostaining with anti-BrdU and -Ki67 antibodies at E12.5 and E13.5 (Figures S6D–S6G), expression of cell cycle inhibitors such as *p27*, *p57*, *p15*, and *p53* was not affected in the mutant P0 cerebral cortex or E16.5 neurospheres (Figures S10A and S10B). *p21* (a.k.a. *Cdkn1a*) transcription increased in the *Hdac3*-deficient P0 cerebral cortex by ~2-fold (Figures S10A and S10B), whereas *p18* expression only decreased slightly in E16.5 mutant neurospheres (Figure S10B). Moreover, the *p53* and *Ki67* transcript levels were not significantly affected in the mutants (Figures S10A and S10B). These results indicate that overall proliferation is not dramatically affected in the mutant cerebral cortex or neurospheres. As the results are from bulk RNA-seq and RT-qPCR, effects at specific cerebral regions or cell types remain possible. Indeed, there were some effects on the $Ki67^+$ cell number at E15.6 and E16.5 (Figure S8).

HDAC3 Binds Multiple Transcription Factors Abundant in the Cerebrum and Neurospheres

As an enzymatic transcriptional coregulator (Yoon et al., 2003; Zhang et al., 2002), HDAC3 is recruited to specific promotors for gene-specific regulation. To identify DNA-binding transcription factors that target it to specific genetic loci during cerebral development, we analyzed public ChIP-seq datasets on HDAC3 (Armour et al., 2017; Emmett et al., 2017; He et al., 2018; Hong et al., 2017; Nanou et al., 2017; Remsberg et al., 2017). DNA sequence motif analysis identified multiple potential candidates, including MEF2, COUP-TFI, nuclear factor-I (e.g., NFIB and NFIC), SOX4, and C/EBPγ. Important for brain development (Heng et al., 2015; Ohtaka-Maruyama et al., 2013), RP58 contains a POZ domain that may interact with the NCoR/SMRT corepressors (Huynh and Bardwell, 1998), so we included this repressor as a candidate. According to RNA-seq, *Rp58*, *Nfib*, *Coup-tfi*, *Sox4*, and *Mef2c* are well expressed in the cerebral cortex (Figure S12A) and neurospheres (Figure S12B). Immunostaining showed that NFIB is abundant in the cortical plate and SVZ/VZ zone at E16.5 but not in the immediate zone (Figure S12C, topper panel). *Hdac3* deletion altered this distribution pattern and made it an even distribution in the cerebral cortex (Figure S12C, lower panel). These results indicate that HDAC3 affects NFIB expression in different cerebral areas during brain development.

Because MEF2C is a known binding partner of HDAC3 (Grégoire et al., 2007), we assessed the interaction of HDAC3 with NFIB and the other transcription factors mentioned earlier. FLAG-tagged HDAC3 was expressed with HA-tagged NFIB, NFIC, SOX4, C/EBPγ, and RP58 in HEK293 cells for co-immunoprecipitation. As shown in Figure S12D, HDAC3 co-immunoprecipitated NFIB, NFIC, and SOX4. Moreover, HDAC3 interacted with a truncated form of NFIB containing its N-terminal 200 residues (Figure S12D, lane 3). This region is conserved among NFIB, NFIC, and other NFI proteins (Figure S12E), suggesting that HDAC3 interacts with different NFI proteins. We also expressed FLAG-tagged HDAC3 alone in HEK293 cells to detect its interaction with endogenous COUP-TFI, NFIB, and RP58 proteins using antibodies against these proteins. As shown in Figures S12F–S12J, FLAG-tagged HDAC3 co-immunoprecipitated endogenous COUP-TFI and NFIB. The results suggest that several transcription factors, including NFI, COUP-TFI, and SOX4, recruit HDAC3 for gene-specific gene regulation during cerebral development.

DISCUSSION

This study uncovers an important role of *Hdac3* in governing perinatal cerebral development through NSPCs. Immunostaining revealed that HDAC3 is highly expressed in the developing mouse brain (Figure S1). Cerebrum-specific inactivation of the gene induces hyperactivity, anxiety, and early lethality in the pups, along with severe developmental defects such as neocortical disorganization, hippocampal hypoplasia, and callosal agenesis (Figure 1). As for the underlying cellular mechanisms, immunofluorescence microscopy revealed rapid loss of NSCs (Figure 3) and neuronal progenitors (Figure 4), resulting from premature neurogenesis (Figure S7) and enhanced DNA damage and apoptosis (Figure 5). Mutant NSPCs were also ectopically distributed to the cortical plate (Figures 3 and 4 and S8B–S8F). They were also defective in forming neurospheres *in vitro* (Figures 6A–6F), and an HDAC3-specific inhibitor abolished neurosphere formation by wild-type NSPCs (Figure 6I). Related to the molecular mechanisms (Figure 7), immunoblotting unveiled alteration of histone modifications in the mutant cerebral cortex and neurospheres (Figures 7A and 7B). Furthermore, RNA-seq not only revealed perturbation of transcription programs in the mutant cerebral cortex and neurospheres (Figures 7C and 7D) but also unmasked high expression of multiple HDAC3-interacting transcription factors in the wild-type cerebrum and neurospheres

(Figures S12A and S12B). These results identify HDAC3 as a deacetylase critical for perinatal cerebral and NSPC development (Figure 7E).

These results complement and extend a recent report on the role of *Hdac3* in brain development (Norwood et al., 2014). In the report, the *Nestin-Cre* strain was used and the resulting ablation induced neonatal lethality, thereby preventing analyses of neocortical development within the first 2 weeks after birth, when neocortical lamination occurs dynamically (Caviness et al., 2008). This *Cre* strain is also inefficient for inducing excision at E12.5–14.5 (Liang et al., 2012; Liang et al., 2013), whereas the *Emx1-Cre* line used herein confers efficient excision specifically in the neural stem/progenitor cells and cortical neurons starting at E12.5 (Figure S1F) (Gorski et al., 2002). Owing to cerebrum-specific expression, the resulting mutant pups survived for ~4 weeks (Figure 1A), permitting systematic analysis of neocortical and hippocampal development at different time points before and after birth. Several reports have described *Hdac3* deletion in the adult brain and showed that HDAC3 is important for learning and memory (McQuown et al., 2011; Nott et al., 2016), motor coordination (Norwood et al., 2014; Nott et al., 2016), social behavior (Nott et al., 2016), and drug addiction (Rogge et al., 2013). HDAC3 is also important for glial cell fate determination (Zhang et al., 2016) and myelin growth and regeneration (He et al., 2018). The present study highlights an important role of HDAC3 in prenatal neocortical and NSPC development. No reports have been made about the function of HDAC3 in the development of the hippocampus and corpus callosum, so our study fills the knowledge gap.

Our results showed that cerebrum-specific deletion of *Hdac3* promotes premature neurogenesis (Figure S7). Moreover, in the mutant neurospheres, expression of pro-neurogenesis genes (such as *Dlx* family members) was upregulated, whereas expression of anti-neurogenesis genes was downregulated (such as *Id* and *Hes* family members) (Figures 7D, S11E, and S11F). These results are consistent with a recent report showing that *Hdac3* knockdown initiates a neuronal differentiation program *in vitro* (Castelo-Branco et al., 2014). HDAC3 is the catalytic subunit of tetrameric complexes composed of NCoR (or SMRT), TBL1 (or its two paralogs), and GPS2 (Karagianni and Wong, 2007; Oberoi et al., 2011). These complexes function as transcriptional corepressors upon transcription factor-dependent recruitment to specific promotors. Consistent with the important role of HDAC3 in NSPCs (Figures 2, 3, and 4), $Smrt^{-/-}$ embryos display NSC defects (Jepsen et al., 2007) and $Ncor^{-/-}$ NSCs show enhanced astrogliogenesis *in vitro* (Hermanson et al., 2002). In agreement with premature astrogliogenesis upon *Ncor* deletion, *Gfap* transcription was elevated in $Hdac3^{-/-}$ neurospheres (1.5-fold) and cerebral cortices (4.3-fold). Moreover, immunostaining detected strong GFAP signals in $Hdac3^{-/-}$ cerebral cortices (Figures S5D–S5F). As shown in Figures S10C and S10D, both *Ncor* and *Smrt* are highly expressed in the wild-type cerebral cortex and neurospheres, suggesting redundant roles of these two paralogs. Together with the published reports on mouse *Ncor* (Hermanson et al., 2002) and *Smrt* (Jepsen et al., 2007), this study supports a model in which HDAC3 complexes govern pre- and postnatal NSPC and cerebral development (Figure 7E). Further genetic studies are needed to pinpoint the exact roles of different subunits in regulating cerebral development.

As for DNA-binding proteins that recruit these complexes for gene-specific action, RNA-seq uncovered high expression of multiple HDAC3-interacting transcription factors, including NFIB, COUP-TFI, and MEF2C, in the wild-type cerebrum and neurospheres (Figures S12A and S12B). These transcription factors are important in NSC maintenance and differentiation. For example, NFIB proteins are master regulators of neuronal differentiation (Becker-Santos et al., 2017). Disruption of *Nr2f1* and *Nr2f2* (encoding COUP-TFI and COUP-TFII, respectively) promotes neurogenesis and generation of early-born neurons in NSPCs and the developing forebrain (Naka et al., 2008). COUP-TFI is also important for oligodendrocyte differentiation (Yamaguchi et al., 2004). Co-immunoprecipitation confirmed the interaction of HDAC3 with NFIB and COUP-TFI (Figures S12D–S12I). MEF2C is important for NSPC development (Li et al., 2008) and interacts with HDAC3 (Grégoire et al., 2007). We thus propose that multiple DNA-binding proteins interact with and recruit HDAC3 complexes for epigenomic regulation during cerebral development (Figure 7E). Further studies with techniques such as bulk and single-cell ChIP-seq are needed to investigate how HDAC3 and its associated subunits are targeted to different genomic loci for governing development of the cerebrum and NSPCs.

HDAC3 complexes interact with MeCP2 (Kruusvee et al., 2017; Nott et al., 2016). RNA-seq revealed low *Mecp2* expression in the developing cerebrum and cultured neurospheres (Figures S12A and S12B). Defects of $Mecp2^{-/-}$ mice are much milder (Chen et al., 2001; Guy et al., 2001) than those of the *Hdac3*

knockouts described here (Figure 1), suggesting that MeCP2 is not a major DNA-binding partner of HDAC3 during brain development. Rev-ErbA and Rev-ErbB are important transcription factors mediating functions of HDAC3 in controlling circadian clock and metabolism (Bugge et al., 2012). RNA-seq detected low expression of *Rev-erba* and *Rev-erbb* in the neonatal cerebrum and E16.5 neurospheres (Figures S12A and S12B), indicating that these two are not major transcription factors mediating HDAC3 functions during cerebral development.

The important role of HDAC3 in mouse cerebral development (Figure 1) begs the question whether this epigenetic regulator is essential for human cerebral and intellectual development. Consistent with the neocortical and hippocampal defects of *Hdac3* knockout mice, five patients with *HDAC3*, *NCOR1*, or *NCOR2* mutations are associated with cerebral anomalies and intellectual disability (Helbig et al., 2016; Zhou et al., 2019a). Moreover, multiple patients with *TBL1XR1* mutations show intellectual disability (Heinen et al., 2016; Laskowski et al., 2016; Saitsu et al., 2014). Clinical features from these cohorts of patients shed light on potential problems of *GPS2* mutations, even though such individuals have not been reported yet. The developmental defects described herein for the mutant mice serve a valuable guide for analysis of cerebrum-related clinical features in patients with mutations in the genes for HDAC3 and its associated subunits (Figure 7E). Such defects in mutant mice suggest a prenatal developmental origin for some clinical features in patients.

There are 18 human HDACs (Haberland et al., 2009; Yang and Seto, 2008b), so a key question is how each HDAC contributes to epigenomic regulation during cerebral development. The results described herein highlight the importance of HDAC3 in this regard. Published studies have identified important roles of HDAC1, HDAC2, HDAC4, and HDAC8 in the brain (Deardorff et al., 2012; Yang and Seto, 2008b). Among them, HDAC4 shows little detectable deacetylase activity and HDAC8 deacetylates cohesion (Deardorff et al., 2012; Yang and Seto, 2008b), so HDAC1 and HDAC2 are two deacetylases targeting histones in the brain. Mouse *Hdac1* and *Hdac2* have redundant roles in regulating brain development (Montgomery et al., 2009). Inactivation of both genes disrupts cell-cycle progression, leaving few S-phase cells (Montgomery et al., 2009). By contrast, BrdU incorporation was normal in $Hdac3^{-/-}$ neuroepithelia at E12.5 and E13.5 (Figures S6D–S6G). Although neuronal progenitors lacking *Hdac1* and *Hdac2* are defective in differentiation (Montgomery et al., 2009) and haploinsufficiency of *SIN3A* (encoding a subunit of an HDAC1/HDAC2 complex) inhibits cortical neurogenesis (Witteveen et al., 2016), *Hdac3* deletion promotes premature neurogenesis and NSPC depletion (Figures 3 and 4). These studies support that HDAC3 is complementary to HDAC1 and HDAC2 during cerebral development. Despite minimal impact of *Hdac3* deletion on expression of these two and other HDACs (Figures S10E and S10F), histones H3 and H4 are hyperacetylated in the mutant cerebral cortex (Figure 7A). In sum, this study identifies HDAC3 as a major deacetylase that regulates epigenetic and transcriptional programs important for perinatal cerebral and NSPC development in mice and perhaps also in humans.

Limitations of the Study

This study employs a mouse genetic approach that induces *Hdac3* deletion at E12.5. Deletion at such an early embryonic stage complicates analysis of the roles at the late stages of development as it would be difficult to assess which stage an effect really occurs. We utilized bulk RNA-seq for transcriptomic analysis, from which we cannot distinguish between direct and indirect effects. Such bulk analysis also fails to differentiate effects from different cell types, so single-cell RNA-seq approaches should be advantageous in the regard.

METHODS

All methods can be found in the accompanying Transparent Methods supplemental file.

SUPPLEMENTAL INFORMATION

Supplemental Information can be found online at https://doi.org/10.1016/j.isci.2019.09.015.

ACKNOWLEDGMENTS

This work was supported by research grants from Canadian Institutes of Health Research, Natural Sciences and Engineering Research Council of Canada, and the Cancer Research Society (to X.-J.Y.). L.L. received stipend support from the China Scholarship Council, the Clifford C.F. Wong Fellowship program at McGill

University, and a CIHR/FRSQ training grant. J.J. received a Jiangsu Government Scholarship for Overseas Studies, JiangSu, China (JS-2017-095).

AUTHOR CONTRIBUTIONS

L.L. carried out a majority of experiments, performed data analysis, and wrote the manuscript; J.J. performed RT-qPCR and repeated some immunostaining experiments for quantification; X.-J.Y. supervised the project and finalized the manuscript.

DECLARATION OF INTERESTS

The authors declare no competing financial interests.

Received: February 12, 2019
Revised: August 1, 2019
Accepted: September 11, 2019
Published: October 25, 2019

REFERENCES

Alenghat, T., Osborne, L.C., Saenz, S.A., Kobuley, D., Ziegler, C.G., Mullican, S.E., Choi, I., Grunberg, S., Sinha, R., Wynosky-Dolfi, M., et al. (2013). Histone deacetylase 3 coordinates commensal-bacteria-dependent intestinal homeostasis. Nature *504*, 153–157.

Armour, S.M., Remsberg, J.R., Damle, M., Sidoli, S., Ho, W.Y., Li, Z., Garcia, B.A., and Lazar, M.A. (2017). An HDAC3-PROX1 corepressor module acts on HNF4alpha to control hepatic triglycerides. Nat. Commun. *8*, 549.

Arnold, S.J., Huang, G.J., Cheung, A.F.P., Era, T., Nishikawa, S.I., Bikoff, E.K., Molnar, Z., Robertson, E.J., and Groszer, M. (2008). The T-box transcription factor Eomes/Tbr2 regulates neurogenesis in the cortical subventricular zone. Gene Dev. *22*, 2479–2484.

Becker-Santos, D.D., Lonergan, K.M., Gronostajski, R.M., and Lam, W.L. (2017). Nuclear factor I/B: a master regulator of cell differentiation with paradoxical roles in cancer. EBioMedicine *22*, 2–9.

Bhaskara, S., Chyla, B.J., Amann, J.M., Knutson, S.K., Cortez, D., Sun, Z.W., and Hiebert, S.W. (2008). Deletion of histone deacetylase 3 reveals critical roles in S phase progression and DNA damage control. Mol. Cell *30*, 61–72.

Bugge, A., Feng, D., Everett, L.J., Briggs, E.R., Mullican, S.E., Wang, F., Jager, J., and Lazar, M.A. (2012). Rev-erbalpha and Rev-erbbeta coordinately protect the circadian clock and normal metabolic function. Genes Dev. *26*, 657–667.

Castelo-Branco, G., Lilja, T., Wallenborg, K., Falcao, A.M., Marques, S.C., Gracias, A., Solum, D., Paap, R., Walfridsson, J., Teixeira, A.I., et al. (2014). Neural stem cell differentiation is dictated by distinct actions of nuclear receptor corepressors and histone deacetylases. Stem Cell Reports *3*, 502–515.

Cattaneo, E., and McKay, R. (1990). Proliferation and differentiation of neuronal stem cells regulated by nerve growth factor. Nature *347*, 762–765.

Caviness, V.S., Bhide, P.G., and Nowakowski, R.S. (2008). Histogenetic processes leading to the laminated neocortex: migration is only a part of the story. Dev. Neurosci. Basel *30*, 82–95.

Chen, R.Z., Akbarian, S., Tudor, M., and Jaenisch, R. (2001). Deficiency of methyl-CpG binding protein-2 in CNS neurons results in a Rett-like phenotype in mice. Nat. Genet. *27*, 327–331.

Chou, S.J., Perez-Garcia, C.G., Kroll, T.T., and O'Leary, D.D.M. (2009). Lhx2 specifies regional fate in Emx1 lineage of telencephalic progenitors generating cerebral cortex. Nat. Neurosci. *12*, 1381–1389.

Codina, A., Love, J.D., Li, Y., Lazar, M.A., Neuhaus, D., and Schwabe, J.W. (2005). Structural insights into the interaction and activation of histone deacetylase 3 by nuclear receptor corepressors. Proc. Natl. Acad. Sci. U S A *102*, 6009–6014.

Deardorff, M.A., Bando, M., Nakato, R., Watrin, E., Itoh, T., Minamino, M., Saitoh, K., Komata, M., Katou, Y., Clark, D., et al. (2012). HDAC8 mutations in Cornelia de Lange syndrome affect the cohesin acetylation cycle. Nature *489*, 313–317.

Drareni, K., Ballaire, R., Barilla, S., Mathew, M.J., Toubal, A., Fan, R., Liang, N., Chollet, C., Huang, Z., Kondili, M., et al. (2018). GPS2 deficiency triggers maladaptive white adipose tissue expansion in obesity via HIF1A activation. Cell Rep. *24*, 2957–2971.e6.

Ellis, P., Fagan, B.M., Magness, S.T., Hutton, S., Taranova, O., Hayashi, S., McMahon, A., Rao, M., and Pevny, L. (2004). SOX2, a persistent marker for multipotential neural stem cells derived from embryonic stem cells, the embryo or the adult. Dev. Neurosci. *26*, 148–165.

Emiliani, S., Fischle, W., Van Lint, C., Al-Abed, Y., and Verdin, E. (1998). Characterization of a human RPD3 ortholog, HDAC3. Proc. Natl. Acad. Sci. U S A *95*, 2795–2800.

Emmett, M.J., Lim, H.W., Jager, J., Richter, H.J., Adlanmerini, M., Peed, L.C., Briggs, E.R., Steger, D.J., Ma, T., Sims, C.A., et al. (2017). Histone deacetylase 3 prepares brown adipose tissue for acute thermogenic challenge. Nature *546*, 544–548.

Fan, R., Toubal, A., Goni, S., Drareni, K., Huang, Z., Alzaid, F., Ballaire, R., Ancel, P., Liang, N., Damdimopoulos, A., et al. (2016). Loss of the co-repressor GPS2 sensitizes macrophage activation upon metabolic stress induced by obesity and type 2 diabetes. Nat. Med. *22*, 780–791.

Farooq, M., Sulochana, K.N., Pan, X.F., To, J.W., Sheng, D., Gong, Z.Y., and Ge, R.W. (2008). Histone deacetylase 3 (hdac3) is specifically required for liver development in zebrafish. Dev. Biol. *317*, 336–353.

Feng, D., Liu, T., Sun, Z., Bugge, A., Mullican, S.E., Alenghat, T., Liu, X.S., and Lazar, M.A. (2011). A circadian rhythm orchestrated by histone deacetylase 3 controls hepatic lipid metabolism. Science *331*, 1315–1319.

Gorski, J.A., Talley, T., Qiu, M., Puelles, L., Rubenstein, J.L., and Jones, K.R. (2002). Cortical excitatory neurons and glia, but not GABAergic neurons, are produced in the Emx1-expressing lineage. J. Neurosci. *22*, 6309–6314.

Grégoire, S., Xiao, L., Nie, J., Xu, M., Wong, J., Seto, E., and Yang, X.J. (2007). Histone deacetylase 3 interacts and deacetylates myocyte enhancer factor 2. Mol. Cell. Biol. *27*, 1280–1295.

Guenther, M.G., Lane, W.S., Fischle, W., Verdin, E., Lazar, M.A., and Shiekhattar, R. (2000). A core SMRT corepressor complex containing HDAC3 and TBL1, a WD40-repeat protein linked to deafness. Genes Dev. *14*, 1048–1057.

Guenther, M.G., Barak, O., and Lazar, M.A. (2001). The SMRT and N-CoR corepressors are activating cofactors for histone deacetylase 3. Mol. Cell. Biol. *21*, 6091–6101.

Guy, J., Hendrich, B., Holmes, M., Martin, J.E., and Bird, A. (2001). A mouse Mecp2-null mutation causes neurological symptoms that mimic Rett syndrome. Nat. Genet. *27*, 322–326.

Haberland, M., Montgomery, R.L., and Olson, E.N. (2009). The many roles of histone deacetylases in development and physiology:

implications for disease and therapy. Nat. Rev. Genet. *10*, 32–42.

He, X., Zhang, L., Queme, L.F., Liu, X., Lu, A., Waclaw, R.R., Dong, X., Zhou, W., Kidd, G., Yoon, S.O., et al. (2018). A histone deacetylase 3-dependent pathway delimits peripheral myelin growth and functional regeneration. Nat. Med. *24*, 338–351.

Heinen, C.A., Jongejan, A., Watson, P.J., Redeker, B., Boelen, A., Boudzovitch-Surovtseva, O., Forzano, F., Hordijk, R., Kelley, R., Olney, A.H., et al. (2016). A specific mutation in TBL1XR1 causes Pierpont syndrome. J. Med. Genet. *53*, 330–337.

Helbig, K.L., Farwell Hagman, K.D., Shinde, D.N., Mroske, C., Powis, Z., Li, S., Tang, S., and Helbig, I. (2016). Diagnostic exome sequencing provides a molecular diagnosis for a significant proportion of patients with epilepsy. Genet. Med. *18*, 898–905.

Heng, J.I., Qu, Z., Ohtaka-Maruyama, C., Okado, H., Kasai, M., Castro, D., Guillemot, F., and Tan, S.S. (2015). The zinc finger transcription factor RP58 negatively regulates Rnd2 for the control of neuronal migration during cerebral cortical development. Cereb. Cortex *25*, 806–816.

Hermanson, O., Jepsen, K., and Rosenfeld, M.G. (2002). N-CoR controls differentiation of neural stem cells into astrocytes. Nature *419*, 934–939.

Hevner, R.F., Shi, L., Justice, N., Hsueh, Y., Sheng, M., Smiga, S., Bulfone, A., Goffinet, A.M., Campagnoni, A.T., and Rubenstein, J.L. (2001). Tbr1 regulates differentiation of the preplate and layer 6. Neuron *29*, 353–366.

Hodge, R.D., Nelson, B.R., Kahoud, R.J., Yang, R., Mussar, K.E., Reiner, S.L., and Hevner, R.F. (2012). Tbr2 is essential for hippocampal lineage progression from neural stem cells to intermediate progenitors and neurons. J. Neurosci. *32*, 6275–6287.

Hong, S., Zhou, W., Fang, B., Lu, W., Loro, E., Damle, M., Ding, G., Jager, J., Zhang, S., Zhang, Y., et al. (2017). Dissociation of muscle insulin sensitivity from exercise endurance in mice by HDAC3 depletion. Nat. Med. *23*, 223–234.

Huynh, K.D., and Bardwell, V.J. (1998). The BCL-6 POZ domain and other POZ domains interact with the co-repressors N-CoR and SMRT. Oncogene *17*, 2473–2484.

Jepsen, K., Solum, D., Zhou, T.Y., McEvilly, R.J., Kim, H.J., Glass, C.K., Hermanson, O., and Rosenfeld, M.G. (2007). SMRT-mediated repression of an H3K27 demethylase in progression from neural stem cell to neuron. Nature *450*, 415–U418.

Kanski, R., Sneeboer, M.A., van Bodegraven, E.J., Sluijs, J.A., Kropff, W., Vermunt, M.W., Creyghton, M.P., De Filippis, L., Vescovi, A., Aronica, E., et al. (2014). Histone acetylation in astrocytes suppresses GFAP and stimulates a reorganization of the intermediate filament network. J. Cell Sci. *127*, 4368–4380.

Karagianni, P., and Wong, J. (2007). HDAC3: taking the SMRT-N-CoRrect road to repression. Oncogene *26*, 5439–5449.

Knutson, S.K., Chyla, B.J., Amann, J.M., Bhaskara, S., Huppert, S.S., and Hiebert, S.W. (2008). Liver-specific deletion of histone deacetylase 3 disrupts metabolic transcriptional networks. EMBO J. *27*, 1017–1028.

Kruusvee, V., Lyst, M.J., Taylor, C., Tarnauskaite, Z., Bird, A.P., and Cook, A.G. (2017). Structure of the MeCP2-TBLR1 complex reveals a molecular basis for Rett syndrome and related disorders. Proc. Natl. Acad. Sci. U S A *114*, E3243–E3250.

Kuleshov, M.V., Jones, M.R., Rouillard, A.D., Fernandez, N.F., Duan, Q., Wang, Z., Koplev, S., Jenkins, S.L., Jagodnik, K.M., Lachmann, A., et al. (2016). Enrichr: a comprehensive gene set enrichment analysis web server 2016 update. Nucleic Acids Res. *44*, W90–W97.

Lai, T., Jabaudon, D., Molyneaux, B.J., Azim, E., Arlotta, P., Menezes, J.R., and Macklis, J.D. (2008). SOX5 controls the sequential generation of distinct corticofugal neuron subtypes. Neuron *57*, 232–247.

Laskowski, R.A., Tyagi, N., Johnson, D., Joss, S., Kinning, E., McWilliam, C., Splitt, M., Thornton, J.M., Firth, H.V., Study, D.D.D., et al. (2016). Integrating population variation and protein structural analysis to improve clinical interpretation of missense variation: application to the WD40 domain. Hum. Mol. Genet. *25*, 927–935.

Li, H., Radford, J.C., Ragusa, M.J., Shea, K.L., McKercher, S.R., Zaremba, J.D., Soussou, W., Nie, Z., Kang, Y.J., Nakanishi, N., et al. (2008). Transcription factor MEF2C influences neural stem/progenitor cell differentiation and maturation in vivo. Proc. Natl. Acad. Sci. U S A *105*, 9397–9402.

Li, L., Jayabal, S., Ghorbani, M., Legault, L.M., McGraw, S., Watt, A.J., and Yang, X.J. (2019). ATAT1 regulates forebrain development and stress-induced tubulin hyperacetylation. Cell. Mol. Life Sci. *76*, 3621–3640.

Liang, H., Hippenmeyer, S., and Ghashghaei, H.T. (2012). A Nestin-cre transgenic mouse is insufficient for recombination in early embryonic neural progenitors. Biol. Open *1*, 1200–1203.

Liang, H., Xiao, G., Yin, H., Hippenmeyer, S., Horowitz, J.M., and Ghashghaei, H.T. (2013). Neural development is dependent on the function of specificity protein 2 in cell cycle progression. Development *140*, 552–561.

Lu, X.F., Cao, X.Y., Zhu, Y.J., Wu, Z.R., Zhuang, X., Shao, M.Y., Xu, Q., Zhou, Y.J., Ji, H.J., Lu, Q.R., et al. (2018). Histone deacetylase 3 promotes liver regeneration and liver cancer cells proliferation through signal transducer and activator of transcription 3 signaling pathway. Cell Death Dis. *9*, 398.

Malvaez, M., McQuown, S.C., Rogge, G.A., Astarabadi, M., Jacques, V., Carreiro, S., Rusche, J.R., and Wood, M.A. (2013). HDAC3-selective inhibitor enhances extinction of cocaine-seeking behavior in a persistent manner. Proc. Natl. Acad. Sci. U S A *110*, 2647–2652.

Marin, O., and Rubenstein, J.L. (2001). A long, remarkable journey: tangential migration in the telencephalon. Nat. Rev. Neurosci. *2*, 780–790.

McQuown, S.C., Barrett, R.M., Matheos, D.P., Post, R.J., Rogge, G.A., Alenghat, T., Mullican, S.E., Jones, S., Rusche, J.R., Lazar, M.A., et al. (2011). HDAC3 is a critical negative regulator of long-term memory formation. J. Neurosci. *31*, 764–774.

Molyneaux, B.J., Arlotta, P., Menezes, J.R., and Macklis, J.D. (2007). Neuronal subtype specification in the cerebral cortex. Nat. Rev. Neurosci. *8*, 427–437.

Montgomery, R.L., Potthoff, M.J., Haberland, M., Qi, X., Matsuzaki, S., Humphries, K.M., Richardson, J.A., Bassel-Duby, R., and Olson, E.N. (2008). Maintenance of cardiac energy metabolism by histone deacetylase 3 in mice. J. Clin. Invest. *118*, 3588–3597.

Montgomery, R.L., Hsieh, J., Barbosa, A.C., Richardson, J.A., and Olson, E.N. (2009). Histone deacetylases 1 and 2 control the progression of neural precursors to neurons during brain development. Proc. Natl. Acad. Sci. U S A *106*, 7876–7881.

Naka, H., Nakamura, S., Shimazaki, T., and Okano, H. (2008). Requirement for COUP-TFI and II in the temporal specification of neural stem cells in CNS development. Nat. Neurosci. *11*, 1014–1023.

Nanou, A., Toumpeki, C., Lavigne, M.D., Lazou, V., Demmers, J., Paparountas, T., Thanos, D., and Katsantoni, E. (2017). The dual role of LSD1 and HDAC3 in STAT5-dependent transcription is determined by protein interactions, binding affinities, motifs and genomic positions. Nucleic Acids Res. *45*, 142–154.

Nieto, M., Monuki, E.S., Tang, H., Imitola, J., Haubst, N., Khoury, S.J., Cunningham, J., Gotz, M., and Walsh, C.A. (2004). Expression of Cux-1 and Cux-2 in the subventricular zone and upper layers II-IV of the cerebral cortex. J. Comp. Neurol. *479*, 168–180.

Noctor, S.C., Flint, A.C., Weissman, T.A., Dammerman, R.S., and Kriegstein, A.R. (2001). Neurons derived from radial glial cells establish radial units in neocortex. Nature *409*, 714–720.

Norwood, J., Franklin, J.M., Sharma, D., and D'Mello, S.R. (2014). Histone deacetylase 3 is necessary for proper brain development. J. Biol. Chem. *289*, 34569–34582.

Nott, A., Cheng, J., Gao, F., Lin, Y.T., Gjoneska, E., Ko, T., Minhas, P., Zamudio, A.V., Meng, J., Zhang, F.R., et al. (2016). Histone deacetylase 3 associates with MeCP2 to regulate FOXO and social behavior. Nat. Neurosci. *19*, 1497–1505.

Oberoi, J., Fairall, L., Watson, P.J., Yang, J.C., Czimmerer, Z., Kampmann, T., Goult, B.T., Greenwood, J.A., Gooch, J.T., Kallenberger, B.C., et al. (2011). Structural basis for the assembly of the SMRT/NCoR core transcriptional repression machinery. Nat. Struct. Mol. Biol. *18*, 177–184.

Ohtaka-Maruyama, C., Hirai, S., Miwa, A., Heng, J.I., Shitara, H., Ishii, R., Taya, C., Kawano, H., Kasai, M., Nakajima, K., et al. (2013). RP58 regulates the multipolar-bipolar transition of newborn neurons in the developing cerebral cortex. Cell Rep. *3*, 458–471.

Remsberg, J.R., Ediger, B.N., Ho, W.Y., Damle, M., Li, Z., Teng, C., Lanzillotta, C., Stoffers, D.A., and Lazar, M.A. (2017). Deletion of histone deacetylase 3 in adult beta cells improves glucose tolerance via increased insulin secretion. Mol. Metab. *6*, 30–37.

Rogge, G.A., Singh, H., Dang, R., and Wood, M.A. (2013). HDAC3 is a negative regulator of cocaine-context-associated memory formation. J. Neurosci. *33*, 6623–6632.

Saitsu, H., Tohyama, J., Walsh, T., Kato, M., Kobayashi, Y., Lee, M., Tsurusaki, Y., Miyake, N., Goto, Y., Nishino, I., et al. (2014). A girl with West syndrome and autistic features harboring a de novo TBL1XR1 mutation. J. Hum. Genet. *59*, 581–583.

Singec, I., Knoth, R., Meyer, R.P., Maciaczyk, J., Volk, B., Nikkhah, G., Frotscher, M., and Snyder, E.Y. (2006). Defining the actual sensitivity and specificity of the neurosphere assay in stem cell biology. Nat. Methods *3*, 801–806.

Suganuma, T., and Workman, J.L. (2008). Crosstalk among histone modifications. Cell *135*, 604–607.

Summers, A.R., Fischer, M.A., Stengel, K.R., Zhao, Y., Kaiser, J.F., Wells, C.E., Hunt, A., Bhaskara, S., Luzwick, J.W., Sampathi, S., et al. (2013). HDAC3 is essential for DNA replication in hematopoietic progenitor cells. J. Clin. Invest. *123*, 3112–3123.

Sun, Z., Miller, R.A., Patel, R.T., Chen, J., Dhir, R., Wang, H., Zhang, D.Y., Graham, M.J., Unterman, T.G., Shulman, G.I., et al. (2012). Hepatic Hdac3 promotes gluconeogenesis by repressing lipid synthesis and sequestration. Nat. Med. *18*, 934–942.

Urban, N., and Guillemot, F. (2014). Neurogenesis in the embryonic and adult brain: same regulators, different roles. Front. Cell. Neurosci. *8*, 396.

Watson, P.J., Fairall, L., Santos, G.M., and Schwabe, J.W.R. (2012). Structure of HDAC3 bound to co-repressor and inositol tetraphosphate. Nature *481*, 335–340.

Witteveen, J.S., Willemsen, M.H., Dombroski, T.C., van Bakel, N.H., Nillesen, W.M., van Hulten, J.A., Jansen, E.J., Verkaik, D., Veenstra-Knol, H.E., van Ravenswaaij-Arts, C.M., et al. (2016). Haploinsufficiency of MeCP2-interacting transcriptional co-repressor SIN3A causes mild intellectual disability by affecting the development of cortical integrity. Nat. Genet. *48*, 877–887.

Yamaguchi, H., Zhou, C., Lin, S.C., Durand, B., Tsai, S.Y., and Tsai, M.J. (2004). The nuclear orphan receptor COUP-TFI is important for differentiation of oligodendrocytes. Dev. Biol. *266*, 238–251.

Yang, W.M., Yao, Y.L., Sun, J.M., Davie, J.R., and Seto, E. (1997). Isolation and characterization of cDNAs corresponding to an additional member of the human histone deacetylase gene family. J. Biol. Chem. *272*, 28001–28007.

Yang, X.J., and Seto, E. (2008a). Lysine acetylation: codified crosstalk with other posttranslational modifications. Mol. Cell *31*, 449–461.

Yang, X.J., and Seto, E. (2008b). The Rpd3/Hda1 family of lysine deacetylases: from bacteria and yeast to mice and men. Nat. Rev. Mol. Cell Biol. *9*, 206–218.

Yoon, H.G., Chan, D.W., Huang, Z.Q., Li, J.W., Fondell, J.D., Qin, J., and Wong, J.M. (2003). Purification and functional characterization of the human N-CoR complex: the roles of HDAC3, TBL1 and TBLR1. EMBO J. *22*, 1336–1346.

You, L., Yan, K., Zou, J., Zhao, H., Bertos, N.R., Park, M., Wang, E., and Yang, X.J. (2015a). The lysine acetyltransferase activator Brpf1 governs dentate gyrus development through neural stem cells and progenitors. PLoS Genet. *11*, e1005034.

You, L., Zou, J., Zhao, H., Bertos, N.R., Park, M., Wang, E., and Yang, X.J. (2015b). Deficiency of the chromatin regulator Brpf1 causes abnormal brain development. J. Biol. Chem. *290*, 7114–7129.

Zhang, J.S., Kalkum, M., Chait, B.T., and Roeder, R.G. (2002). The N-CoR-HDAC3 nuclear receptor corepressor complex inhibits the JNK pathway through the integral subunit GPS2. Mol. Cell *9*, 611–623.

Zhang, L.G., He, X.L., Liu, L., Jiang, M.Q., Zhao, C.T., Wang, H.B., He, D.Y., Zheng, T., Zhou, X.Y., Hassan, A., et al. (2016). Hdac3 interaction with p300 Histone acetyltransferase regulates the oligodendrocyte and astrocyte lineage fate switch. Dev. Cell *36*, 316–330.

Zhou, W., He, Y., Rehman, A.U., Kong, Y., Hong, S., Ding, G., Yalamanchili, H.K., Wan, Y.W., Paul, B., Wang, C., et al. (2019a). Loss of function of NCOR1 and NCOR2 impairs memory through a novel GABAergic hypothalamus-CA3 projection. Nat. Neurosci. *22*, 205–217.

Zhou, Y., Zhou, B., Pache, L., Chang, M., Khodabakhshi, A.H., Tanaseichuk, O., Benner, C., and Chanda, S.K. (2019b). Metascape provides a biologist-oriented resource for the analysis of systems-level datasets. Nat. Commun. *10*, https://doi.org/10.1038/s41467-41019-09234-41466.

ISCI, Volume *20*

Supplemental Information

Histone Deacetylase 3 Governs Perinatal Cerebral Development via Neural Stem and Progenitor Cells

Lin Li, Jianliang Jin, and Xiang-Jiao Yang

Figure S1

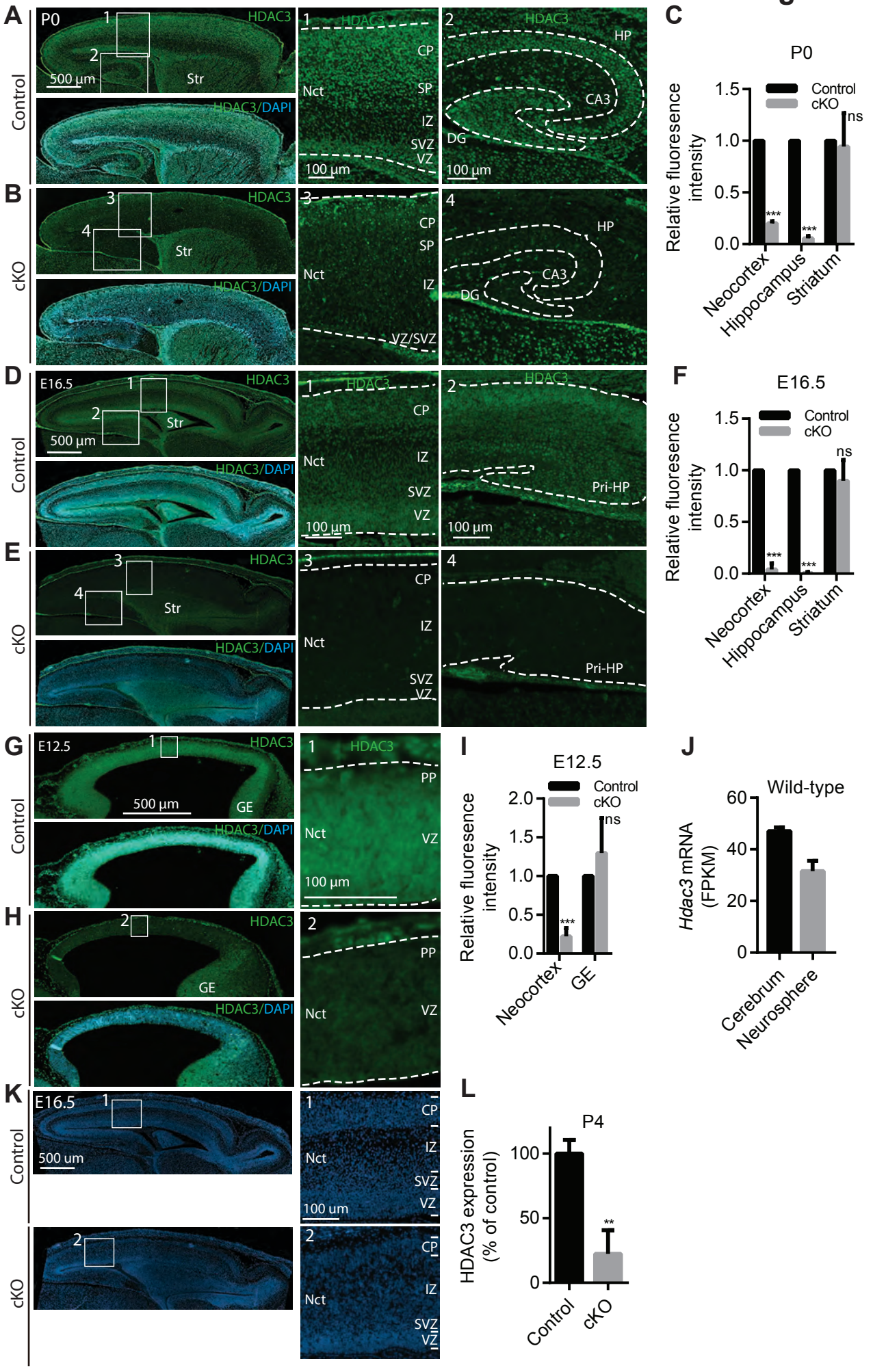
A
P0
HDAC3
Control
500 μm
Str
HDAC3/DAPI
CP
SP
Nct
IZ
SVZ
VZ
100 μm
HP
CA3
DG
B
cKO
C
P0
Control
cKO
Relative fluorescence intensity
ns
***
Neocortex
Hippocampus
Striatum
D
E16.5
E
F
E16.5
Pri-HP
G
E12.5
GE
PP
H
I
E12.5
J
Wild-type
Hdac3 mRNA (FPKM)
Cerebrum
Neurosphere
K
L
P4
HDAC3 expression (% of control)
**

Figure S1. Cerebral expression of *Hdac3* during development and its deletion in the mutant (related to Figure 1).

(A-B) Immunostaining of wild-type and mutant neonatal brain sections with anti-HDAC3 antibody. Enlarged images of the neocortices and hippocampi are shown at the right.

(**C**) Fluorescence intensity of HDAC3 in the neocortex, hippocampus or striatum, demarcated with dashed lines in (A-B), was measured with Image J (n=3 for each group). The respective fluorescence intensity in the wild-type was arbitrarily set to 1.0.

(D-E) Immunodetection of HDAC3 in the wild-type (**D**) and mutant (**E**) brain sections of E16.5 embryos. Enlarged images of the neocortices and hippocampi are shown at the right.

(**F**) Fluorescence intensity in the neocortex, hippocampal primordium and striatum, shown in (D-E), was measured as in (C). n=3 for each group.

(**G-H)** Immunostaining to detect HDAC3 in the wild-type (**G**) and mutant (**H**) E12.5 embryonic sections. Enlarged images of the neuroepithelia are shown at the right.

(**I**) Fluorescence intensity in the neocortex and ganglionic eminence, shown in (G-H), was measured as in (C). n=3 for each group.

(J) FPKM (fragments per kilobase of transcript per million mapped reads) values for *Hdac3* mRNA in the wild-type cerebral cortex at P0 and the wild-type NSPCs cultured from E16.5 embryos. The FPKM values are from Tophat analysis of RNA-Seq datasets (n=2).

(**K**) DAPI staining of E16.5 embryonic sections uncovered compression of the VZ/SVZ and disorganization of the mutant cerebral cortex.

(**L**) Quantification of the HDAC3 levels in the wild-type and mutant cerebral cortices. The immunoblot in Fig. 1E was quantified with Image J (n=3), and the average values are shown here.

Abbreviations: GE, ganglionic eminence; Pri-HP, hippocampal primordium; Str, striatum. Additional abbreviations are listed in the legend to Fig. 1. Scale bars, 500 μm for the left panels and 100 μm for the rest panels in (A-B), (D-E), G-H) & (K). ns, statistically not significant; **, $p<0.01$; ***, $p<0.001$.

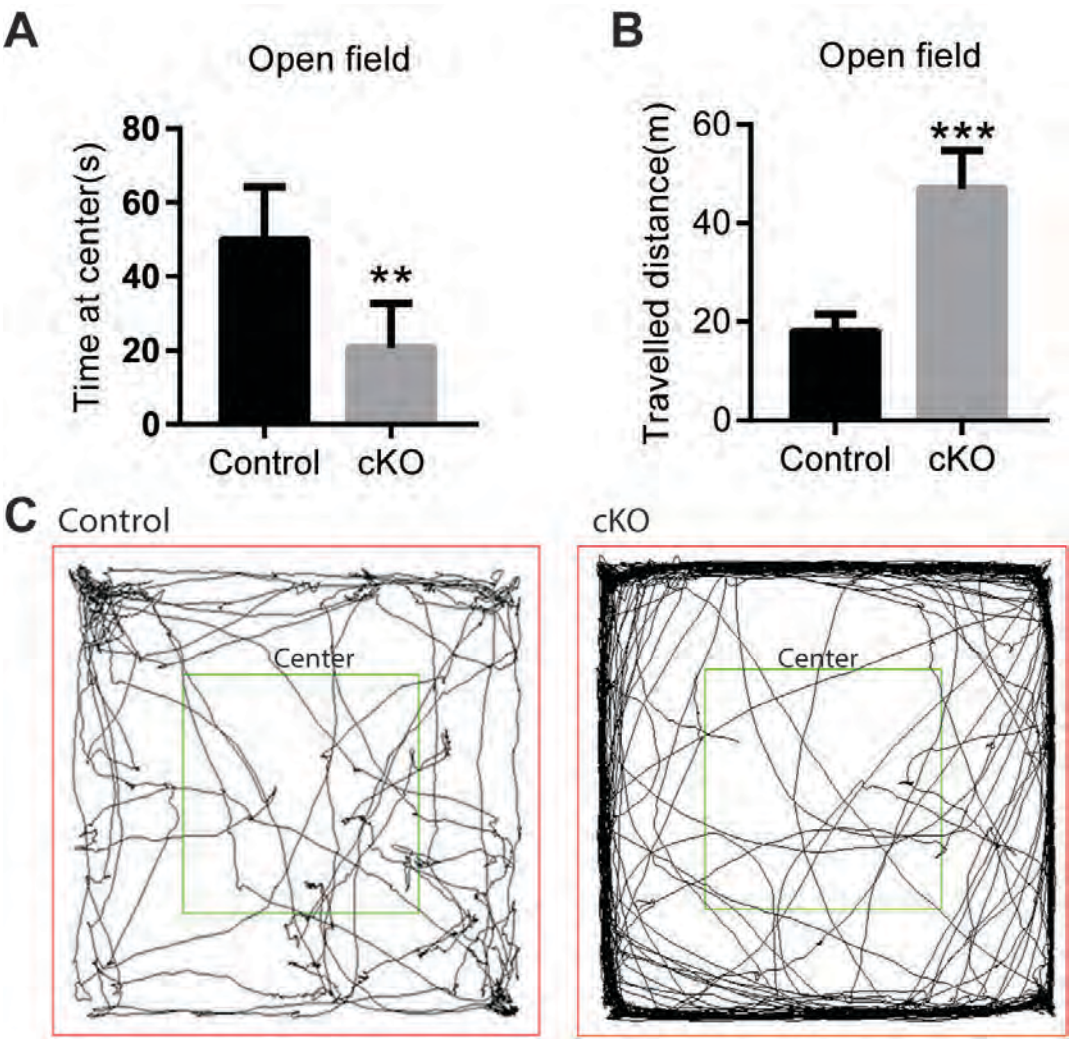

Figure S2. Anxiety and hyperactivity in the *Hdac3* knockouts (related to Figure 1).
(**A**) Open field tests of wild-type and mutant mice at P22. Time spent at the center of the test arena was significantly reduced in the mutant mice (n=6).
(**B**) Total distance that mutant mice travelled during open field tests was significantly increased (n=6).
(**C**) Representative trajectory maps for control and mutant mice at P22. Red boxes indicate open field arenas (40 cm x 40 cm), and the green boxes denote the centers of arenas (20 cm x 20 cm).

Figure S3

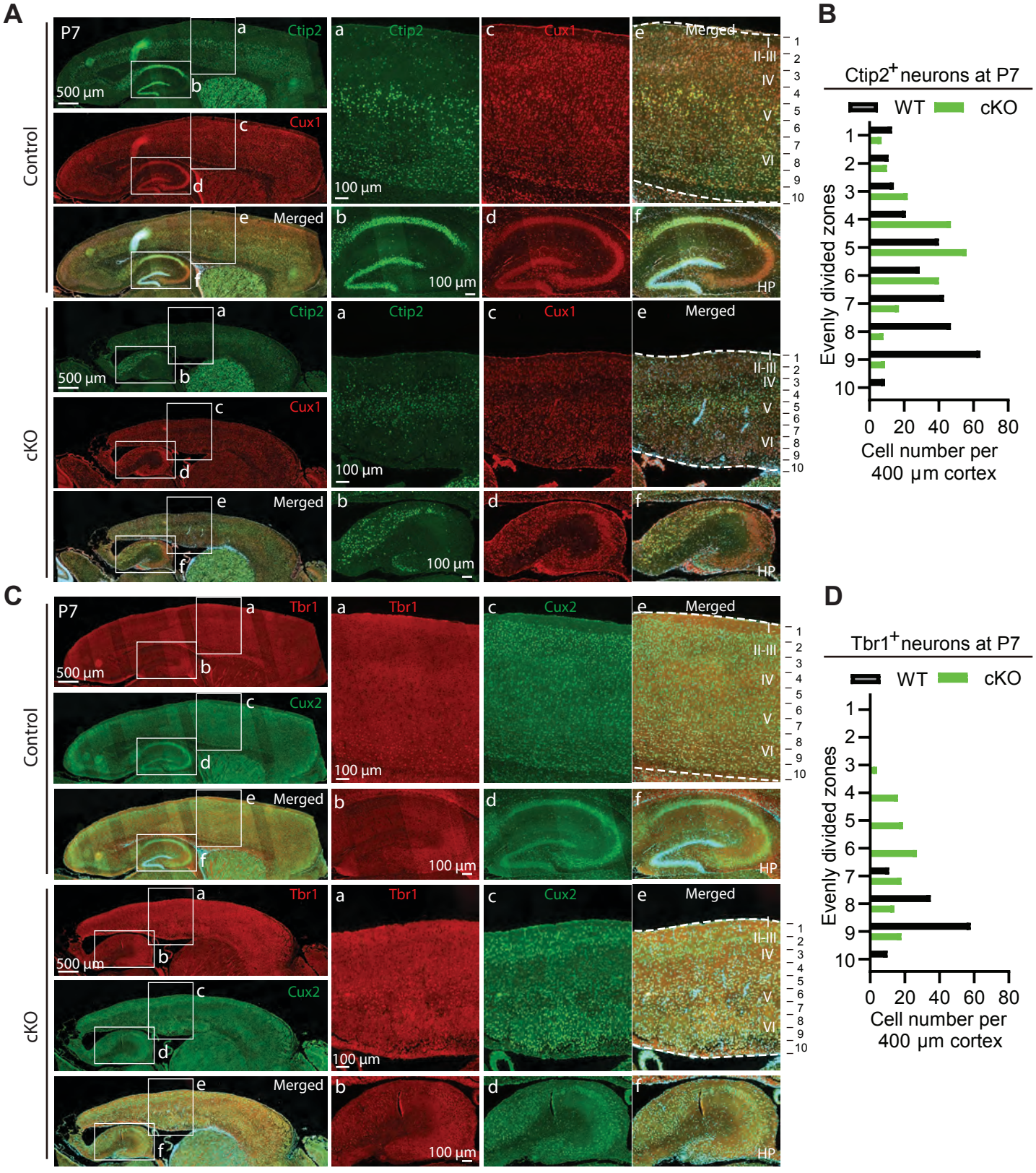
A
P7
Ctip2
Cux1
Merged
500 μm
100 μm
Control
cKO
HP
I
II-III
IV
V
VI
B
Ctip2+ neurons at P7
WT
cKO
Evenly divided zones
Cell number per 400 μm cortex
C
Tbr1
Cux2
D
Tbr1+ neurons at P7

Figure S3. Defective neocortical lamination and hippocampal development in the *Hdac3*-deficient brain at P7 (related to Figure 2).

(**A**) Co-immunostaining of wild-type and mutant P7 brain sections with anti-Cux1 and -Ctip2 antibodies. The former labels the SVZ and layers II-IV of adult neocortex (Nieto et al., 2004), whereas the latter marks layers V-VI (Lai et al., 2008). Scale bars, 500 μm for the left panels and 100 μm for the rest.

(**B**) The mutant neocortical layers are not clearly separated, so the wild-type or mutant neocortex was divided equally into 10 zones for determination of the $Ctip2^{+}$ cell distribution.

(**C-D**) Co-immunostaining of wild-type and mutant P7 brain sections with anti-Tbr1 and -Cux2 antibodies. The former labels layer VI in the adult neocortex (Hevner et al., 2001)) and the latter marks layers II-IV (Nieto et al., 2004). Scale bars, 500 μm for the left panels and 100 μm for the rest panels of (C).

Figure S4

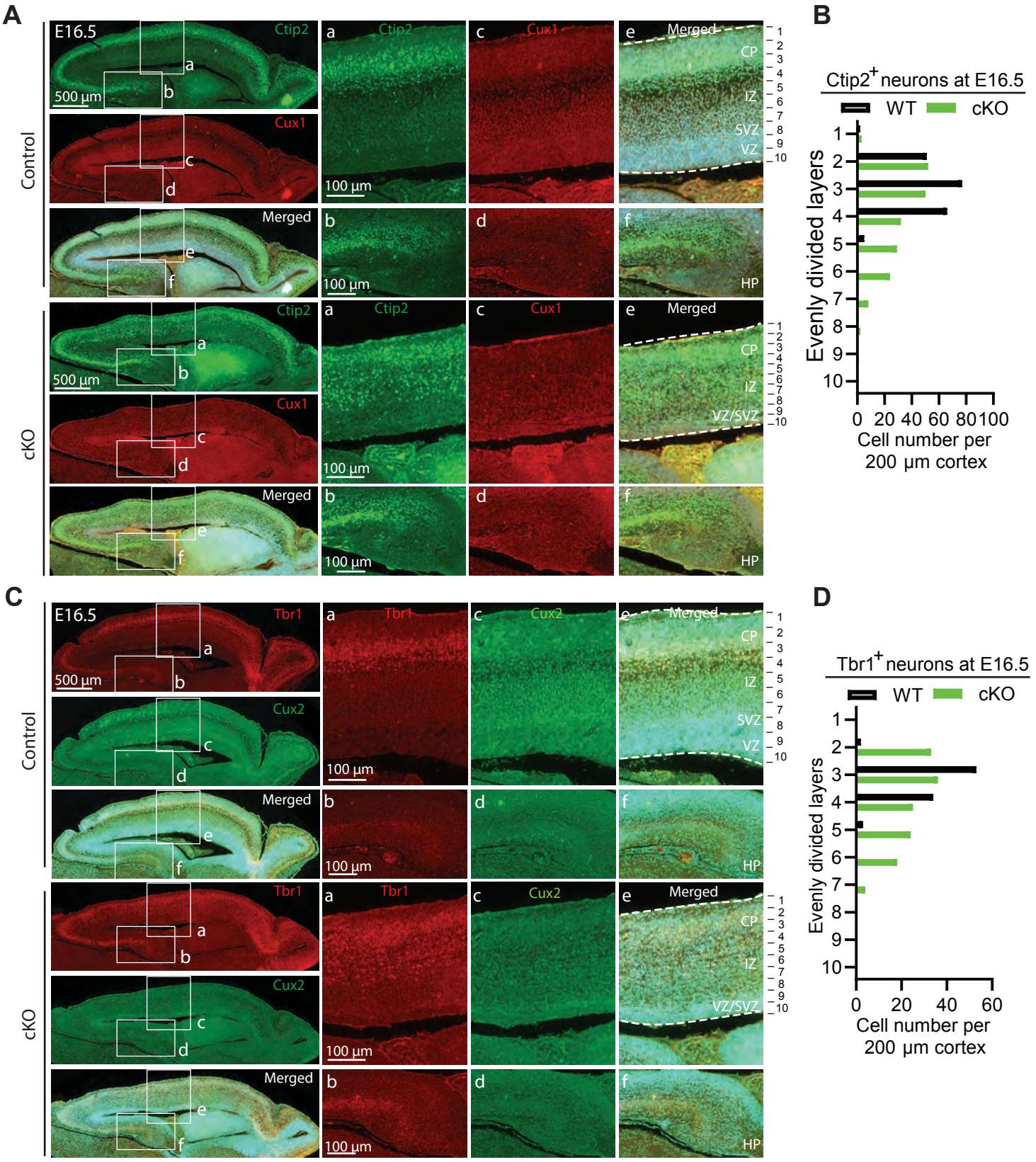
A
E16.5
Ctip2
Cux1
Merged
500 μm
100 μm
Control
cKO
CP
IZ
SVZ
VZ
VZ/SVZ
HP
B
Ctip2+ neurons at E16.5
WT
cKO
Evenly divided layers
Cell number per 200 μm cortex
C
Tbr1
Cux2
D
Tbr1+ neurons at E16.5

Figure S4. Defective neocortical lamination and hippocampal development in the *Hdac3*-deficient brain at E16.5 (related to Figure 2).

(**A**) Co-immunostaining of wild-type and mutant E16.5 brain sections with anti-Cux1 and -Ctip2 antibodies. The former labels SVZ and layers II-IV of adult neocortex (Nieto et al., 2004), whereas the latter marks layers V-VI (Lai et al., 2008). Scale bars, 500 μm for left panels and 100 μm for the rest.

(**B**) The mutant neocortical layers are not clearly separated, so the wild-type or mutant neocortex were equally divided into 10 zones for determination of the $Ctip2^{+}$ cell distribution.

(**C-D**) Co-immunostaining of wild-type and mutant E16.5 brain sections with anti-Tbr1 and -Cux2 antibodies. The former labels layer VI in the adult neocortex (Hevner et al., 2001)) and the latter marks layers II-IV (Nieto et al., 2004). Scale bars, 500 μm for left panels and 100 μm for the rest panels of (C).

Figure S5

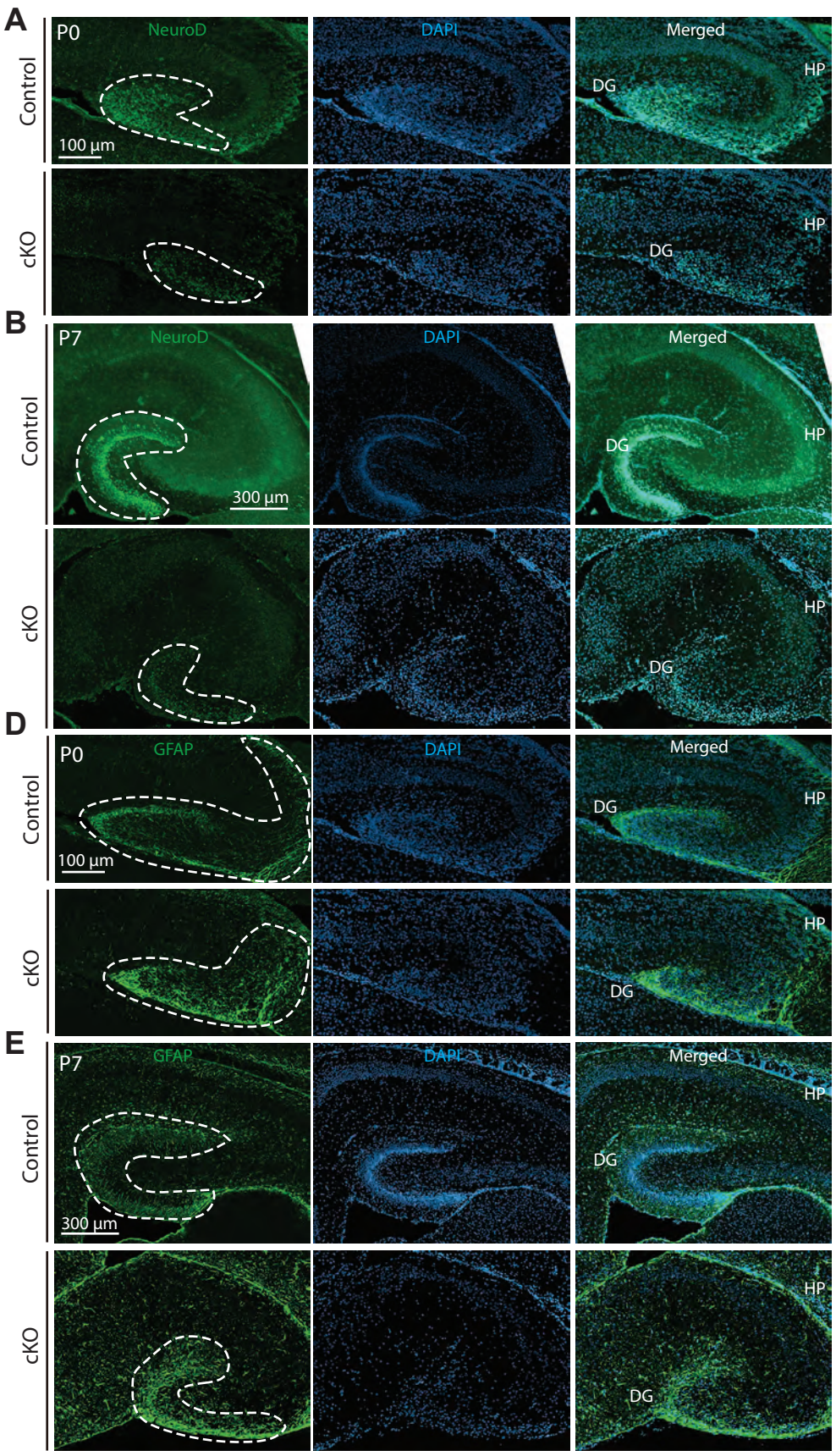
A
P0
NeuroD
DAPI
Merged
Control
cKO
100 µm
DG
HP
B
P7
300 µm
C
NeuroD
Control
cKO
NeuroD+ cell number in dentate gyrus
800
600
400
200
0
P0
P7
D
GFAP
E
F
GFAP
Fluorescence intensity
2.0
1.5
1.0
0.5
0.0

Figure S5. Immunostaining to detect NeuroD and GFAP in wild-type and mutant hippocampi (related to Figure 2).

(**A**) Immunofluorescence microscopic analysis of neonatal brain sections with anti-NeuroD antibody. For the analysis, brain sections were prepared from wild-type and mutant newborns. Only the hippocampal areas are shown here. The images illustrate disorganization of $NeuroD^+$ neuron distribution in the mutant hippocampus and low expression of NeuroD in these neurons.

(**B**) Same as (**A**) except that P7 brain sections were analyzed.

(**C**) Quantification of $NeuroD^+$ neurons in the demarcated areas shown in (A-B).

(**D-E**) Same as (**A-B**) except that anti-GFAP antibody was used.

(**F**) Fluorescence intensity of $GFAP^+$ cells. GFAP is localized to axons and dendrites, which make it difficult to count individual cells, so the overall fluorescence intensity quantified in the areas demarcated with deashed lines, with the wild-type value arbitrarily set to 1.0. The expression of GFAP and NeuroD was minimal in the neocortex.

Abbreviations: DG, dentate gyrus; HP, hippocampus. Scale bars, 100 μm for (A) and (D); 300 μm for (B) and (E).

Figure S6

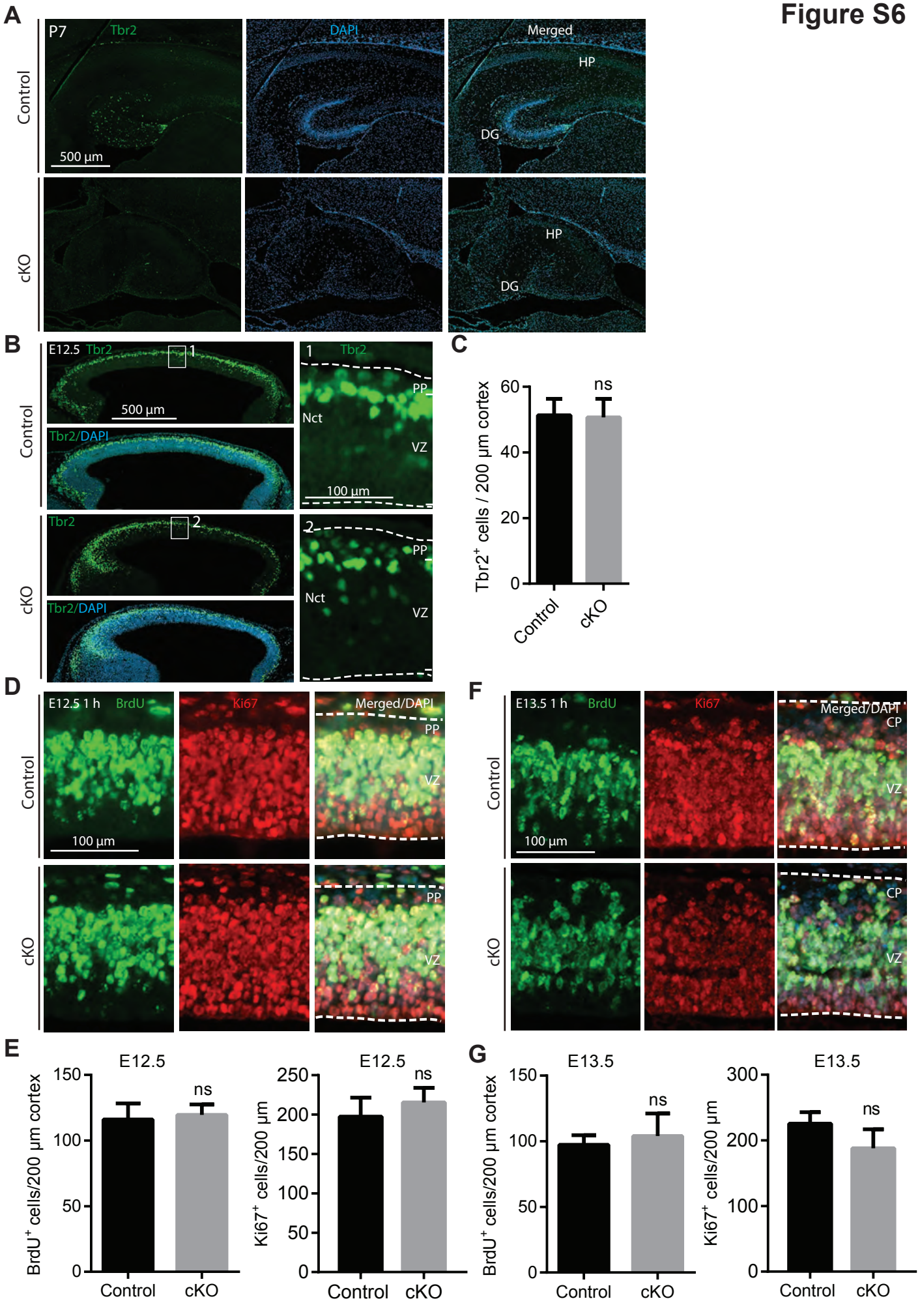
A
P7
Tbr2
DAPI
Merged
HP
DG
500 µm
Control
cKO
B
E12.5 Tbr2
Tbr2/DAPI
500 µm
100 µm
PP
Nct
VZ
C
Tbr2+ cells / 200 µm cortex
ns
Control
cKO
D
E12.5 1 h BrdU
Ki67
Merged/DAPI
F
E13.5 1 h BrdU
CP
E
E12.5
BrdU+ cells/200 µm cortex
Ki67+ cells/200 µm
G
E13.5

Figure S6. Detection of Tbr2$^+$ progenitor cells and normal cell proliferation in the mutant deficient cerebral primordium (related to Figure 4).

(**A**) Immunostaining of brain sections with an anti-Tbr2 antibody. Brain sections were prepared from wild-type and mutant pups at P7. Only the hippocampal areas are shown here. The images illustrate few Tbr2$^+$ progenitors in the mutant hippocampus. Scale bar: 500 μm.

(**B**) Same as (**A**) except that E12.5 embryo sections were analyzed. Only the neocortical (Nct) area is shown. Scale bars, 500 μm for the left panels and 500 μm for the right ones.

(**C**) Quantification of Tbr2$^+$ progenitors. n=3; ns, not statistically significant.

(D) BrdU was injected into pregnant mice at E12.5 for embryo retrieval 1 h later. Embryonic sections were double-stained with anti-BrdU and -Ki67 antibodies. Only an enlarged area of the neocortex is shown in (A) for the wild-type or mutant embryonic section. Scale bar, 100 μm.

(E) Quantification of BrdU$^+$ or Ki67$^+$ cells on embryonic sections prepared as in (D). n=3 for the wild-type or mutant embryo. ns, not statistically significant.

(**F-G**) Same as (**D-E**) except BrdU was injected into pregnant mice at E13.5.

Figure S7

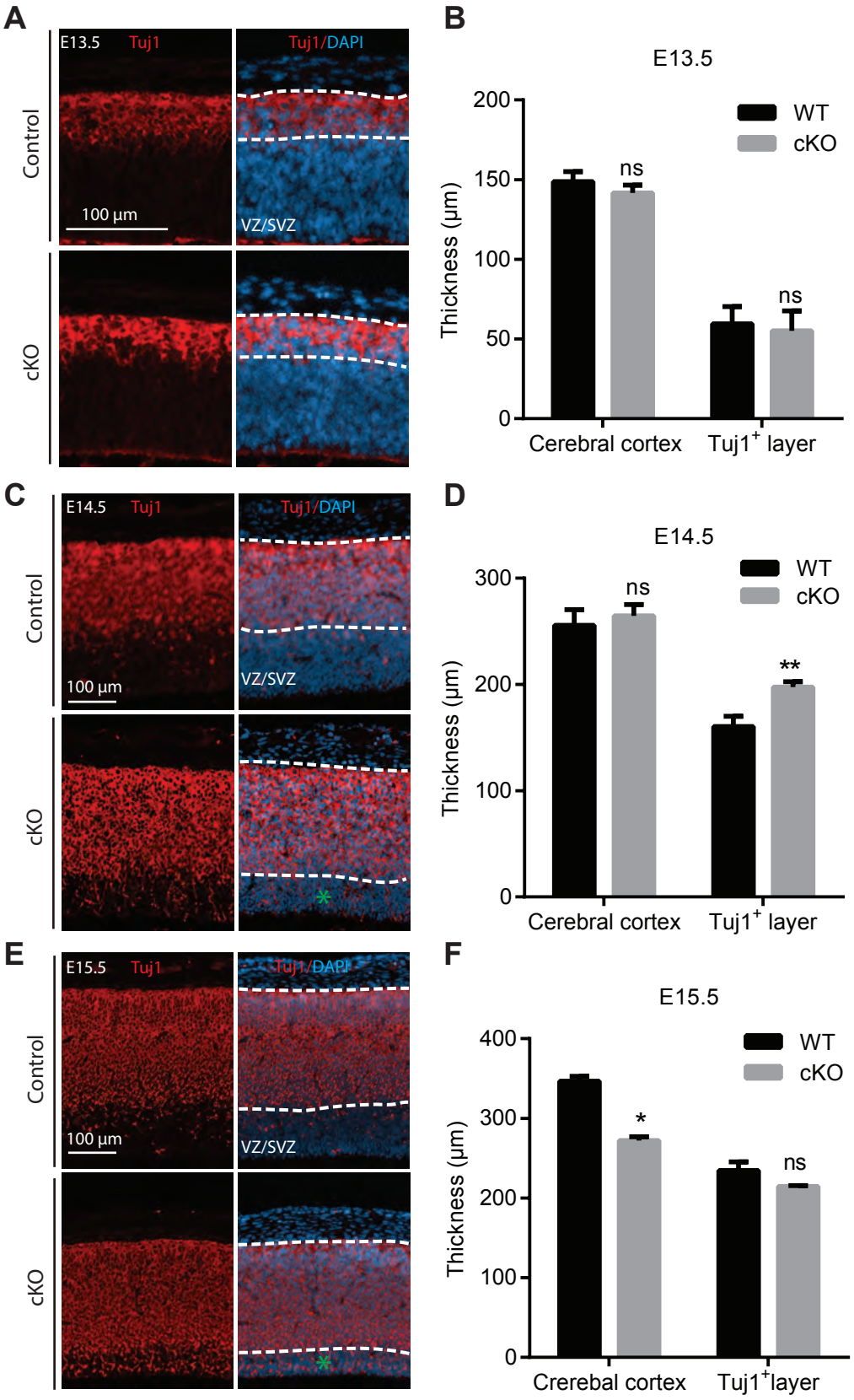
A
E13.5 Tuj1
Tuj1/DAPI
Control
cKO
100 μm
VZ/SVZ
B
E13.5
WT
cKO
ns
ns
Thickness (μm)
200
150
100
50
0
Cerebral cortex
Tuj1+ layer
C
E14.5 Tuj1
Tuj1/DAPI
Control
cKO
100 μm
VZ/SVZ
D
E14.5
WT
cKO
ns
**
Thickness (μm)
300
200
100
0
Cerebral cortex
Tuj1+ layer
E
E15.5 Tuj1
Tuj1/DAPI
Control
cKO
100 μm
VZ/SVZ
F
E15.5
WT
cKO
*
ns
Thickness (μm)
400
300
200
100
0
Crerebal cortex
Tuj1+layer

Figure S7. *Hdac3* deletion triggers premature neurogenesis in the developing neocortex (related to Figure 5).

(**A**) Immunostaining of wild-type and mutant embryo sections with Tuj1 antibody. Embryos were collected at E13.5. Only an enlarged area of the neuroepithelium is shown here for the wild-type or mutant embryonic section. Dashed lines mark borders of the $Tuj1^+$ layer.

(**B**) Quantification of thickness of the entire cortex and the $Tuj1^+$ layer on sections as shown in (**A**). n=3.

(**C-D**) Same as (**A-B**) except that E14.5 embryo sections were analyzed.

(**E-F**) Same as (**A-B**) except that E15.5 embryo sections were analyzed. Green asterisks mark ectopic distribution of $Tuj1^+$ cells and compression of the ventricular/subventricular zone in the mutant at E14.5 and E15.5. n=3.

Scale bars, 100 μm; ns, not statistically significant; *, $p<0.05$; **, $p<0.01$.

Figure S8

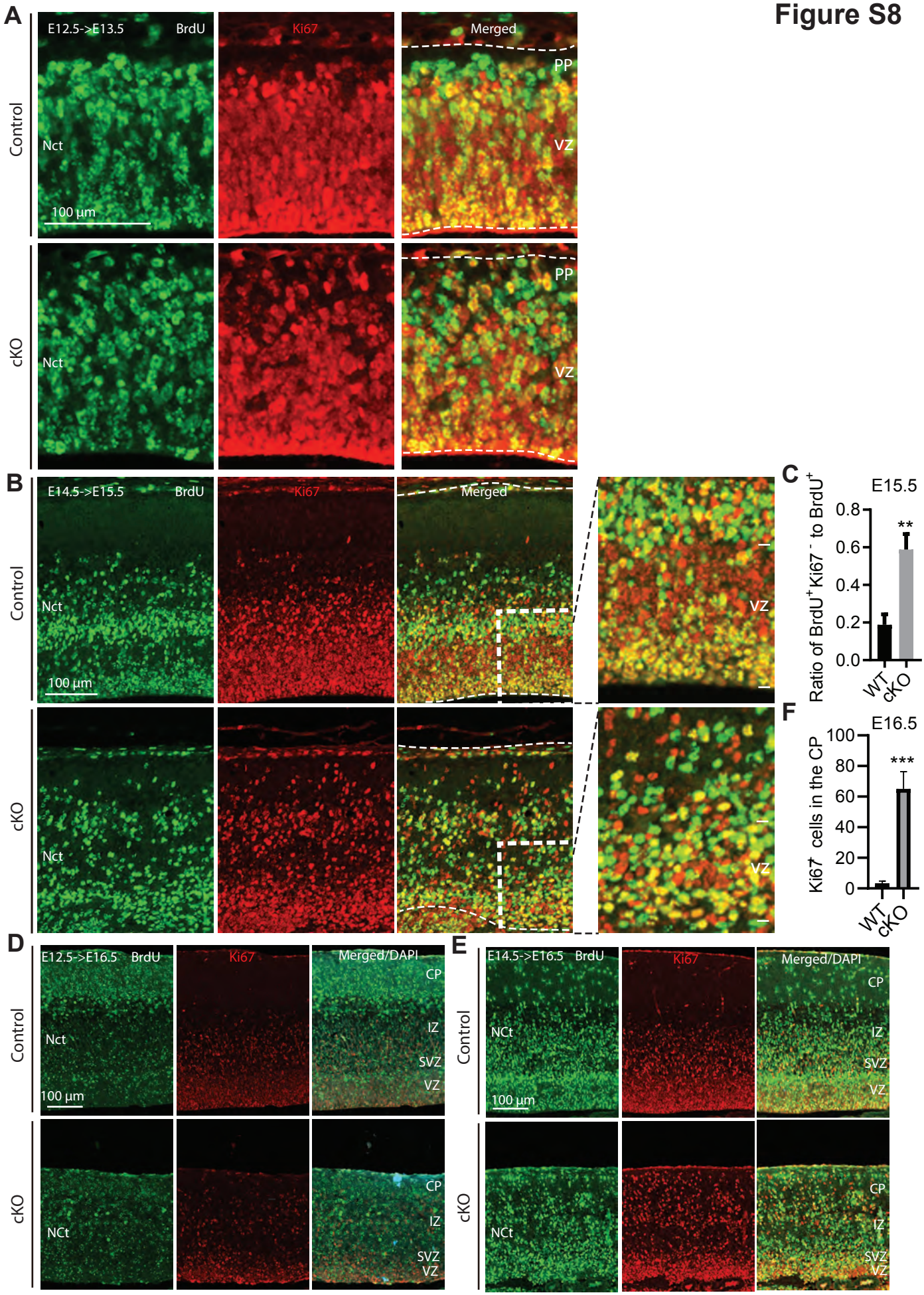
A
E12.5->E13.5
BrdU
Ki67
Merged
Control
Nct
100 µm
PP
VZ
cKO
Nct
PP
VZ
B
E14.5->E15.5
BrdU
Ki67
Merged
Control
Nct
100 µm
VZ
cKO
Nct
VZ
C
E15.5
Ratio of BrdU+Ki67- to BrdU+
0.8
0.6
0.4
0.2
0.0
**
WT
cKO
F
E16.5
Ki67+ cells in the CP
100
80
60
40
20
0
***
WT
cKO
D
E12.5->E16.5
BrdU
Ki67
Merged/DAPI
Control
Nct
100 µm
CP
IZ
SVZ
VZ
cKO
NCt
CP
IZ
SVZ
VZ
E
E14.5->E16.5
BrdU
Ki67
Merged/DAPI
Control
NCt
100 µm
CP
IZ
SVZ
VZ
cKO
NCt
CP
IZ
SVZ
VZ

Figure S8. *Hdac3* deletion alters neuronal migration and induces premature cell cycle exit (related to Figure 5).

(**A**) BrdU was injected into E12.5 pregnant mice for embryo retrieval 24 h later. Embryonic sections were co-stained with anti-BrdU and -Ki67 antibodies. Only an enlarged area of the cerebral cortex is shown here for the wild-type or mutant embryo section. $BrdU^{+}Ki67^{-}$ cells are those that have already exited from the cell cycle.

(**B**) Same as (A) except BrdU was injected at E14.5 pregnant mice.

(**C**) Quantification of the cells in the insets from (B). n=3.

(D-E) BrdU was injected into E12.5 and E14.5 pregnant mice for embryo collection and brain dissection at E16.5. Brain sections were co-stained with anti-BrdU and -Ki67 antibodies. Only an enlarged area of the developing neocortex is shown here for the wild-type or mutant section.

(**F**) Quantification of the $Ki67^{+}$cells in the wild-type or mutant cortical plate (CP) at E16.5. n=3. Scale bar, 100 μm.

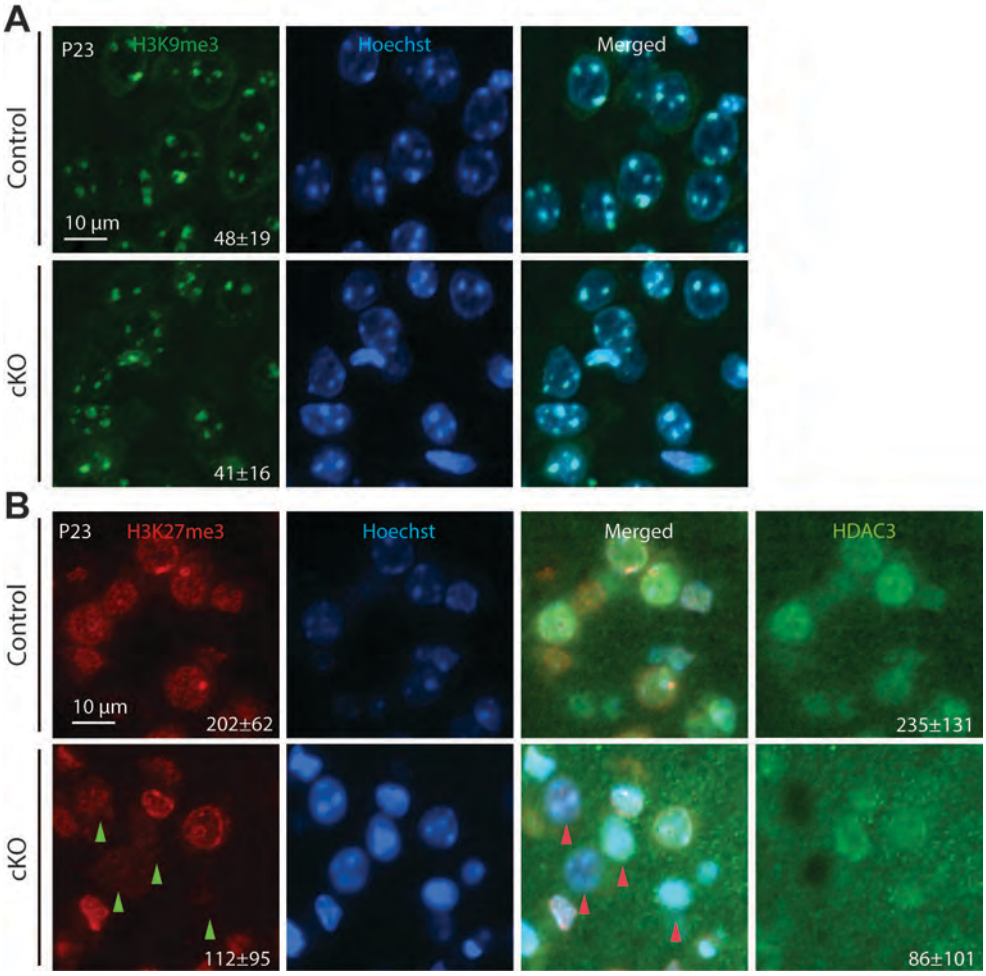

Figure S9. Histone methylation in the mutant cerebral cortex (related to Figure 7).

(**A**) Immunostaining of wild-type and mutant brain sections with anti-H3K9me3 antibody. The sections were prepared from pups at P23. The shown area here was enlarged from the cerebral cortex. The H3K9me3 level was similar between wild-type and mutant cerebral cortices.

(**B**) Same as (**A**) except double immunostaining with anti-HDAC3 and -H3K27me3 antibodies was carried out. The shown area was enlarged from the cerebral cortex. The H3K27me3 level decreased in the mutant cerebral cortex. The fluorescence intensity was measured from 20 cells and the quantification is shown, as mean±s.d., at the bottom-right corners of related images. Green and red arrowheads mark nuclei with weak H3K27me3 signals in the mutant cerebral cortex. Scale bar, 10 µm.

Figure S10

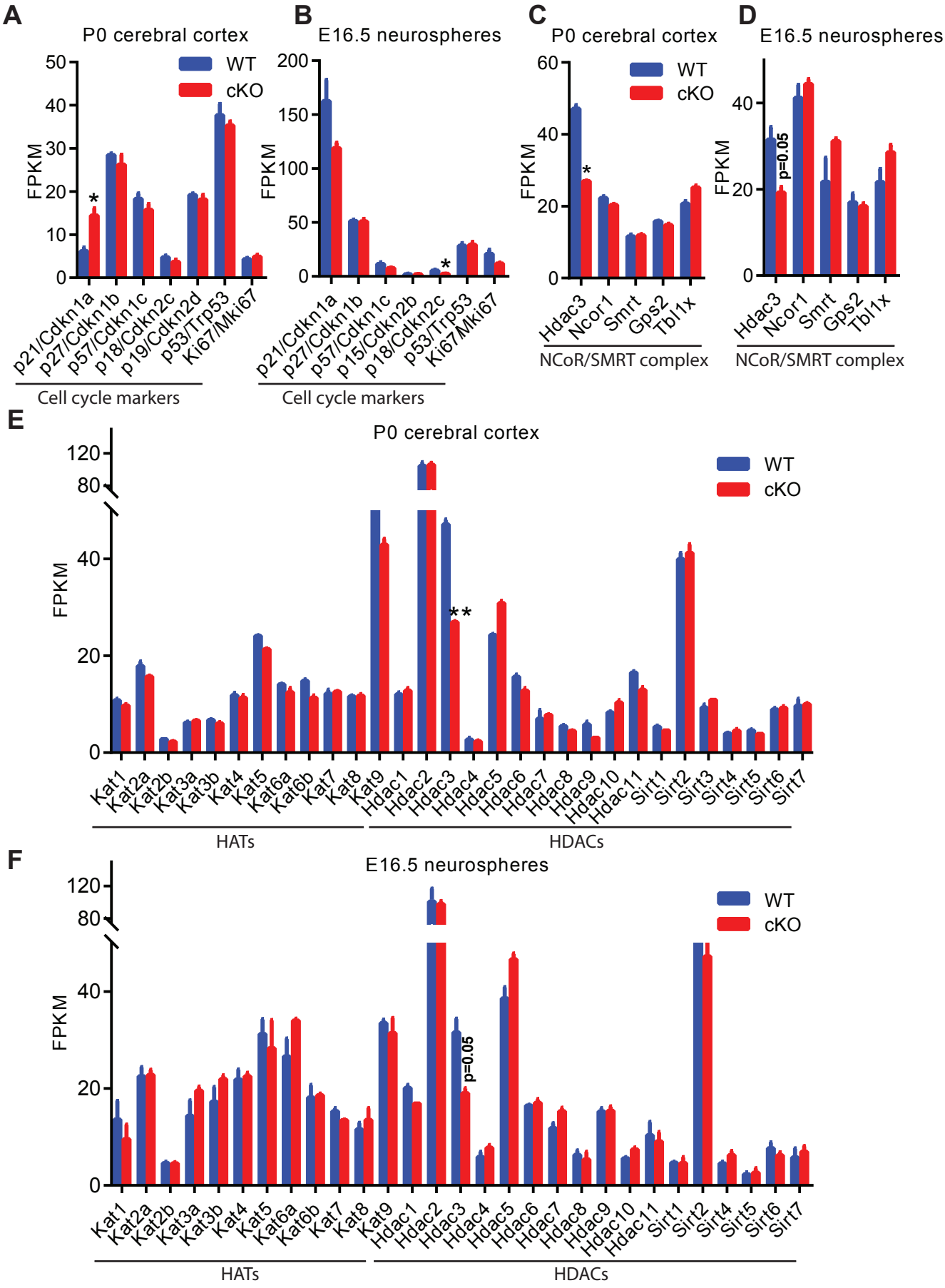
A
P0 cerebral cortex
WT
cKO
FPKM
p21/Cdkn1a
p27/Cdkn1b
p57/Cdkn1c
p18/Cdkn2c
p19/Cdkn2d
p53/Trp53
Ki67/Mki67
Cell cycle markers
B
E16.5 neurospheres
p15/Cdkn2b
C
P0 cerebral cortex
Hdac3
Ncor1
Smrt
Gps2
Tbl1x
NCoR/SMRT complex
D
E16.5 neurospheres
p=0.05
E
P0 cerebral cortex
HATs
HDACs
F
E16.5 neurospheres

Figure S10. Altered transcription of multiple genes in the mutant cerebrum and neurospheres (related to Figure 7).

(**A-B**) FPKM values for cell cycle regulator genes in the wild-type and *Hdac3*-deficient neonatal cerebral cortices and neurospheres.

(**C-D**) FPKM values for *Ncor*, *Smrt*, *Gps2* and *Tbl1x* in the wild-type and *Hdac3*-deficient neonatal cerebral cortices and neurospheres.

(**E-F**) FPKM values for genes encoding different lysine acetyltransferases (KATs) and HDACs in the wild-type and *Hdac3*-deficient neonatal cerebral cortices and neurospheres.

The FPKM values for *Hdac3* transcripts were significantly (in C & E) or almost significantly (in D & F) reduced ($p=0.05$), but the values for the excised two exons in the mutant was much more dramatically reduced in the mutant from RNA-Seq analysis (ref GEO: GSE133195). Moreover, Western blotting (Fig. 1E) and immunostaining using the anti-HDAC3 antibody (Fig. S1A-I) indicated that *Hdac3* is efficiently deleted in the mutant starting at E12.5. The FPKM values are from Tophat analysis of RNA-Seq datasets (see GEO: GSE133195 for the complete tables). Deletion of coding exon 3 introduces a reading frameshift (see Methods), so impact of the deletion at the protein level was much more evident than at the transcript level.

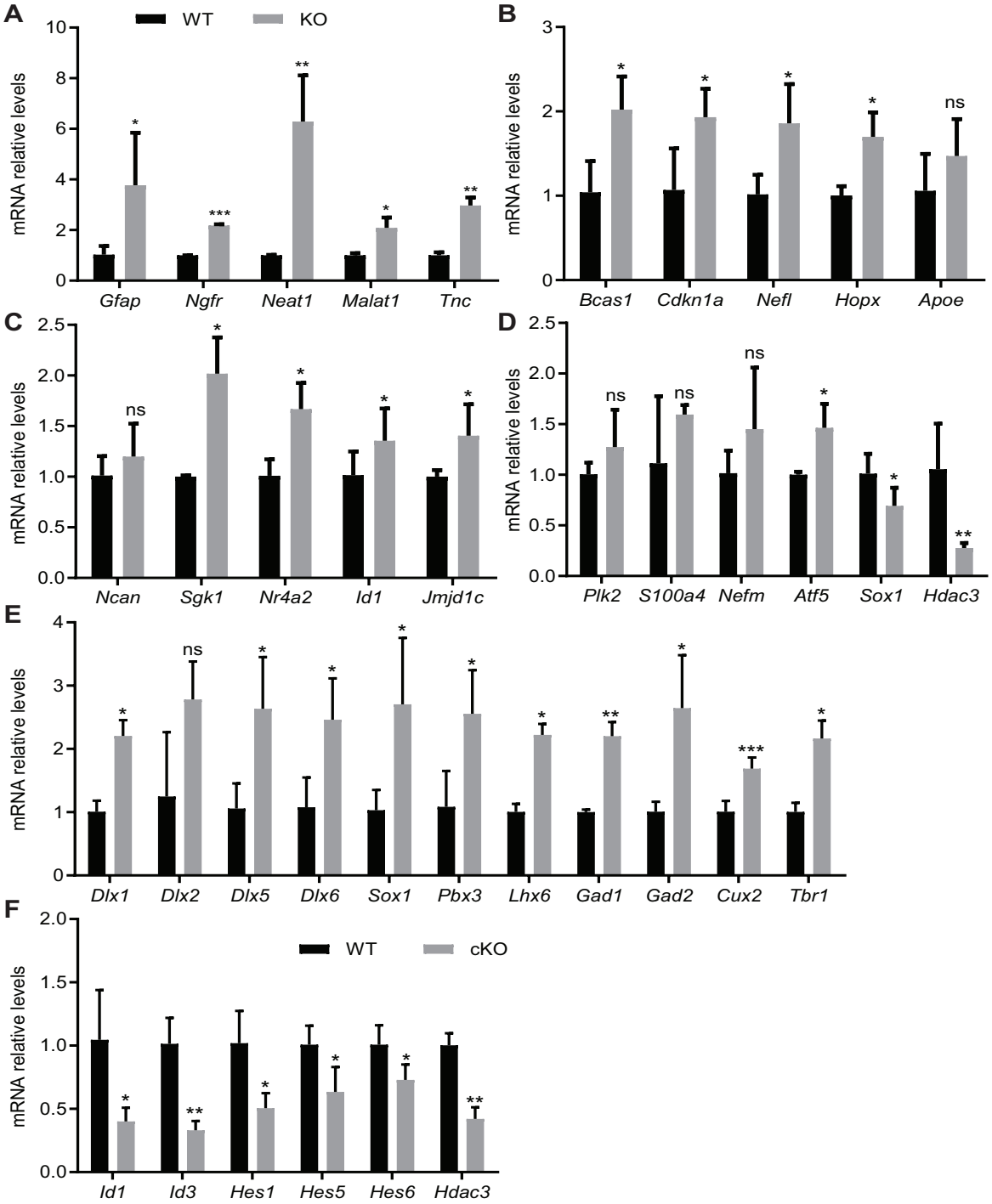

Figure S11. Validation of top differentially expressed genes identified by RNA-Seq of P0 cerebral cortices and E16.5 neurospheres (related to Figure 7).

(**A-D**) RT-qPCR analysis of 19 upregulated genes and one downregulated gene (*Sox1*) in wild-type and mutant neonatal cerebral cortices along with *Hdac3* itself (n=3). *β-Actin* was used as the internal control. For each gene, he transcript level in the wild-type was arbitrarily set to 1.0.

(**E**) RT-qPCR analysis of 11 upregulated genes in wild-type and mutant neurospheres (n=3).

(**F**) Same as (**E**) but 5 downregulated genes were analyzed along with *Hdac3* itself.

ns, not statistically significant; *, $p<0.05$; **, $p<0.01$; ***, $p<0.001$.

Figure S12

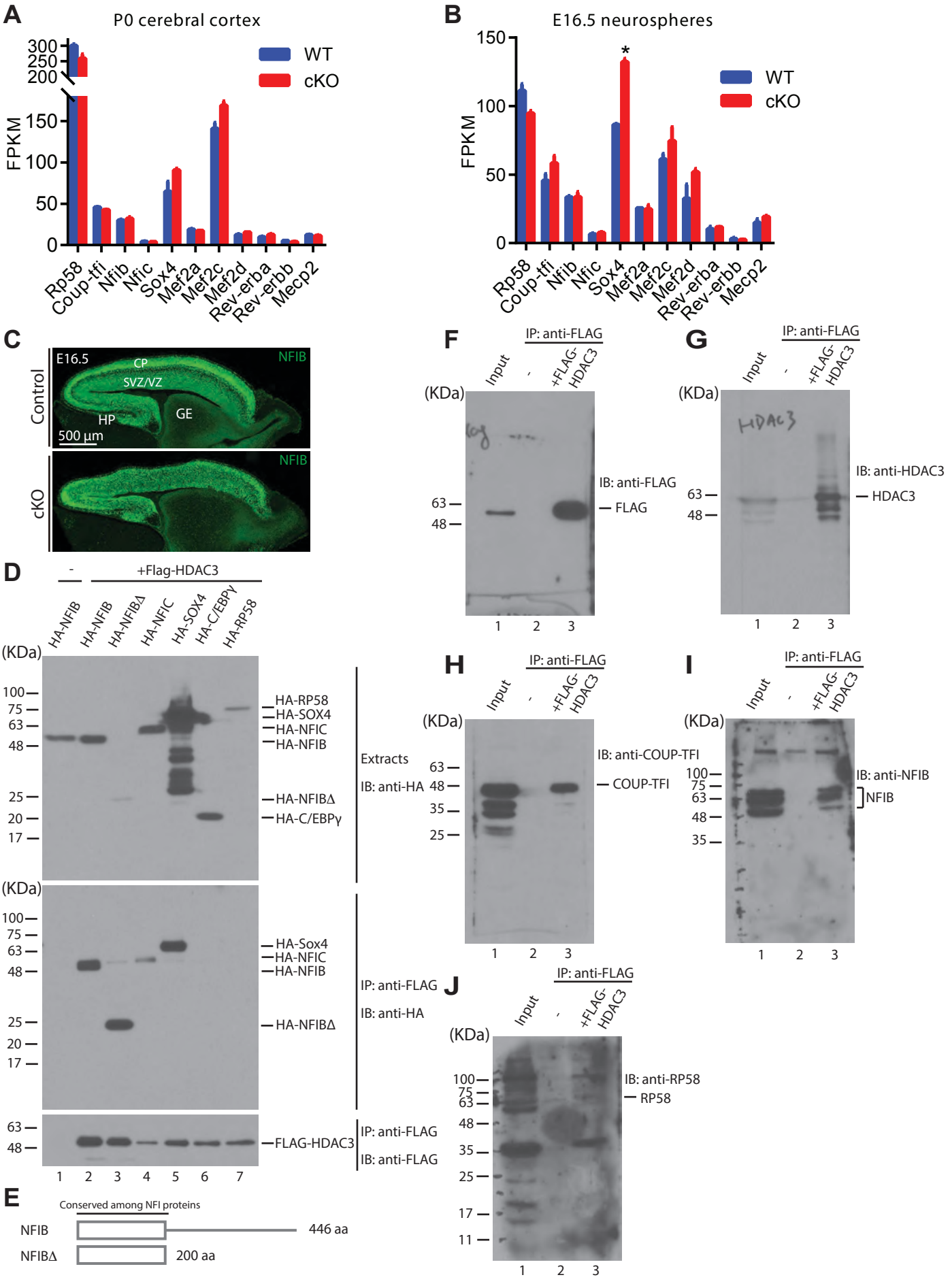
A
P0 cerebral cortex
FPKM
WT
cKO
Rp58
Coup-tfi
Nfib
Nfic
Sox4
Mef2a
Mef2c
Mef2d
Rev-erba
Rev-erbb
Mecp2
B
E16.5 neurospheres
C
E16.5
CP
SVZ/VZ
HP
GE
NFIB
500 µm
Control
cKO
D
-
+Flag-HDAC3
HA-NFIB
HA-NFIBΔ
HA-NFIC
HA-SOX4
HA-C/EBPγ
HA-RP58
(KDa)
HA-Sox4
FLAG-HDAC3
Extracts
IB: anti-HA
IP: anti-FLAG
IB: anti-FLAG
E
Conserved among NFI proteins
NFIB
NFIBΔ
446 aa
200 aa
F
IP: anti-FLAG
Input
+FLAG-HDAC3
IB: anti-FLAG
FLAG
G
IB: anti-HDAC3
HDAC3
H
IB: anti-COUP-TFI
COUP-TFI
I
IB: anti-NFIB
NFIB
J
IB: anti-RP58
RP58

Figure S12. Interaction of HDAC3 with multiple DNA-binding transcription factors highly expressed in the developing brain (related to Figure 7).

(**A-B**) FPKM values of *Rp58*, *Coup-tfi*, *Nfib*, *Nfic*, *Sox4*, *Mef2a*, *Mef2c*, *Mef2d*, *Rev-erba*, *Rev-erbb* and *Mecp2* in wild-type and *Hdac3*-deficient neonatal cerebral cortices or E16.5 neurospheres. The FPKM values are from Tophat analysis of RNA-Seq datasets. Except for *Sox4*, the difference between the wild-type and mutant was not statistically significant. *, $p<0.05$.

(**C**) Immunostaining of E16.5 wild-type and mutant embryonic brain sections with an anti-NFIB antibody. The results indicate that NFIB is highly expressed in the cerebrum at E16.5 and *Hdac3* deletion did not affect NFIB expression, but the distribution was affected. CP, cortical plate; HP, hippocampus; GE, ganglionic eminence; SVZ/VZ, subventricular zone/ventricular zone.

(**D**) Co-immunoprecipitation to assess HDAC3 interaction with NFIB, its N-terminal fragment (NFIBΔ), NFIC2, SOX4, C/EBPγ and RP58. HDAC3 was transiently expressed as a FLAG-tagged fusion protein, while potential partners were expressed as HA-tagged fusion proteins in HEK293 cells. Soluble extracts were prepared for immunoprecipitation (IP) on M2 agarose conjugated with the M2 anti-FLAG monoclonal antibody and after extensive washing, bound proteins were eluted with the FLAG peptide for immunoblotting with anti-FLAG and -HA antibodies as specified. Lane 1 is the negative control, for which HA-tagged NFIB was expressed without FLAG-HDAC3.

(**E**) Schematic illustration of NFIB and its truncation mutant. NFIB has a conserved DNA-binding domain in the N-terminal part (illustrated as a rectangular box). The truncation mutant contains this domain, conserved among different members of the NFI family of transcription factors.

(**F-J**) HDAC3 was transiently expressed as the FLAG fusion protein in HEK293 cells for co-immunoprecipitation with endogenous COUP-TFI, NFIB, and RP58 proteins, detected by their respective antibodies. Lanes 2 were negative controls, for which an empty expression vector was transfected into HEK293 cells.

Table S1 Mendelian ratio for wild-type and *Hdac3*-deficient pups (related to Figure 1)

	Hdac3 f/f	Hdac3 f/+	Hdac3 f/f,Emx1-Cre	Hdac3 f/+,Emx1-Cre	Total	Chi-Test
Total	25	19	17	19	80	ns
Male	11	12	9	9	41	ns
Female	14	7	8	10	39	ns
Expected Ratio	25%	25%	25%	25%	100%	

Note: *Hdac3*$^{f/+}$; *Emx1-Cre* male mice were mated with *Hdac3*$^{f/f}$ females, and pups were genotyped in the first few days after birth. ns, not statistically significant.

Table S2 Genes upregulated by >2.0 fold in mutant neurospheres (related to Figure 7)

Gene Symbol	Base mean	log2(FC)	StdErr	Wald-Stats	*p* value	*p* adjust
Spp1	1908.55	4.52	0.20	22.73	2.39E-114	2.99E-110
Col3a1	984.14	4.28	0.23	18.65	1.32E-77	8.27E-74
Col6a3	776.36	3.74	0.21	17.88	1.81E-71	7.55E-68
Col1a1	451.14	3.28	0.24	13.66	1.65E-42	5.18E-39
Col6a2	313.99	3.23	0.25	12.76	2.88E-37	6.02E-34
Cyp1b1	149.52	2.96	0.28	10.45	1.53E-25	2.14E-22
Col6a1	359.91	2.55	0.25	10.37	3.41E-25	4.27E-22
Col4a1	1423.41	2.25	0.17	12.88	5.70E-38	1.43E-34
Mgp	73.44	2.01	0.28	7.04	1.86E-12	5.18E-10
Tbx18	72.89	1.95	0.28	6.85	7.22E-12	1.96E-09
Col4a2	1481.11	1.87	0.19	9.93	2.93E-23	2.63E-20
Postn	117.75	1.77	0.28	6.22	5.09E-10	1.06E-07
Sned1	166.28	1.76	0.28	6.30	2.95E-10	6.38E-08
Neat1	502.40	1.68	0.23	7.30	2.86E-13	9.88E-11
Nid1	188.45	1.65	0.27	6.16	7.13E-10	1.41E-07
Rasgef1b	759.13	1.63	0.20	7.98	1.51E-15	7.86E-13
Nrk	87.15	1.62	0.29	5.63	1.78E-08	2.69E-06
Anpep	78.83	1.61	0.28	5.69	1.28E-08	1.97E-06
Dcn	210.51	1.53	0.27	5.65	1.56E-08	2.39E-06
Ctsk	96.31	1.45	0.28	5.10	3.47E-07	3.56E-05
Serpinf1	99.58	1.40	0.29	4.87	1.10E-06	9.53E-05
Pdgfrb	174.22	1.39	0.28	4.94	7.95E-07	7.43E-05
Ednra	124.32	1.35	0.28	4.76	1.89E-06	1.53E-04
Enpp1	86.17	1.34	0.29	4.70	2.61E-06	1.99E-04
Col5a1	420.27	1.33	0.23	5.76	8.58E-09	1.38E-06
Pbx3	481.33	1.30	0.22	5.94	2.79E-09	5.07E-07
Dlx2	929.73	1.30	0.18	7.08	1.45E-12	4.31E-10
Nrp2	1875.70	1.30	0.17	7.53	5.13E-14	2.01E-11
A430107O13Rik	88.20	1.26	0.28	4.41	1.04E-05	6.39E-04
Maf	2103.96	1.23	0.15	8.21	2.17E-16	1.30E-13
Dlx6as1	1954.67	1.22	0.18	6.69	2.25E-11	5.64E-09
Dnm3os	40.67	1.20	0.27	4.47	7.89E-06	5.15E-04
Adamts12	166.33	1.20	0.27	4.37	1.25E-05	7.31E-04
Mmp9	63.33	1.20	0.28	4.24	2.25E-05	1.20E-03
Mmp2	116.25	1.19	0.29	4.17	3.06E-05	1.52E-03
Zfhx4	470.46	1.19	0.26	4.64	3.53E-06	2.55E-04
Penk	312.76	1.19	0.26	4.50	6.70E-06	4.51E-04
Gm14204	377.05	1.18	0.23	5.07	3.93E-07	3.94E-05
Cp	169.35	1.18	0.28	4.21	2.60E-05	1.36E-03
Gad2	1829.42	1.17	0.16	7.51	6.06E-14	2.30E-11
Thbs1	460.37	1.16	0.22	5.18	2.26E-07	2.42E-05

Dlx1	1917.91	1.14	0.15	7.44	9.82E-14	3.52E-11
Sp9	342.75	1.14	0.25	4.59	4.43E-06	3.08E-04
Adarb2	738.05	1.14	0.24	4.74	2.18E-06	1.74E-04
Gad1	6301.49	1.14	0.13	8.98	2.81E-19	2.07E-16
Tox2	875.68	1.13	0.18	6.17	7.01E-10	1.41E-07
Col5a2	426.57	1.13	0.25	4.57	4.95E-06	3.42E-04
Sez6	7104.16	1.13	0.15	7.68	1.55E-14	6.93E-12
Dlx1as	2060.80	1.12	0.16	7.12	1.07E-12	3.36E-10
Lhx6	3068.50	1.12	0.14	7.96	1.76E-15	8.83E-13
Grik1	650.11	1.12	0.21	5.46	4.74E-08	6.53E-06
Gm5607	264.20	1.11	0.27	4.19	2.74E-05	1.41E-03
Sorl1	855.54	1.11	0.19	5.85	4.87E-09	8.02E-07
Bend4	591.16	1.10	0.20	5.40	6.66E-08	8.43E-06
Lama4	126.63	1.10	0.29	3.84	1.21E-04	4.77E-03
Agtr2	47.29	1.09	0.27	4.11	4.01E-05	1.89E-03
Sox1	764.80	1.08	0.20	5.48	4.19E-08	5.84E-06
Gsn	270.71	1.07	0.25	4.28	1.86E-05	1.01E-03
Col11a2	549.73	1.07	0.22	4.89	1.02E-06	8.86E-05
Plxna2	10911.13	1.06	0.14	7.48	7.17E-14	2.64E-11
Slc32a1	825.49	1.04	0.19	5.54	3.07E-08	4.37E-06
Dlx5	566.83	1.03	0.21	4.95	7.45E-07	7.07E-05
Dlx6	129.03	1.02	0.28	3.64	2.70E-04	8.87E-03
BC057022	202.44	1.02	0.27	3.76	1.73E-04	6.40E-03
Ephb1	650.56	1.01	0.20	5.07	4.02E-07	3.99E-05
Zfp804a	944.22	1.01	0.19	5.23	1.74E-07	1.93E-05
Nid2	313.04	1.00	0.26	3.88	1.03E-04	4.19E-03
Acan	324.19	1.00	0.25	3.92	8.93E-05	3.74E-03

Note: 68 genes are listed here. Filtered sequence reads from the neurosphere RNA-Seq datasets were mapped to the mouse reference genome (mm9) via STAR, and mapped reads were counted with FeatureCounts for subsequent differential analysis with DESeq2. Visit Gene Expression Omnibus (GSE133195) for the whole table. Abbreviations: FC, fold of change; StdErr, standard error; *p* adjusted, adjusted *p* value.

Table S3 Genes downregulated by <0.5 fold in mutant neurospheres (related to Figure 7)

Gene Symbol	Base mean	log2(FC)	StdErr	Wald-Stats	*p* value	*p* adjust
Slc16a3	134.44	-2.95	0.29	-10.33	5.29E-25	6.02E-22
Mt2	541.36	-2.41	0.23	-10.52	6.90E-26	1.08E-22
Dio2	485.96	-2.00	0.23	-8.59	8.36E-18	5.24E-15
Mt1	785.96	-1.96	0.24	-8.00	1.23E-15	6.68E-13
Bnip3	403.77	-1.76	0.23	-7.61	2.76E-14	1.15E-11
Dgkk	384.34	-1.72	0.24	-7.13	9.82E-13	3.15E-10
Slc2a1	759.68	-1.71	0.20	-8.72	2.87E-18	1.91E-15
Hmox1	1464.35	-1.62	0.18	-9.24	2.42E-20	1.90E-17
Cav1	408.40	-1.61	0.24	-6.59	4.44E-11	1.07E-08
Egln3	252.83	-1.61	0.25	-6.36	2.04E-10	4.66E-08
P4ha2	148.60	-1.54	0.28	-5.51	3.55E-08	5.00E-06
Ndufa4l2	54.04	-1.50	0.28	-5.42	6.09E-08	7.86E-06
Ramp1	229.70	-1.48	0.27	-5.59	2.26E-08	3.37E-06
Gpi1	12193.74	-1.48	0.12	-12.24	1.96E-34	3.50E-31
Ldha	4733.31	-1.46	0.14	-10.19	2.17E-24	2.27E-21
Fbln2	2214.92	-1.44	0.17	-8.72	2.90E-18	1.91E-15
Ldb2	825.97	-1.43	0.19	-7.60	2.91E-14	1.18E-11
Pdk1	709.26	-1.43	0.20	-7.30	2.92E-13	9.88E-11
Grin2c	212.73	-1.42	0.27	-5.30	1.19E-07	1.36E-05
Lipg	89.78	-1.38	0.29	-4.81	1.54E-06	1.28E-04
Ero1l	1547.51	-1.38	0.18	-7.74	1.01E-14	4.70E-12
F2rl2	148.73	-1.35	0.28	-4.89	9.99E-07	8.86E-05
Sparcl1	3544.49	-1.35	0.14	-9.47	2.87E-21	2.40E-18
Usp43	187.36	-1.35	0.28	-4.79	1.66E-06	1.37E-04
Car9	44.87	-1.33	0.27	-4.95	7.50E-07	7.07E-05
Rgs6	93.60	-1.32	0.29	-4.61	3.99E-06	2.81E-04
Pgm2	695.03	-1.31	0.20	-6.58	4.68E-11	1.11E-08
Fam162a	323.31	-1.31	0.25	-5.22	1.81E-07	1.98E-05
Slc38a3	818.09	-1.29	0.19	-6.85	7.36E-12	1.96E-09
Ptpru	361.51	-1.29	0.24	-5.41	6.30E-08	8.06E-06
Ccbe1	353.89	-1.29	0.24	-5.42	5.83E-08	7.69E-06
Hk2	348.52	-1.28	0.25	-5.22	1.78E-07	1.95E-05
Phospho1	82.95	-1.26	0.29	-4.37	1.23E-05	7.28E-04
Id1	158.08	-1.24	0.28	-4.38	1.16E-05	6.95E-04
Ephx1	1105.46	-1.23	0.22	-5.58	2.40E-08	3.50E-06
Pcdh20	221.41	-1.23	0.26	-4.68	2.88E-06	2.11E-04
Sidt1	65.68	-1.23	0.28	-4.31	1.60E-05	9.00E-04
Necab1	1027.45	-1.22	0.20	-6.25	4.20E-10	8.91E-08
Slc1a3	11585.24	-1.21	0.12	-9.99	1.77E-23	1.70E-20
P4ha1	774.59	-1.20	0.20	-5.94	2.90E-09	5.19E-07
Mfge8	2807.72	-1.19	0.17	-7.04	1.86E-12	5.18E-10

Bhlhe40	730.28	-1.16	0.20	-5.69	1.24E-08	1.94E-06
3110035E14Rik	323.14	-1.16	0.26	-4.47	7.70E-06	5.08E-04
Tpi1	2839.71	-1.15	0.16	-7.15	8.86E-13	2.92E-10
Lrfn5	368.26	-1.15	0.23	-5.01	5.49E-07	5.34E-05
Ndrg1	1483.54	-1.15	0.19	-6.16	7.29E-10	1.41E-07
Cpne7	534.90	-1.15	0.24	-4.82	1.46E-06	1.23E-04
Rspo2	117.33	-1.15	0.29	-4.00	6.38E-05	2.83E-03
Id3	330.19	-1.14	0.24	-4.77	1.80E-06	1.47E-04
Nusap1	432.02	-1.14	0.23	-4.93	8.17E-07	7.59E-05
Rasl11a	170.87	-1.13	0.27	-4.16	3.20E-05	1.57E-03
Slc16a1	373.95	-1.13	0.26	-4.29	1.78E-05	9.82E-04
Ntsr1	730.48	-1.13	0.19	-5.86	4.63E-09	7.74E-07
Ppp1r3c	436.79	-1.12	0.23	-4.84	1.31E-06	1.12E-04
Galk1	186.51	-1.10	0.27	-4.12	3.79E-05	1.81E-03
Aox1	130.83	-1.10	0.28	-3.93	8.35E-05	3.55E-03
Ass1	302.07	-1.10	0.25	-4.38	1.17E-05	6.97E-04
Igfbp2	4075.91	-1.09	0.14	-8.02	1.03E-15	5.85E-13
Inhbb	241.51	-1.09	0.25	-4.29	1.82E-05	9.98E-04
Emp2	392.03	-1.08	0.24	-4.47	7.83E-06	5.13E-04
Rlbp1	688.12	-1.08	0.20	-5.35	8.96E-08	1.09E-05
Ctsc	548.99	-1.07	0.24	-4.55	5.39E-06	3.69E-04
Tubb6	659.82	-1.06	0.23	-4.63	3.73E-06	2.67E-04
Thy1	1720.43	-1.06	0.16	-6.60	3.99E-11	9.80E-09
Abi3	67.34	-1.05	0.28	-3.71	2.11E-04	7.39E-03
Cth	94.19	-1.04	0.29	-3.61	3.10E-04	9.87E-03
Vegfa	5178.04	-1.03	0.14	-7.65	2.03E-14	8.78E-12
E130114P18Rik	186.44	-1.03	0.27	-3.86	1.12E-04	4.47E-03
Klf10	876.79	-1.03	0.20	-5.26	1.41E-07	1.60E-05
Grm2	403.03	-1.02	0.23	-4.50	6.72E-06	4.51E-04
Eya1	182.41	-1.01	0.28	-3.64	2.68E-04	8.87E-03
Kbtbd11	639.87	-1.01	0.21	-4.78	1.78E-06	1.46E-04
Pgk1	2463.05	-1.01	0.15	-6.83	8.40E-12	2.19E-09
Ccnd2	9091.65	-1.01	0.13	-7.76	8.55E-15	4.12E-12
Slc24a4	67.94	-1.00	0.28	-3.56	3.65E-04	1.12E-02

Note: 68 genes are listed here. Filtered sequence reads from the neurosphere RNA-Seq datasets were mapped to the mouse reference genome (mm9) via STAR, and mapped reads were counted with FeatureCounts for subsequent differential analysis with DESeq2. Refer GSE133195 for the whole table. Abbreviations: FC, fold of change; StdErr, standard error; *p* adjust, adjusted *p* value.

TRANSPARENT METHODS

Animal study approval. Mouse-related procedures were performed according to the Animal Use Protocol 5786, which was reviewed and approved by the Facility Animal Care Committee of McGill University, Montreal, Quebec, Canada.

Mice. *Hdac3*$^{f/f}$ mice were derived from the EMMA mouse repository (No. 05711; *Hdac3*<tm1a(EUCOMM)Wtsi>/WtsiBiat). The original *Hdac3* allele from the depository contains a LacZ cassette flanked with two FRT sites. This cassette was first removed through crossing *with Pgk1-FLPo* mice (The Jackson Laboratory, Cat. No. 011065) to obtain the heterozygous *Hdac3*$^{f/+}$ mice. This *Hdac3*^{f} allele contains two LoxP sites flanking the third coding exon (Chr18:37,952,470-379,952,613; GRCm38/mm10, https://genome.ucsc.edu/) of *Hdac3*. Removal of this 134-bp exon by Cre-mediated recombination triggers a reading frameshift and subsequent inactivation of the entire allele. Intercross between heterozygous *Hdac3*$^{f/+}$ mice generated *Hdac3*$^{f/f}$ homozygotes, which were then mated with *Emx1-Cre* mice (The Jackson Laboratory, Cat. No. 005628). Crossing of the resulting *Hdac3*$^{f/+}$;*Emx1-Cre* mice with *Hdac3*$^{f/f}$ homozygotes generated *Hdac3*$^{f/+}$;*Emx1-Cre* and *Hdac3*$^{f/f}$;*Emx1-Cre* embryos or pups. All mice were in the C57BL/6 genetic background.

Open field tests. The tests were carried out as previously described (Li et al., 2019).

Histological analysis. Preparation of brain and embryonic sections for Nissl staining and other histological analysis were performed as described (Kim et al., 2013; You et al., 2015a; You et al., 2015b). Slides were digitized with an Aperio Slide Scanner (Leica Systems) for further viewing or quantification.

BrdU tracing *in vivo*. BrdU labeling was carried out as described (Li et al., 2019; You et al., 2015a; You et al., 2015b). It was injected intraperitoneally into pregnant mice with a dosage of 50 mg per 1 kg body weight. The mice were sacrificed at different timepoints according to experimental goals. For S-phase analysis, mice were sacrificed 1 h after injection. For analysis of the cell-cycle exit, the waiting time after injection was 24 h, and for neuronal migration, the post-injection wait time was from 48 to 96 h.

Immunostaining. Antigen retrieval was carried out by boiling paraffin-section slides in the citrate buffer (10 mM sodium citric acid, 0.05% Tween 20, pH 6.0) for 20 min as described (Kim et al., 2013; You et al., 2015a; You et al., 2015b). For BrdU detection, the sections were incubated in 2N HCl for 30-60 min. Nuclei were counterstained with DAPI or Hoechst 33342. The following antibodies were used: rabbit anti-HDAC3 (Abcam, ab7030, 1:2500), goat anti-Sox2 (R&D systems, AF2018, 1:200), rabbit anti-Tbr2 (Abcam, ab23345, 1:400), rabbit anti-Cux1 (1:200) (Sansregret et al., 2011), rat anti-Ctip2 (Abcam, ab18465, 1:400), rabbit anti-Cux2 (1:200) (Gingras et al., 2005), rabbit anti-Tbr1 (Santa Cruz, sc-376258, 1:100), mouse Tuj1 (Covance, MMS-435p, 1:1000), rat anti-BrdU (Abcam, ab6326, 1:400), mouse anti-Ki67 (BD Pharmingen, 550609, 1:200), rabbit anti-gamma H2A.X (Abcam, ab2893, 1:500), rabbit anti-H3K9me3 (EMD Millipore, 07-442, 1:500), mouse anti-H3K27me3 (Abcam, ab6002, 1:500), goat anti-NeuroD (Santa Cruz, sc1084, 1:100), rabbit anti-GFAP (Dako, Z0334, 1:2000), Alexa Fluor 488-conjugated goat-anti-rabbit IgG (Invitrogen, A-11008, 1:500), Alexa Fluor 488-conjugated donkey-anti-goat IgG (Invitrogen, A-11055, 1:500), Alexa Fluor 568-conjugated goat-anti-rabbit

IgG (Invitrogen, A-11011, 1:500), Alexa Fluor 488-conjugated goat-anti-rat IgG (Invitrogen, A-11006, 1:500) and Alexa Fluor 568-conjugated goat-anti-mouse IgG (Invitrogen, A-11004, 1:500) antibodies. For quantification of fluorescence intensity, images were analyzed by Image J (e.g. Figs S1 and S9), whereas cell numbers were counted manually.

Immunoblotting. On ice, mouse tissues or neurospheres were suspended in the cold RIPA buffer (150 mM NaCl, 1.0% Nonidet P-40 (or Triton X-100), 0.5% sodium deoxycholate, 0.1% SDS, 50 mM Tris-HCl, pH 8.0) containing a proteinase inhibitor cocktail, composed of 1 mM phenylmethylsulfonyl fluoride, 1 μg/ml pepstatin, 2 μg/ml aprotinin and 0.5 μg/ml leupeptin. After brief sonication (for 15 seconds at setting 5 with a VirSonic 100 sonicator) on ice, the suspension was centrifugated for 10 min in an Eppendorf centrifuge at 20,000 *g* and 4°C. The supernatant was transferred to a new tube on ice. The protein concentration was determined by a Bradford protein assay kit (Sigma). Protein extracts were mixed with a 3xRSB buffer (240 mM Tris-HCl pH 6.8, 6% SDS, 30% glycerol, 16% β-mercaptoethanol, 0.06% bromophenol blue) and boiled for SDS-PAGE on 10-15% acrymide gels and subsequent transfer onto a Nitrocellulose membrane (Pall Corp., P/N66485). The membrane was incubated with the blocking buffer [TBS-T (0.1% Tween 20 in TBS) containing 5% nonfat milk powder] for 30 min at room temperature on a rocking platform and then incubated with the same buffer containing a primary antibody overnight at 4 °C on a rocking platform. After washing with TBS-T for 4 times (10 min each, with agitation), the membrane was incubated, on a rocking platform, with the blocking buffer containing the horse radish peroxidase-conjugated secondary antibodies at room temperature for 1 h. The membrane was washed above and developed with the enhanced chemiluminescence substrates (FroggaBio, 16024). The following antibodies were used: rabbit anti-HDAC3 (Abcam, ab7030, 1:10,000), rabbit anti-H3 (Abcam, ab1791, 1:100,000), rabbit anti-H3K4ac (EMD Millipore, 07-539, 1:2000), rabbit anti-H3K9ac (Abcam, ab4441, 1:2000), rabbit anti-H3K14ac (Abcam, ab52946, 1:1000), rabbit anti-H3K18ac (Abcam, ab1191, 1:10,000), rabbit anti-H3K23ac (EMD Millipore, 07-355, 1:20,000), rabbit anti-H3K27ac (EMD Millipore, 07-360, 1:1000), rabbit anti-H4 (Abcam, ab18253, 1:10,000), rabbit anti-H4K16ac (Abcam, ab109463, 1:1500), rabbit anti-H4ac (EMD Millipore, 06-866, 1:2000), rabbit anti-H3K14pr (PTM Biolabs, PTM-211, 1:1000), mouse anti-H3K23pr (PTM-208, 1:1000), mouse anti-H3K23cr (PTM-519, 1:2500), rabbit anti-H3K4me3 (EMD Millipore, 07-473, 1:5000), rabbit anti-H3K9me3 (EMD Millipore, 07-442, 1:500), mouse anti-H3K27me3 (Abcam, ab6002, 1:2000), rabbit anti-NFIB/B2 (Abcam, ab186738, 1:2000), rabbit anti-ZNF238/RP58 (Abcam, ab118471, 1:500), and rabbit anti-COUP-TFI (Abcam, ab181137, 1:1000) antibodies. For quantification, immunoblots in Figs 1E, 6J and 7A-B were analyzed via Image J.

Neurosphere formation assays. The procedures were carried out in the tissue-culture hood unless indicated otherwise. All the surgical instruments and solutions used were sterilized. Briefly, the pregnant mice at E16.5 or E18.5 were euthanized and embryos were dissected out and put in PBS. Heads was collected, washed in PBS and kept in PBS/2% glucose on ice for subsequent manipulation. Under a bench dissecting microscope, the head skin was removed and the skull was opened with a pair of surgical scissors. The brain was dissected out using a fine pair of forceps in cold PBS/2% glucose solution. The cerebral cortices were segregated from the rest of the brain with the forceps under the dissecting microscope and collected into an Eppendorf tube containing 1 ml of the neurosphere complete culturing medium (NeuroCult NSC Basal Medium, StemCell Technologies, #05700) supplemented with 10% NeuroCult Proliferation Supplement (StemCell

Technologies, #05701) and 20 ng/ml rhEGF (StemCell Technologies, #78006.1) on ice. The tube was transferred into the hood for pipetting up and down gently for 8 times with a 1 ml Pipetman tip to prepare single cell suspension, with the Pipetman set at 0.8 ml. Air bubbles was minimized during pipetting as excessive oxygen from the bubbles was deleterious for subsequent NSC growth. After pipetting, the tube was kept still at room temperature for 1 min and the supernatant was transferred to a new tube for centrifugation in a bench-top centrifuge for 5 min at 150 *g*. The supernatant was discarded, and the pellet was gently mixed with 1 ml of the fresh neurosphere complete culture medium. The suspension was filtered through a sterile 40-μm nylon cell strainer (Fisher Scientific, #22363547) and the resulting filtrate was considered as the single-cell preparation. After counting, wild-type and mutant cells were seeded into wells of a 6-well plate at the same number.

For treatment with the HDAC3 inhibitor RGFP966 (SelleckChem, S7229), different concentrations were used (0, 0.08 or 0.8 μM). At different timepoints, the size, number and cell amount of neurospheres were measured. For size measurement, images were randomly taken under a macroscope. For counting neurospheres, a small aliquot of cultured neurospheres was diluted in a 96-well plate and the neurosphere number was counted under a regular light microscope. For determination of the total cell number, an aliquot of neurospheres was taken and pipetted up and down to prepare single cell suspension for counting. For RNA-Seq, fresh neurospheres were washed once with PBS for subsequent RNA preparation. For immunoblotting, neurospheres were washed once with PBS for extract preparation in the RIPA buffer as described above.

For immunostaining, cultured neurospheres were collected into a 15 ml tube and kept for 10 min in a hood. The supernatant was aspirated and 4% PFA was added for incubation at room temperature for 10 min. After fixation, the upper supernatant was removed and neurospheres were washed trice in PBS (to preserve neurosphere morphology, all separation steps were carried out by standing still in the hood for 10 min, instead of centrifugation). Cells in neurospheres were permeabilized in 0.2% Triton-X for 10 min and blocked in 5% BSA for 30 min, followed by incubation with a primary antibody for 30-60 min, extensive washing and subsequent incubation in the blocking buffer with the respective fluorophore-conjugated secondary antibody for 60 min. Neurospheres were then transferred to a 6- or 12-well plate for examination under a fluorescence microscope.

RNA isolation, RNA-Seq and bioinformatic analysis. Total RNA was isolated from wild-type and mutant neonatal cerebral cortices, or wild-type and mutant neurospheres cultured for 4 days from E16.5 embryonic cerebral cortices. The RNA quality and quantity were assessed on an RNA Tapestation (Agilent). All RNA samples with a SIN score higher than 8 were used for subsequent RNA-Seq at Omega Bio-tek (Norcross, GA, USA). Specifically, reverse transcription was carried out with oligo-dT primers and cDNA was then fragmented for PCR amplification and sequencing library preparation. The prepared libraries were loaded into different lanes of a flow cell for sequencing on an Illumina sequencer. At least 40 million pair-end 100 bp reads were obtained for each sample.

The read quality was assessed by FastQC to remove the reads with scores lower than 20. The Tuxedo suite (Tophat-Cufflinks-Cuffdiff) was initially used for analysis. Then the STAR-FeatureCounts/Htseq-count-DESeq2 pipeline was also employed. For this pipeline, the filtered reads were mapped to the mouse genome (mm9) using STAR, and the mapped reads were then counted with FeatureCounts or Htseq-Count, followed by differential analysis with DESeq2. The new pipeline was faster than the Tuxedo suite, but results from the two pipelines were consistent.

For gene ontology (GO) analysis, the Log_2FC (fold change) value of 0.8 was used as the cutoff to select top up- or downregulated genes for GO analysis via the bioinformatic tools Enrichr https://amp.pharm.mssm.edu/Enrichr/ (Kuleshov et al., 2016) and Metascape (http://metascape.org/gp/index.html#/main/step1) (Zhou et al., 2019). The detailed gene and GO lists have been deposited in the GEO database: GSE133195.

RT-qPCR. Selected gene targets were quantified in cDNA prepared from neonatal wild-type and mutant cerebral cortices or cultured neurospheres as described (You et al., 2016; You et al., 2015a). The RT-qPCR primers used for amplifying gene targets from neonatal cerebral cortices were as follows: *Gfap,* ccctggctcgtgtggattt and gaccgataccactcctctgtc;
Ngfr, cgaatgcgaggagatccctg and gtcaccgtatcggccactg;
Neat1, cctcggttgacgcctacaca and atgatgctcccagaacaagaca;
Malat1 ttcaagttggcaagtaactcc and cagcttcagaagagtcccc;
Tnc, acggctaccacagaagctg and atggctgttgttgctatggca;
Bcas1, agaagcgaaaggctcggaag and agggacagaataactcagagtgt;
Cdkn1a, cctggtgatgtccgacctg and ccatgagcgcatcgcaatc;
Nefl, ccgtacttttcgacctcctaca and cttgtgtgcggatagacttgag;
Hopx, agatcctggagtacaacttc and ttaaaccatttctgcgtct;
Apoe, ctgacaggatgcctagccg and cgcaggtaatcccagaagc;
Ncan, tgcaaccacggctaagctc and ggggataagcaggcaatgac;
Sgk1, ctgctcgaagcacccttacc and tcctgaggatgggacattttca;
Nr4a2, gtgttcaggcgcagtatgg and tggcagtaatttcagtgttggt;
Id1, cctagctgttcgctgaaggc and ctccgacagaccaagtaccac;
Jmjd1c, cacattcttggatctgtgacca and atgctgtctttgcagttgagg;
Plk2, cctgcggactatcacctacca and ctgcccatcttcagaaggct;
S100a4, tgagcaacttggacagcaaca and cttcttccggggctccttatc;
Nefm, acagctcggctatgctcag and cgggacagtttgtagtcgcc;
Atf5, tgggctggctcgtagactat and gtcatccaatcagagaagccg;
Sox1, aacacccggattacaagtacc and ccagcgagtacttgtcctt;
β-Actin, ggctgtattcccctccatcg and ccagttggtaacaatgccatgt; and
Hdac3, caccaagagccttgatgcctt and gcagctccaggataccaattact.

Additional RT-qPCR primers used for validating gene targets in cultured neurospheres were:
Dlx1, atgccagaaagtctcaacagc and aacagtgcatggagtagtgcc;
Dlx2, gtggctgatatgcactcgacc and gctggttggtgtagtagctgc;
Dlx5, tctctaggactgacgcaaaca and gttacacgccatagggtcgc;
Dlx6, aaaacgacagtgatcgaaaacgg and agtctgctgaaagcgatggtt;
Pbx3, cgaggcgcaagcaaagaaac and tgccaaaagcatattgtccagt;
Lhx6, ctacttcagccgatttggaacc and gcaaagcactttctcctcaacg;
Gad1, cacaggtcaccctcgattttt and accatccaacgatctctctcatc;
Gad2, tccggcttttggtccttcg and atgccgcccgtgaactttt;
Cux2, gactgccctactatccagcat and gcatgtcactcacgctaccc;
Tbr1, gcagcagctacccacattc and gtccttggagtcaggaaaattgt;
Id1, cctagctgttcgctgaaggc and ctccgacagaccaagtaccac;
Id3, cgaccgaggagcctcttag and ggacgcgatagggaagacc;
Hes1, ccagccagtgtcaacacga and aatgccgggagctatctttct;
Hes5, agtcccaaggagaaaaaccga and gctgtgtttcaggtagctgac; and

Hes6, accacctgctagaatccatgc and gcacccggtttagttcagc.

Statistical analysis. Statistical analysis was performed with unpaired 2-tailed Student's *t* test. $p<0.05$ was considered to be statistically significant. Data are presented as mean ± s.d. (standard deviation). Graphs were generated with GraphPad Prism 6 (Graphpad Software).

SUPPLEMENTARY REFERENCES

Gingras, H., Cases, O., Krasilnikova, M., Berube, G., and Nepveu, A. (2005). Biochemical characterization of the mammalian Cux2 protein. Gene *344*, 273-285.

Hevner, R.F., Shi, L., Justice, N., Hsueh, Y., Sheng, M., Smiga, S., Bulfone, A., Goffinet, A.M., Campagnoni, A.T., and Rubenstein, J.L. (2001). Tbr1 regulates differentiation of the preplate and layer 6. Neuron *29*, 353-366.

Kim, G.W., Li, L., Gorbani, M., You, L.Y., and Yang, X.J. (2013). Mice Lacking alpha-Tubulin Acetyltransferase 1 Are Viable but Display alpha-Tubulin Acetylation Deficiency and Dentate Gyrus Distortion. J Biol Chem *288*, 20334-20350.

Kuleshov, M.V., Jones, M.R., Rouillard, A.D., Fernandez, N.F., Duan, Q., Wang, Z., Koplev, S., Jenkins, S.L., Jagodnik, K.M., Lachmann, A.*, et al.* (2016). Enrichr: a comprehensive gene set enrichment analysis web server 2016 update. Nucleic Acids Res *44*, W90-97.

Lai, T., Jabaudon, D., Molyneaux, B.J., Azim, E., Arlotta, P., Menezes, J.R., and Macklis, J.D. (2008). SOX5 controls the sequential generation of distinct corticofugal neuron subtypes. Neuron *57*, 232-247.

Li, L., Jayabal, S., Ghorbani, M., Legault, L.M., McGraw, S., Watt, A.J., and Yang, X.J. (2019). ATAT1 regulates forebrain development and stress-induced tubulin hyperacetylation. Cell Mol Life Sci, doi: 10.1007/s00018-00019-03088-00013.

Nieto, M., Monuki, E.S., Tang, H., Imitola, J., Haubst, N., Khoury, S.J., Cunningham, J., Gotz, M., and Walsh, C.A. (2004). Expression of Cux-1 and Cux-2 in the subventricular zone and upper layers II-IV of the cerebral cortex. J Comp Neurol *479*, 168-180.

Sansregret, L., Vadnais, C., Livingstone, J., Kwiatkowski, N., Awan, A., Cadieux, C., Leduy, L., Hallett, M.T., and Nepveu, A. (2011). Cut homeobox 1 causes chromosomal instability by promoting bipolar division after cytokinesis failure. Proc Natl Acad Sci U S A *108*, 1949-1954.

You, L., Li, L., Yan, K., Zou, J., Belle, J., Nijnik, A., Wang, E., and Yang, X.J. (2016). BRPF1 is essential for development of fetal hematopoietic stem cells. J Clin Invest *126*, 3247-3262.

You, L., Yan, K., Zou, J., Zhao, H., Bertos, N.R., Park, M., Wang, E., and Yang, X.J. (2015a). The lysine acetyltransferase activator Brpf1 governs dentate gyrus development through neural stem cells and progenitors. PLoS Genet *11*, e1005034.

You, L., Zou, J., Zhao, H., Bertos, N.R., Park, M., Wang, E., and Yang, X.J. (2015b). Deficiency of the chromatin regulator Brpf1 causes abnormal brain development. J Biol Chem *290*, 7114-7129.

Zhou, Y., Zhou, B., Pache, L., Chang, M., Khodabakhshi, A.H., Tanaseichuk, O., Benner, C., and Chanda, S.K. (2019). Metascape provides a biologist-oriented resource for the analysis of systems-level datasets. Nat Commun *10*, doi: 10.1038/s41467-41019-09234-41466.